Department of Precision and Microsystems Engineering

Design, topology optimization, fabrication and testing of an adjustable compliant slit mechanism

Nathan Ooijevaar

Report no : 2026.034
Coach : Ir. A. Garde
Professor : Prof. dr. ir. M. Langelaar
Specialisation : Computational Design and Mechanics
Type of report : Master Thesis
Date : 18 May 2026

Design, topology optimization, fabrication and testing of an adjustable compliant slit mechanism

Towards the future of X-ray astronomy

ME56035: MSc Thesis

Nathan Ooijevaar

Delft University of Technology

TU Delft

Design, topology optimization, fabrication and testing of an adjustable compliant slit mechanism

Towards the future of X-ray astronomy

by

Nathan Ooijevaar

to obtain the degree of Master of Science
at the Delft University of Technology,
to be defended publicly on Monday May 18th,2026 at 9:00 AM.

Student number:	4903374	
Project duration:	November, 2024 – May, 2026	
Thesis committee:	Prof. dr. ir. M. Langelaar,	TU Delft, Supervisor
	Prof. dr. ir. J. Herder,	TU Delft, External commitee member
	Dr. R. den Hartog,	SRON, Internship supervisor
	Ir. A. Garde,	TU Delft, Daily supervisor

TU Delft Delft University of Technology

SRON SPACE RESEARCH ORGANISATION NETHERLANDS

Preface

This report is the result of my research on the design and optimization of a mechanism to be used for the development of technology for future space missions, carried out both at Delft University of Technology and Space Research Organization of the Netherlands.

What initially drew me to this project were the ties to space research, an interest of mine since a young age. When, during the first meeting regarding the project, I encountered a different professor than anticipated who told me that I could incorporate topology optimization into the project, I was sold. After a year (and a bit) I am happy to say that I made the right decision. During many meetings, lunches, and coffee breaks, I gained a great wealth of knowledge on two topics that are close to my heart.

I would like to express my sincerest gratitude to Aditya Garde, Matthijs Langelaar, and Roland den Hartog for their guidance and support throughout this project. Not only in their guidance in steering the project and lending a helping hand when needed, but also giving me autonomy to shape my own path. I would also like to thank Just Herder for taking part in my thesis committee.

Furthermore, I would like to thank Kevin Ravensberg from SRON for his help in the practical needs that accompany building a test setup, Tonny Coppens from SRON for making the various wafer pairs used to create the slit, and Leon Roessen from DEMO for his help getting my designs manufactured.

Finally, I would like to thank my friends and family for their support throughout this project and being a welcome distraction when needed.

I want to acknowledge the role of generative AI in this thesis. While AI tools assisted in refining individual text sections and generating and debugging code, the ideas, arguments, and conclusions presented here are entirely my own.

Nathan Ooijevaar
Delft, May 2026

Abstract

To create an X-ray Interferometry test bed a high precision adjustable slit mechanism is needed. Compliant mechanisms are ideal solutions for such high precision mechanisms. This research presents the design, manufacturing, and testing of such a compliant mechanism. Furthermore, topology optimization is explored and evaluated as an alternative design method to find a novel mechanism that performs better than a traditionally synthesized counterpart. A traditionally designed mechanism was first designed and characterized using a $405\ \mathrm{nm}$ laser source and Fraunhofer diffraction analysis. Although optical verification was limited to a minimum slit width of $3\ \mu\mathrm{m}$, experimental results demonstrate that the traditionally developed design has the potential to achieve dimensional requirements, with demonstrated step sizes of $0.2\ \mu m$. Simultaneously, a topology optimization model was developed, implementing penalized strain energy, parasitic displacement, and decoupling constraints, along with a robust formulation, to generate an alternative multi-degree-of-freedom mechanism. Although topology optimization proved a tool capable of producing an alternative compliant mechanism, there is still work to be done to fully mature this synthesis method. The research concludes that the developed mechanism meets the requirements set for the X-ray Interferometry test bed, whilst the topology optimization proves a viable alternative, albeit complex, method for future high-performance iterations.

Contents

Nomenclature

Abbreviations

Abbreviation	Definition
CNJ	Circular notch joint
CXRO	Center for X-Ray Optics
DoC	Degree of constraint
DoF	Degree of freedom
GCMMA	Globally convergent method of moving asymptotes
HTP	Hyperbolic tangent projection
KKT	Karush–Kuhn–Tucker
MMA	Method of moving asymptotes
MPs	Motion paths
MSE	Mutual strain energy
PDE	Partial differential equation
ROM	Range of motion
SE	Strain energy
SIMP	Solid isotropic material with penalization
SRON	Space Research Organization Netherlands
TO	Topology optimization
XRI	X-ray interferometry/interferometer

Symbols

Symbol	Definition	Unit
a	Slit width	m
a_{eff}	Effective slit width	m
b	Mechanism plate thickness	m
D	Baseline	m
E	Young's modulus	MPa
E_γ	Photon energy	eV
f	Eigenfrequency	Hz
F_i	Input force	N
$g_i(x)$	Inequality constraints	

Symbol	Definition	Unit
$h_i(x)$	Equality constraints	
h_z	Wafer axial offset	m
I	Intensity of light	W/m^2
I_0	Light source intensity	W/m^2
$J(x)$	Objective function	
k	Stiffness	N/m
K_x	Mechanism translation stiffness	N/m
K_{θ_y}	Out-of-plane rotational stiffness	N/rad
K_{θ_z}	Hinge rotational stiffness	N/rad
L	Link length	m
L_{abs}	Absorption distance	m
m	Sprung mass	kg
p	SIMP penalty / total perimeter	
r	Radius	m
R	Hinge radius	m
T	Transmittance	
t	hinge thickness	m
u	Displacement	m
U_p	Potential energy	J
U_s	Strain energy	J
V	Volume	m^3
V^*	Allowed volume fraction	
W	Slit width	m
W_{in}	Virtual work	J
$W_{s,\text{pen}}$	Penalized strain energy	J
z	Propagation distance of light	m
δ_X	Mechanism range of motion	m
$\delta\rho$	Density gradient	
ϵ_{el}	Element strain	
γ	Slit angular offset	rad
η	Output decoupling factor	
λ_i	Lagrange multiplier	
μ_{abs}	Absorption coefficient	m^{-1}
Ω	Optimization design space	
$\lvert\partial\Omega_S\rvert$	Topology domain perimeter estimate	
ρ	Density	

Symbol	Definition	Unit
ρ_i	Element density	
$\tilde{\rho}_i$	Filtered element density	
$\bar{\tilde{\rho}}_i$	Projected element density	
σ	Stress	MPa
σ_0	Initial stress	MPa
θ	Diffraction angle	rad
θ_i	Interferometric resolution	rad
θ_t	Projection threshold	
θ_z	Hinge angular range of motion	rad
ω	Natural eigenfrequency	Hz
ξ	Input decoupling factor	

1

Introduction

Advancements in astronomical research to farther and compact objects require the development of new technologies. One such technology in development is X-ray interferometry (XRI), which could be used to further imaging capabilities for deep space objects and would be able to directly image the event horizon of black holes (Uttley et al., 2021). A test bed for XRI is currently being developed at Space Research Organization of the Netherlands (SRON) in Leiden to demonstrate the feasibility of XRI for single space-craft missions. A schematic of this test bed is shown in Figure 1.1.

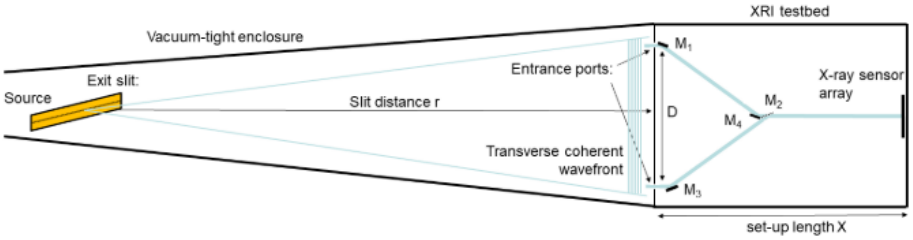

Figure 1.1: Conceptual sketch of an XRI testbed (den Hartog et al., 2020). Note that the image is not to scale.

A crucial part of this test bed is the slit mechanism used to generate a transversely coherent X-ray beam (Figure 1.1: exit slit, from den Hartog et al., 2020). The slit is formed using cleaved wafers, which can provide atomically flat surfaces. The slit must be adjustable, with a width ranging from a minimum of $0.5\ \mu\mathrm{m}$ to a maximum of $500\ \mu\mathrm{m}$ over a slit length of $20\ \mathrm{mm}$, allowing the slit to be used for multiple wavelengths. Furthermore, a second degree of freedom is needed to achieve sufficient parallelism between the slit edges.

This combination of high precision and large stroke is an ideal subject for compliant mechanisms as they eliminate friction and backlash. Additionally, since the test bed will operate in vacuum, traditional hinges cannot be used because they produce particles due to friction. Therefore, the mechanism must be operated remotely and fit within a constrained design space. Furthermore, the mechanism should have a sufficiently high eigenfrequency to avoid resonance from environmental vibrations.

In addition to operational constraints, the manufacturability and robustness of the design are crucial, as the mechanism will be fabricated and tested.

In summary, the design challenge is defined by the following criteria:

- A mechanism that is vacuum compatible.
- Remote actuation of the mechanism.
- The range of motion that is required, along with the precision to achieve a consistent minimum slit width of 0.5 micron.

- Positioning of the slit. The location of the slit in front of the source defines where the optical axis lies. So, there should be a way to ensure the slit is located correctly.
- Multiple degrees of freedom. The slit width needs to be variable, and the angle between the two slit halves also needs to be adjustable.
- A mechanism that is not affected by the vibrations present in the environment.
- Limited design space. The largest region has a diameter of $100\ mm$, whilst the smallest region is only $35\ mm$ in diameter.

As no off-the-shelf mechanism meets these requirements, a dedicated design needs to be developed. An existing prototype mechanism serves as a starting point that should be developed further, including the design of a mounting and actuation system for the vacuum environment.

The combination of challenges stated makes for a complex design case. A design method that could provide a better solution than one designed conventionally is topology optimization. Initially proposed by Bendsøe and Kikuchi, 1988, topology optimization aims to find the optimal distribution of material in a design domain based on an objective function and constraints. The biggest advantage of using topology optimization is that no initial design is needed. If properly formulated, a topology optimization model can find a solution to a design case from scratch, leading to designs that are hard to find intuitively.

Although the final design is determined by the optimizer, designers can still influence the final design through numerous methods. Changing the optimization objective, boundary conditions, (virtual) loads, and constraints will alter the final topology. This is both an advantage and disadvantage. It allows the designer to steer the optimizer to practical solutions, but will also introduce bias in the optimization. The balance between a practically usable solution and the freedom for the optimizer to find novel topologies is something that should be managed carefully. The final optimized design will be compared to the traditionally designed counterpart using COMSOL Multiphysics®to assess the benefits of topology optimization.

In summary, the objective for this MSc thesis is to design, manufacture, and test a high aspect ratio adjustable compliant slit mechanism with demanding precision requirements. Two design methods will be used in parallel. Firstly, the traditional design method that will ultimately be employed in the overarching project, which will also serve as a baseline. Secondly, the use of topology optimization to try and find better performance of the mechanism. In addition to the mechanism, the system to mount and actuate the mechanism inside vacuum will be designed.

1.1. Research questions & goals

With the given design challenge, two separate research paths arise. Firstly, the development of the slit mechanism and the surrounding system. To guide this research, the goal is divided into a main question supported by two sub-questions:

How can a high aspect ratio adjustable slit mechanism be designed to provide control over slit width and angular alignment to adhere to the requirements of the XRI test bed?

The sub-questions to support this question are:

- Which mechanism and actuation method enable the required sub micron precision and control to produce an adjustable slit with the required dimensional tolerances?
- To what extend does the developed prototype meet the operational requirements for the slit dimensions needed?

The second part involves the development of a topology optimization model to produce an alternative mechanism. Here, the goal is to find a mechanism that performs better than the traditional mechanism based on certain performance metrics. For this part, there are certain questions that need to be answered, with one main question:

'Can topology optimization be used to generate a slit mechanism that performs better than a traditionally designed counterpart?'

This research question is supported by the two following sub-questions:

- Which methods need to be combined to find a mechanism that meets the design challenges?
- Where is designer input necessary to find a practically viable solution and where can this be minimized?

1.2. Report layout

This report is divided into 7 Chapters, including the current. To start, relevant literature regarding XRI and the concept of topology optimization will be presented in Chapter 2. Then, in Chapter 3 the design challenges are elaborated. The functional requirements, performance criteria, design criteria, and constraints will be discussed. Following this, the design process and design for the traditional mechanism and surrounding system are presented in Chapter 4. The topology optimization model, the optimization modules used, the found topology optimized design, and general considerations to find a practically usable design are discussed in Chapter 5. The validation the mechanism design through optical tests is presented in Chapter 6. A discussion on the performed work, found results, and recommendations for future work are given in Chapter 7. Finally, answers to the research questions posed in the previous Section will be given in Chapter 8.

2

Literature

This Chapter will highlight the theories used for this design study. First, XRI will be explained. More in depth information on the context for this master thesis project will be discussed. Then, the basic concept of topology optimization will be discussed.

2.1. X-ray interferometry overview

2.1.1. Interferometry

Optical interferometry is based on the linear superposition of electromagnetic fields (Fowles, 2012). When two mutually coherent electromagnetic wave fronts are in phase, they constructively interfere. If they are exactly out of phase, the waves destructively interfere. Young's double slit experiment was the first time the interference of light was demonstrated, by projecting a fringe pattern on a wall. This pattern contains information about the light source that creates the wave fronts and can be used to recreate an image of the light source.

Interferometry is often used in radio telescopes such as the Event Horizon Telescope (EHT) which was used to image the super massive black hole M87* in 2019 (Figure 2.1). For singular telescopes, the maximum angular resolution that can be achieved is limited by the Rayleigh diffraction limit ($\theta_R = 1.22\ \lambda/D$). Significantly better angular resolutions can be achieved using interferometry. Multiple telescopes simultaneously record a signal that is combined to reconstruct an image. In this case, the angular resolution is defined as $\theta = \lambda/2D$. Here, λ is the wavelength of light observed, and D is the baseline of the interferometer, which in the case of radio telescopes is the distance between them.

There are two methods to increase the angular resolution. Either increase the baseline, or decrease the wavelength observed. The EHT the baseline is the diameter of the earth, resulting in an angular resolution of about $25\ \mu\,\mathrm{arcsec}$ (Uttley et al., 2021). Using X-rays, a similar angular resolution can be

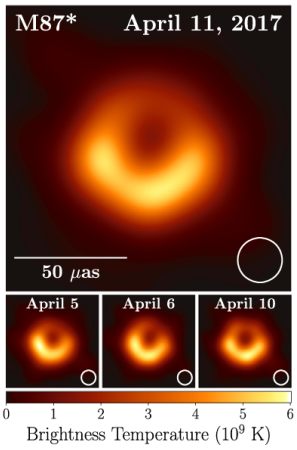

Figure 2.1: Image of the M87* super massive black hole. Note that the large image is actually an average of three different imaging methods, from Akiyama et al., 2019.

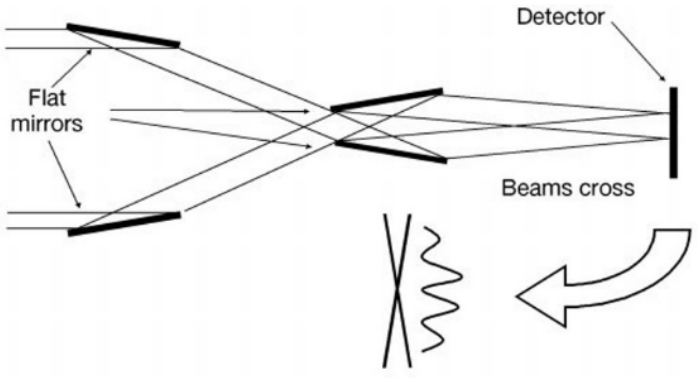

Figure 2.2: Schematic of the X-ray interferometer designed and built by Cash et al., 2000. The propagation of light is from left to right. The image is not to scale.

achieved with a $1\ m$ baseline. This enables the technology to be placed on a single satellite. Furthermore, the X-ray band remains a largely unexplored spectrum of light, making a compelling science case (Uttley et al., 2021).

2.1.2. XRI design by Cash et al.

X-ray fringes have been detected as far back as 1932, when Kellstrom used grazing incidence reflection to build likely the first X-ray interferometer using a Lloyd's Mirror and a Fresnel bent mirror. More recently, Cash et al., 2000 were able to produce and detect X-ray fringes using a grazing incidence interferometer with four flat mirrors. A conceptual overview of the setup can be found in Figure 2.2. The interferometer had a baseline of $1\ \mathrm{mm}$ producing an angular resolution of 0.1 arc second.

Although the setup can be used to produce fringes, there is a drawback in using the design. The scaling of the setup is problematic. For the $1\ \mathrm{mm}$ baseline used, a vacuum system of $120\ \mathrm{m}$ was needed. For a $30\ \mathrm{cm}$ baseline, the vacuum system would need to be $300\ \mathrm{km}$ long. Apart from being impractical to build and operate on earth, this design cannot be flown on a single spacecraft. Cash, 2003 proposes multiple spacecraft missions to address the scaling issues, in which the optics and detectors are placed on two or more separate spacecraft.

2.1.3. The Willingale design

Willingale, 2004 proposes a different solution to the scaling issue, using a setup with a slatted combining mirror. A conceptual sketch of this design is shown in Figure 2.3. An incoming transversely coherent X-ray beam passes through a double slit, use to block stray light, with baseline D. Two mirror pairs are used to steer the beams towards the detector: M1-M2 and M3-M4. The M2 mirror is the crucial part in this setup. A slatted design, mimicking partially closed Venetian blinds, is used to combine the two beams. Figure 2.4 illustrates what happens with the X-ray beams at the M2 mirror. By optimizing the ratio between the grazing angle and the beam angle for the mirror pairs, the total size of the interferometer can be reduced by multiple factors of 10^3 (den Hartog et al., 2020).

den Hartog et al., 2020 intend to push the envelope further using the design proposed by Willingale by ultimately placing multiple XRI on a single spacecraft with an angular resolution in the range of micro arc seconds. The first step in achieving this is to prove that the XRI concept proposed by Willingale works using X-rays. For the proposed test bed a baseline of $10\ \mathrm{mm}$ will be used. The total length of the system will be about $15\ \mathrm{m}$. In order for the interferometer setup to work, the X-ray beam passing through the double slit entrance ports needs to be transversely coherent. One possibility to achieve this is to create and use a Fraunhofer diffraction pattern. For such a pattern, the central $50\ \%$ of the central peak is

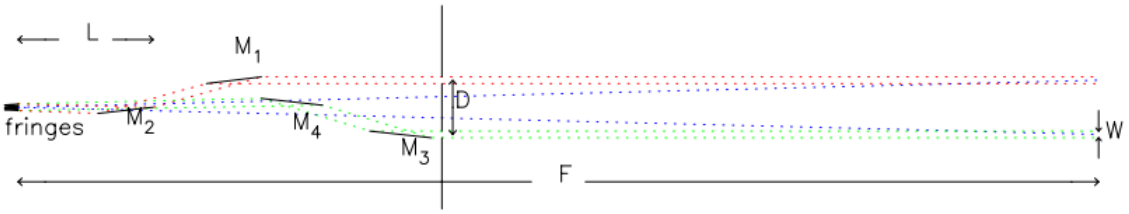

Figure 2.3: The Willingale X-ray interferometer setup. M1, M3, and M4 are regular flat mirrors. M2 is a slatted mirror meant to combine the two beams of light. The propagation of light is from right to left. In this image there are two separate beams of light entering the entrance port located at the vertical line. In the test bed this will be one wavefront created by the slit. Note that the image is not to scale. (Willingale, 2004)

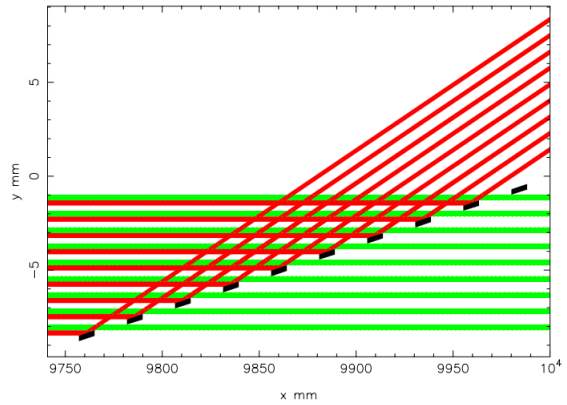

Figure 2.4: Schematic of the slatted M2 mirror. The red and green lines are the X-ray beams. The black rectangles represent the slats from the mirror. Note that the propagation of light is from right to left, from Willingale, 2004.

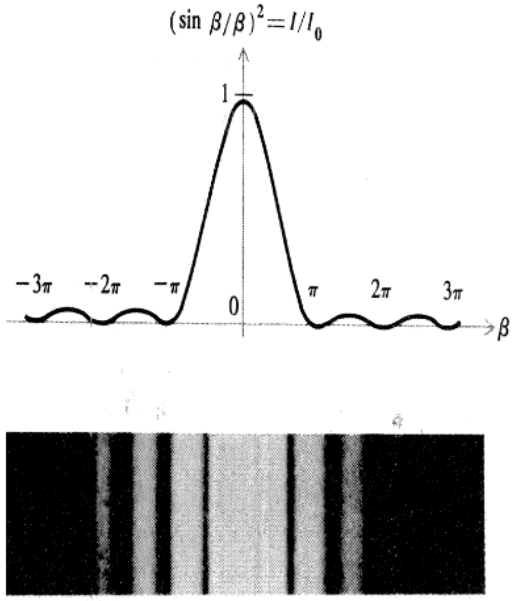

Figure 2.5: Normalized Fraunhofer diffraction pattern intensity profile for a narrow rectangular slit, Fowles, 2012. The central 50% of the central maximum is coherent and consequently needs to cover the entrance port of the slit.

transversely coherent (den Hartog et al., 2020). An image showing a Fraunhofer diffraction pattern can be seen in Figure 2.5. The double slit through which the X-ray beams pass needs to be fully covered by the transversely coherent part of the central peak of the Fraunhofer diffraction pattern. This wavefront can be produced using a very narrow slit. For the dimension available and the wavelengths of light used this is in the order of microns. The exact needed width can be determined using the following equations for Fraunhofer diffraction patterns for a narrow rectangular slit:

$$\alpha = \frac{2\lambda}{W} \tag{2.1}$$

$$d_f = \frac{2\lambda\ z}{W} \tag{2.2}$$

Here, α is the diffraction angle, d_f is the width of the central band, λ is the wavelength, W is the width of the slit, and z is the distance from the slit in the travel direction of the wavefront.

2.2. Topology Optimization

As stated in the introduction, topology optimization is a way to solve the challenges of the presented design case. This Section gives a general overview of topology optimization, specifically for the Solid Isotropic Material with Penalization (SIMP) method.

2.2.1. General formulation

The topology optimization methods most widely applied for compliant mechanisms are the density-based approaches. From these methods, the SIMP method is used the most due to its ease of use and versatility (Zhu et al., 2020).

The general idea of the SIMP method is to fill a design space Ω with n finite elements that can vary in density from 0 to 1. The goal of the optimization is to find the optimal distribution of material in the design space for the given objective. A primary constraint that is often applied is a volume constraint to limit the amount of material that can be used by the optimization algorithm (Bendsøe, 1989).

A general topology optimization problem for compliant mechanisms can be formulated in the following manner.

$$\begin{aligned} \min: \quad & J(\mathbf{x}) && (2.3)\\ s.t.: \quad & V \leq V^* && (2.4)\\ & g_i(\mathbf{x}) \leq 0 && (2.5)\\ & h_i(\mathbf{x}) = 0 && (2.6) \end{aligned}$$

$J(\mathbf{x})$ is the objective function that needs to be minimized and $V \leq V^*$ is a volume inequality constraint. Often, the objective is to minimize (or maximize) compliance in a specific direction. Additional inequality constraints $g_i(\mathbf{x})$ and equality constraints $h_i(\mathbf{x})$ can be added if necessary (Zhu et al., 2020).

The most important distinction for the SIMP method is that the problem has been made continuous as the material density of an element can be any value between 0 and 1. To avoid 'gray' areas (areas where element densities lie between 0 and 1) a penalization function is applied to prevent the usage of these intermediate densities. This is because these intermediate material areas do not have a physical meaning. Such a penalty function looks like this:

$$E(\mathbf{x}) = [\rho(\mathbf{x})]^p \, \overline{E}, \quad 0 < \rho_{min} \leq \rho \leq 1, \quad p > 1 \tag{2.7}$$

where $E(\mathbf{x})$ is the Young's Modulus for a specific element, $\overline{E}$ is the Young's modulus of the chosen material, p is the penalization factor, and $\rho(\mathbf{x})$ is the element density. Note that the element density cannot be equal to 0 (Sigmund, 1997). This is a measure taken to avoid singularity problems in system matrices. It is evident from the equation that intermediate values are discouraged, as density scales linearly and Young's modulus scales by the power of p. Because of this, intermediate values give very little stiffness for the amount of material used. The result is that most elements will be either 1 or 0. A big drawback is that the SIMP method suffers greatly from mesh dependency. Changes in mesh size can result in big changes in the final topology (Bendsøe, 1989).

2.2.2. Sensitivity analysis

For topology optimization, the standard procedure for sensitivity analysis is to determine the derivatives of the displacements with respect to the design variables of the optimization problem (Bendsøe and Sigmund, 2004). The sensitivities are needed, as the optimizer uses the gradient of the objective and constraint functions to find global or local optima. The most common way to determine the sensitivities for topology optimization is to use the adjoint method (Bendsøe and Sigmund, 2004), which is also used in the COMSOL Multiphysics ®software package which will be used to perform the topology optimization for this report. Instead of calculating the derivatives of the displacements directly, an augmented response is formed. Lagrange multipliers λ_i are introduced, which can eliminate the sensitivities of state variables, reducing computational costs.

2.2.3. Filtering

Two major issues present when using the SIMP method are that of checkerboard patterns and mesh dependency. Checkerboard patterns (alternating 0 and 1 elements) can appear when using the SIMP

Figure 2.6: Results of applying a Heaviside filter to the density filter. The upper picture is the unfiltered design. The lower picture shows the filtered design, from Sigmund, 2007.

method when no filtering is present. This is because these regions give higher than possible stiffness for the amount of material used. The second issue is that of mesh dependency. When looking at the diagonal edges in Figure 2.6, the problem of mesh sizing becomes apparent. A coarse mesh will result in jagged edges, which are both not producible and give inaccuracies in the found performance when compared to reality. An obvious solution is to decrease the mesh size. This would result in smoother edges and more realistic results. However, what is observed is that this greatly influences the final design found. As the elements become smaller, the boundaries for void-material phases become more defined. This results in finer structures and more intricate designs. Generally, mesh-independent results are deemed favorable (Sigmund, 1997).

In order to combat the checkerboard and mesh dependency problems, filtering schemes are found in literature.

Density filters

One scheme proposed is a so-called density filter. The idea of a density filter is to replace the density of each element with the weighted average of a mesh-independent region around that element. This operation can be generalized as a convolution integral over the filter region (Bourdin, 2001). Often the convolution integral is replaced by a simpler expression (Lazarov and Sigmund, 2011). Bruns and Tortorelli, 2001 proposes this basic expression:

$$\tilde{\rho}_e = \frac{\sum_{i \in N_e} w(\mathbf{x}_i) v_i \rho_i}{\sum_{i \in N_e} w(\mathbf{x}_i) v_i}, \tag{2.8}$$

Here, $\tilde{\rho}_e$ is the filtered density of element e, based on the densities of the surrounding elements, ρ_i. The filtering region N_e for each element is defined as the following

$$N_e = \{i \mid \|\mathbf{x}_i - \mathbf{x}_e\| \leq R\} \tag{2.9}$$

and the weight factor $w(x_i)$ is

$$w(\mathbf{x}_i) = R - \|\mathbf{x}_i - \mathbf{x}_e\| \tag{2.10}$$

As the region used for the filter is mesh-independent, the problem of mesh dependency is alleviated. The downside is that because of the averaging of element densities, elements with intermediate densities become more apparent. Methods to alleviate this effect are presented in Section **??**.

Helmholtz Partial Differential Equation filtering

Using the density filters described in the previous Section has a large drawback. To use these filters information from the region around each element is needed. This can become computationally expensive when dealing with complex domains and geometries, where the filter region can, for example, cross subdomain boundaries (Lazarov and Sigmund, 2011). Lazarov and Sigmund, 2011 propose a new method to produce density filters, using Helmholtz partial differential equations. The main advantage is the reduction in computational cost, rather than outright performance of the filter. As discussed in the previous Section, the density filters are generally a convolution over the filter region. Lazarov and Sigmund, 2011 suggest that instead of outright solving this convolution, the density filter can be seen as a solution of the Helmholtz partial differential equation (PDE).

$$-r^2 \nabla^2 \tilde{\rho} + \tilde{\rho} = \rho \tag{2.11}$$

As the PDE does not need information from neighboring cells the issue of high computational cost for complex problems is alleviated. This is also the type of filtering that is employed by the software package COMSOL Multiphysics®, which will be used to perform the topology optimization.

2.2.4. Threshold projection

To further reduce the appearance of gray areas, threshold projections can be used. A step function is applied over the filtered design domain, where all intermediate values above a certain threshold value θ_t are set to 1 and all values below this threshold are set to 0. Another benefit of using a projection is that it can be used to setup a robust optimization formulation, as will be discussed in Section 5.2.4.

To avoid issues with the infinite gradient of step functions, Guest et al., 2004 suggested using a regularized Heaviside step function. A parameter β is introduced that is used to determine the steepness of the regularization. As the parameter β approaches infinity, the smoothed step function approaches the step function. Generally, a higher β leads to a more black and white design, at the cost of computation speed.

A similar method, which is used in the software package COMSOL Multiphysics®, is to use a Hyperbolic Tangent Projection (HTP). Although mathematically not identical, they practically have the same effect and can be tuned in a similar manner. The Equation for the HTP is:

$$\bar{\tilde{\rho}}_i = \frac{\tanh(\beta\theta_t) + \tanh\big(\beta(\tilde{\rho}_i - \theta_t)\big)}{\tanh(\beta\theta_t) + \tanh\big(\beta(1 - \theta_t)\big)} \tag{2.12}$$

Again, β sets the steepness of the step slope and θ_t sets the density threshold.

2.2.5. Optimization algorithm

To perform the optimization, Globally Convergent Method of Moving Asymptotes (GCMMA) is used. It is an extension of the Method of Moving Asymptotes (MMA) originally proposed by Svanberg, 1987. MMA is an optimization algorithm especially efficient for structural optimizations, where the objective function J is usually a complex non linear function. The key idea is to approximate the computationally costly objective function with a strictly convex sub problem. This convex approximation is built up using the gradients of the objective and constraints. At each design iteration the convex sub problems are solved to update the design variables, until either convergence or maximum allowed iterations are reached. In this design case, it was the latter of the two options that terminates the design process. As mentioned, the GCMMA is a method proposed by Svanberg, 2002 that builds on MMA to eliminate its biggest drawback. It uses conservative approximations and inner iteration loops to ensure global convergence, which is not necessarily the case for MMA.

3

The design challenge

In this Chapter, the design challenge will be presented. First, the functional and non-functional requirements for the slit mechanism will be specified in Sections 3.1 and 3.2. Then, the performance

requirements will be discussed in Section 3.3. Finally, design criteria and constraints will shortly be elaborated in Sections 3.4 and 3.5.

3.1. Functional Requirements

These are the requirements that the design must adhere to. If these requirements are not met, the design cannot fulfill its purpose. As discussed in Chapter 1, to see fringes with the desired wavelength, the slit must have a certain width. Additionally, since multiple photon energies will be used, the slit needs to be adjustable. Specifically, photons with energies of 0.282, 0.45, and 1.25 keV will be used. A change in photon energy is equivalent to a change of wavelength, according to the following relation:

$$E_\gamma \approx \frac{1240}{\lambda} \tag{3.1}$$

As mentioned in Section 2.1, the double slit aperture must be covered by the central $50\ \%$ of the central peak of the Fraunhofer diffraction pattern. This corresponds to half the width of the central band, as depicted in Figure 2.5. From Equation 2.1, it becomes evident that the slit needs to be changeable in width. As the wavelength decreases, the diffraction angle decreases. Narrowing the slit compensates for this effect. Doing so manually is possible. However, it is not guaranteed that the width remains constant when mounting the slit system to the vacuum system. In addition, to manually change the width, the vacuum has to be broken. This means replacing the copper seals used to maintain the vacuum and pumping down the pressure for several hours afterward. In summary, this is a process that costs time and money and is not guaranteed to work. So, remote operation of the slit is a necessity.

The width of the slit should be kept equal throughout its entire length. In other words, the two edges should be parallel. Without parallelism, the interference pattern measured at the detector will degrade (Goodman, 2000). Furthermore, if the slits are not aligned well, then closing them to the required size will be impossible, because the bottom or top of the slit will come into contact before reaching the desired slit width. Assembling the system such that the slit edges are perfectly parallel is nearly impossible. As mentioned previously, it cannot be guaranteed that the parallelism is not affected during mounting in the vacuum system. Furthermore, perfect parallel motion cannot be guaranteed during the translation of the wafers. Therefore, the angle between the wafers must also be adjustable remotely. Since the slit does not need to be perfectly vertical, a rotational DoF needs to be added to one wafer to ensure the relative angle is adjustable.

3.2. Non-functional requirement

There is also an aspect of this design challenge that does not affect whether the mechanism functions, that also does not have specific tolerance in which it should lie, but that is important to improve the performance of the design. It is that the slit should be placed close to the source. The reason for this is that the number of photons that reach the camera should be maximized. As the slit will only be $0.5\ \mu m$ wide, the number of photons that pass through the slit will be low. Furthermore, the source does not provide a focused light beam. Rather, it is a source that emits light in all directions. Thus, the intensity of the light drops with distance, according to the inverse square law.

$$I \propto 1/r^2 \tag{3.2}$$

Doubling the distance from the source reduces the intensity of light that reaches the slit by 75%, which is also proportional to the amount of photons per second. Since the source is not very bright in the required X-ray band, it is important to maximize the amount of photons that pass through the slit by bringing the slit closer.

3.3. Performance requirements

Performance requirements set how well the required functions should be performed. These are quantified values which can be used to define the performance of the design.

As discussed in Section 3.1, the slit needs to be adjustable in width and set according to the wavelength used.

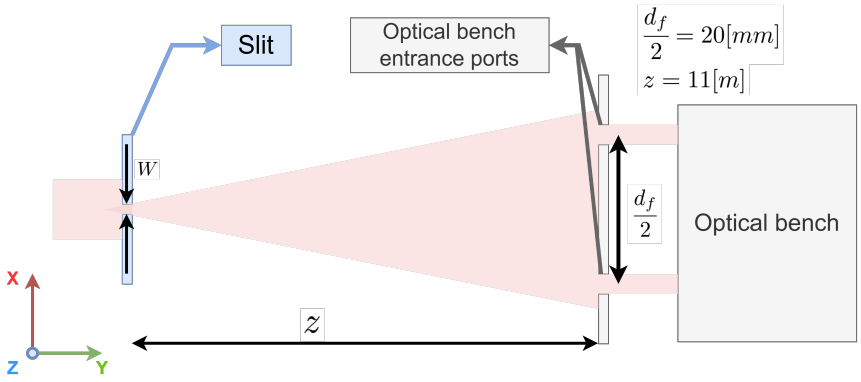

Figure 3.1: Schematic overview of the dimensions used to determine the required slit dimensions with Equation 2.2. Note that this image is not to scale.

Wavelength $[nm]$	405	4.4	2.8	1
Required slit width $[\mu m]$	222.5	2.42	1.54	0.55

Table 3.1: Required slit width for each wavelength that is to be used.

As mentioned in the Introduction, the required range of motion is $500\ \mu\text{m}$. This can be derived from Equations (2.1), (2.2) and (3.1). As discussed in Section 3.1, three x-ray photon energies will be used. These three energies correspond to the following wavelengths, according to Equation 3.1: $4.4\ \text{nm}$, $2.8\ \text{nm}$ and $1\ \text{nm}$. In addition, there is a desire to test the alignment using a blue light laser, which has a wavelength of about $405\ \text{nm}$. Using Equations (2.1) and (2.2) the required dimensions of the slit can be determined. These required slit widths for the XRI test bed can be found in Table 3.1. The relevant parameters, along with a schematic of the test bed, can be seen in figure 3.1.

So, the minimum range of motion should be $225.5\ \mu\text{m}$. Realistically, the initial width of the slit cannot be set to this exact value during assembly. The minimum range of motion should be higher than this to accommodate for assembly errors. So, taking a safety factor into account, it is set to $0.5\ \text{mm}$.

For the rotation DoF, there are no equations to determine the minimum required range of motion. The range of motion for the rotation is important to correct for the misalignment of the wafers during assembly. Tooling can be used to reduce misalignment. A typical set of vernier calipers has an accuracy of $0.05\ \text{mm}$. By measuring the distance between the wafers at the top and bottom of the slit, they can be aligned to an accuracy of $\tan(0.05/20) = 2.5\ \text{mrad}$ or $0.14°$. However, $0.15°$ range of motion is easily achieved using compliant hinges, so this is set as the minimum range of motion needed.

Much more important is the resolution of the actuation step size. The wafers should be parallel to below 10 arcsec, or roughly $50\ \mu\text{rad}$ to achieve proper coherence. Over the $20\ \text{mm}$ slit length, this equates to a difference of one micron. So, the step size of the actuation should be well below 1 micron to accommodate for this.

For the the width of the slit, the maximum allowed tolerance is even lower. A slit thinner than $0.5\ \mu\text{m}$ does not directly affect the functioning of the setup. However, it would lower the amount of photons that pass through the slit. So, a thinner slit would require longer exposure times. A wider slit *will* be problematic. The absolute limit beyond which the light falling on the detector will no longer be coherent is $1\ \mu\text{m}$. However, this would require perfect alignment with the X-ray source. Realistically, the slit should be no more than $0.6\ \mu\text{m}$ wide. This also means that the step size at the end effector should ideally be at or below $0.1\ \mu\text{m}$.

Not only is the size of the slit important, but the location of the slit is also crucial for the functioning of the full XRI setup. As previously stated, the slit determines the optical axis of the system. Moving the slit out of the optical axis will change which part of the central band of the Fraunhofer diffraction pattern will fall on the optical bench entrance ports. Moving the optical axis away from the center will lead to a

reduction in fringe visibility (Monnier, 2003). Furthermore (and more importantly), a shift in the location of the center of the optical axis during a measurement will lead to smearing of the fringes. When this occurs, maxima of the fringe pattern will fall on previous minima, leading to either a reduction in fringe visibility or complete loss of the fringes. This relation is governed by the following equation:

$$\theta_i = \frac{\lambda}{2 \cdot D} \tag{3.3}$$

θ_i is the interferometric resolution expressed in radians, λ the wavelength of light used and D is the baseline, which in the case of the XRI is $1\ cm$. At the location of the slit, this interferometric resolution is equal to a displacement of $1\ \mu m$. So there needs to be capability to keep the center of the slit in this range. A translating degree of freedom of the entire slit should be present, with a resolution of $1\ \mu m$.

For each DoF, there are certain tolerances in which the slit dimensions should lie. The most critical ones have been discussed. An overview for all tolerances can be found in Tables 3.2 and 3.3. For each DoF shown, the left image shows the desired orientation, and the right image shows the misaligned orientation. The axis orientation can be seen in Figure 3.2. Appendix A presents the tables including schematics for each DoF. Note that the DoFs marked with an asterisk (*) represent hard limits essential for the functionality of the XRI test bed. The other tolerances, set in discussion with SRON instrument scientists, are intentionally conservative. While exceeding these non-critical limits will not directly prohibit the operation of the test bed, the fringe quality will progressively deteriorate and will eventually be insufficient for proper performance analysis.

DOF	**Tolerance**
Translation in X *	$\pm 10\ \mu$m
Translation in Y	± 5 mm
Translation in Z	± 1 mm
Rotation around X	$\pm 1°$
Rotation around Y	$\pm 1°$
Rotation around Z	± 5 mrad

Table 3.2: Positioning tolerances for the slit assembly as a whole.

DoF	**Tolerance**
Translation of one wafer in X *	$0.1\ \mu$m
Translation of one wafer in Y	$\pm 20\ \mu$m
Translation of one wafer in Z	± 1 mm
Rotation of one wafer around X	$\pm 1°$
Non-parallel slit edge *	± 10 arcsec
Rotation of one wafer around Z	± 5 mrad

Table 3.3: Tolerances for relative positioning errors between the two wafer edges.

From these tolerances, the critical ones that can only be adjusted during assembly are the rotation of the wafers around the z-axis. The reason these two tolerances are critical is that X-rays can penetrate through material, up to a certain depth. If the wafer planes are not perfectly perpendicular to the X-ray beam, the X-rays can partially pass through the wafer at the corners. A schematic drawing showcasing this effect can be found in Figure 3.3. The factor of light that penetrates through the material is called the transmittance and is defined as:

$$T = \frac{I}{I_0} \tag{3.4}$$

Here, I_0 is the initial intensity and I is the intensity after passing through a medium. The transmittance can be determined using the Beer-Lambert Law, which is the following:

$$I = I_0 e^{-\mu_{abs} L_{abs}} \tag{3.5}$$

Here, μ_{abs} is the absorption coefficient per meter and L_{abs} is the distance traveled through the medium. The absorption coefficient is dependent on both material and photon energy. Using data from The Center for X-ray Optics (CXRO), the transmittance can be validated (Lawrence Berkeley National Laboratory's, 2010). The transmittance versus the thickness can be found in Figure 3.4a. As stated, if the wafers are not placed perfectly perpendicular to the beam path, the corners give a very low thickness, meaning the wafers are partially transparent. This angle can be related to the width over which the wafers are (semi-) transparent for the x-rays. For small angles, this width is approximated using:

$$w = \theta \cdot t \tag{3.6}$$

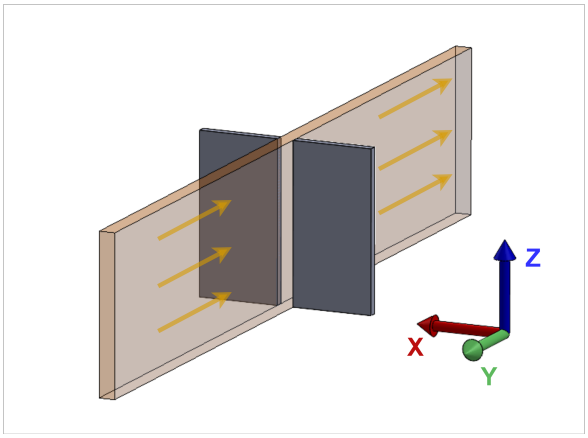

Figure 3.2: Definition of the axis orientation used for Table 3.2 and 3.3. The wafers are depicted by the gray boxes. The beam path is shown with the transparent orange box, moving toward the negative Y direction.

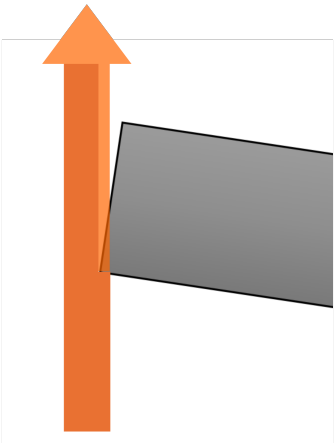

Figure 3.3: Schematic drawing of the transmittance due to wrongly oriented wafers. The beam travel direction is from the bottom to the top. Note that the angle in this image is exaggerated to demonstrate the issue.

A graph showing the relation of width versus angular offset can be found in Figure 3.4b. The graph specifically shows how far from the edge the point lies where the transmittance drops to 1% intensity, as depicted in Figure 3.3. From Equation 3.3 it can be found that this is at the point where the thickness of the silicon in the beam path is $23\ \mu\mathrm{m}$. This transparent region effectively widens the slit, meaning that the diffraction angle of the outgoing wavefront is lowered. The central maximum of the outgoing wavefront should cover the entrance port of the interferometer. So, a lower diffraction angle means that there is less margin to align the beam path. If the diffraction angle becomes too low, the mirror system would be only partially illuminated, or not at all. A semi-transparent region of $100\ \mathrm{nm}$ is deemed acceptable, corresponding to a maximum angular offset of $4.5\ \mathrm{mrad}$.

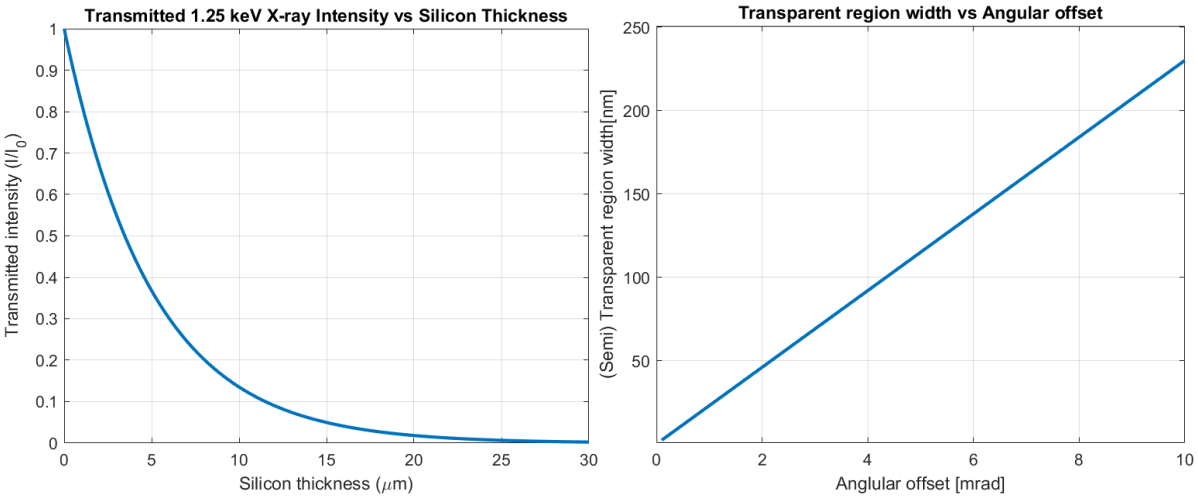

(a) Transmittance versus Silicon thickness

(b) Transparent region width versus Angular offset

Figure 3.4: Transmittance plots, made using data from CXRO. Figure 3.4b indicates how wide the semi-transparent region is versus the angular offset. A semi-transparent region of $100\ \mathrm{nm}$ is deemed acceptable, which corresponds to an offset of roughly $4.5\ \mathrm{mrad}$.

The final challenge is the stability of the system over time. The x-ray fringe patterns needed to prove the functioning of the system take time to form, as they are made up of individual photons (Tonomura et al., 1989). Due to a low expected count rate (den Hartog et al., 2020) the camera will need to be exposed for about one hour per measurement. This requires the mechanism to remain stable over this exposure time. There are two main disturbances that can affect the stability of the mechanism: temperature changes and external vibrations.

Figure 3.5 presents a plot of the temperature over a week, from a thermometer mounted on the vacuum system. It shows that over a day (1440 minutes), the total temperature change is about $0.1 - 0.2°\mathrm{C}$. For aluminium, this results in $2\ \mu\mathrm{m}$ displacement over $1\ \mathrm{m}$ length. For the length scale of the mechanism, which is roughly $60\ \mathrm{mm}$ this results in a maximum thermal expansion of about $0.12\ \mu\mathrm{m}$ over the full design domain. So, thermal expansion is not something that necessarily needs to be accounted for during the design phase.

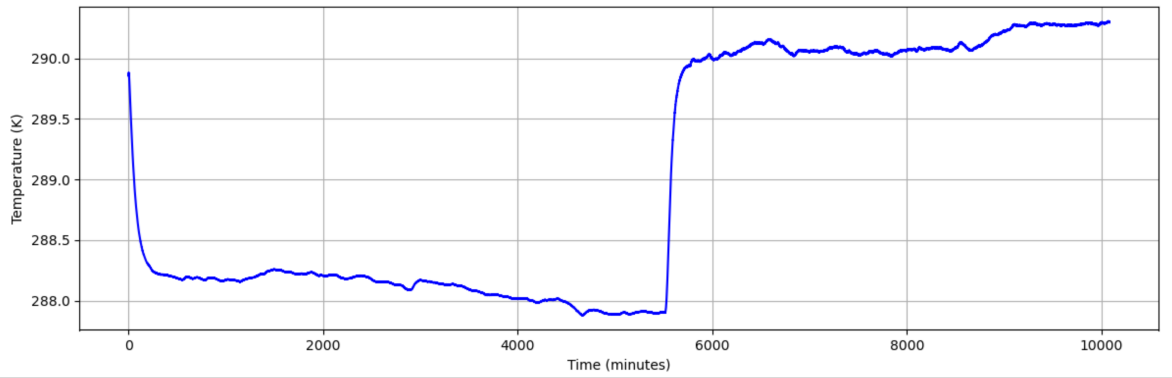

Figure 3.5: Plot of the temperature over a week, measured each minute. The temperature is given in Kelvin. The thermometer was placed on a blind flange of the vacuum system. The drop at the start of the plot is a result of the vacuum turbo pump cooling after shutdown. The sudden change half way through the measurement is the vacuum turbo pump turning on. Data provided by Aditya Garde.

To measure the environmental vibrations, seismometers and gyroscopes were placed on a metallic slab in the lab at SRON where the setup will be placed. Figure 3.6 shows these measured seismic vibrations. It can be seen that at $50\ \mathrm{Hz}$ a final peak is present above the urban noise floor. So, the mechanism should have a minimum eigenfrequency above this peak to avoid resonance.

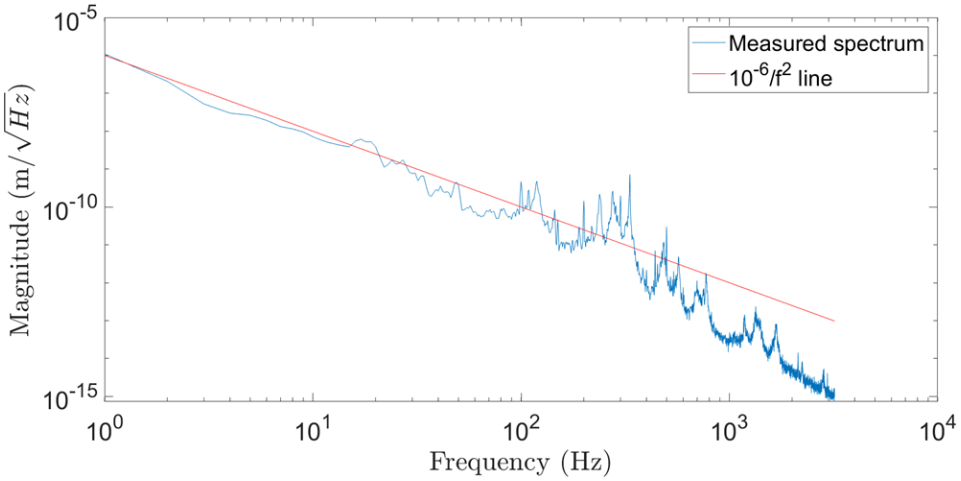

Figure 3.6: Seismic noise levels measured in the lab where the test bed is built. The X-axis shows the frequency in Hz and the Y-axis shows the magnitude of the seismic displacement. The red line indicates the seismic level of $10^{-6}/f^2\sqrt{\mathrm{Hz}}$ present in urban environments. Data provided by Aditya Garde.

3.4. Design criteria

As mentioned in the introduction, at the start of this project the fundamental slit mechanism concept was predetermined and, therefore, not subject to redesign. The main efforts for the design phase were focused on finding the right dimensioning for the chosen mechanism concept and the design of the supporting subsystems. This includes the actuation, mounting, and integration into the vacuum system. Consequently, the design challenge is mostly a challenge of integration and implementation,

rather than a structural challenge. The design criteria mentioned here are therefore aimed at comparing implementation strategies, rather than a comparison of different structural concepts.

The mechanism will be mounted in a confined vacuum environment with limited access ports. As will be discussed in later Chapters, the loads present in this system are not high. Consequently, the performance criteria do not need to be focused on structural and kinematic performance, but on practical aspects such as manufacturing feasibility and costs. The design volume is limited, and once the mechanism is installed it is difficult to access. Thus, complex assembly processes and required manual adjustments are undesirable. In addition to this, components with intricate details an small features are more prone to manufacturing errors and damage during handling. Thus, overly complex parts are undesirable.

- Costs. As there is a budget to adhere to, material cost, manufacturing costs, and required post processing steps should be minimised.
- Manufacturability. Components should be manufacturable with minimal specialised tooling and without many intricate features.
- Ease of assembly. The mechanism should be installable without the need for manual adjustments inside the vacuum system.

3.5. Constraints

As the source that produces the X-ray light uses a high voltage anode and cathode, the system needs to be placed in vacuum to avoid arching of the anode and cathode. This places multiple constraints on the system. First of all, the materials used should be vacuum compatible. Additionally, the vacuum system itself is limited to off-the-shelf parts which offer limited space to work in. The design domain therefore is fixed (Figures 3.7a and 3.7b). It is the inner domain of a six way vacuum cross. The thin cylinder seen on the left side of the domain is part of the X-ray source. This is where the slit should ideally be located. The mechanism has to fit inside this shaded domain.

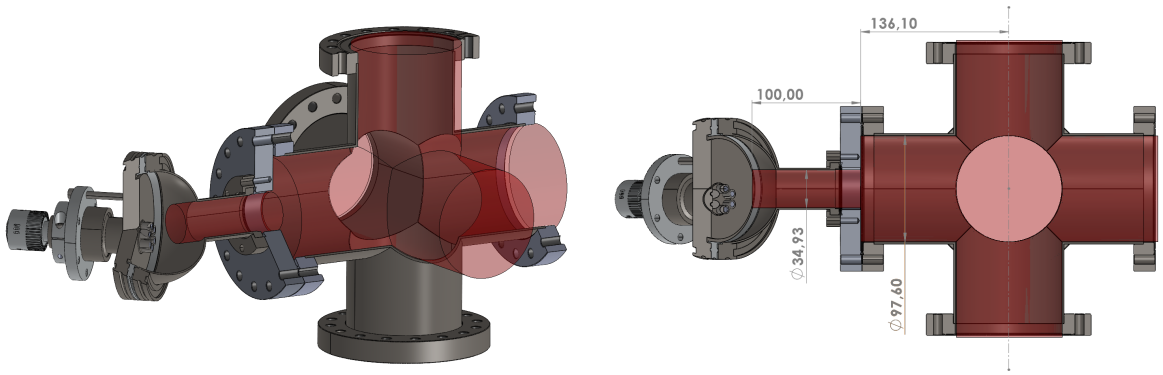

(a) Design Domain Bounding box isometric view

(b) Design Domain Bounding box including critical dimensions

Figure 3.7: Overview of the design domain and its bounding box dimensions.

4

Compliant mechanism design

In this Chapter, the design strategy and design for the slit system using traditional design techniques will be discussed. At the start of the design phase, it was decided that a prototype designed in earlier work would be used as a basis for the motion guidance for the slit mechanism. However, this mechanism was not yet adequate for the vacuum system. Furthermore, actuation and mounting solutions need to be developed for the system to function.

First, an overview of the slit mechanism will be given in Section 4.1. The mechanism concept, snout design, wafers that define the slit, and the actuators are described. Then, in Section 4.1 the mounting system is elaborated, including the integration into the vacuum system and mounting of the actuators. Then, Section 4.4 analyses the detailed design of the mechanism. The crucial design parameters are analyzed, along with the parameter optimization done to find these design parameters. Finally, validation of the mechanism using simulations is presented.

4.1. System Design

As discussed in Chapters 1 and 3 the slit mechanism will operate in a vacuum system. The XRI test bed consists of 4 major sections. The X-ray source, a six way cross in which the slit mechanism is mounted, a vacuum tube which will house the optical bench, and the detector. The six way cross is the crucial zone for this mechanism. The cross' primary purpose is to provide ports to mount a pressure gauge, turbo pump and getter pump, and allow interfaces for wiring to transfer electronic signals into the vacuum. It is an off-the-shelf part that does not have ports meant for internal mounting of parts. As such, the mounting system for the mechanism to the vacuum system needs to be designed. Actuation will be provided using off-the-shelf actuators.

4.1.1. Mechanism concept

The basic design that will be utilized for the translational motion is a simple four-bar-notch block as depicted in Farhadi Machekposhti et al., 2015 (Figure 4.1a). The flexures found in this Figure are Circular Notch Joints (CNJ, Figure 4.1b). These CNJs were chosen for multiple reasons. Firstly, as the mechanism is to be made from Aluminium using wire EDM the joints need to be compatible with this technique. CNJs are primitive planar flexure that have a simple geometry. Secondly, the joint offers relatively large DoC stiffnesses with very low axis drift. Lastly, a full analytical analysis of all the stiffnesses and range of motion was available, allowing them to be used in an analytical optimization.

Two parallel rigid links with CNJs are utilized to provide parallel translational motion. The two links are connected by a rigid bar. Under this bar material is added on which one wafer can be mounted to provide one of the edges for the slit. This material is placed such that room is still available below the bar for a rotational degree of freedom to be added. The rotational motion is provided using one notch flexure mounted to the same plane where the two links are mounted. On top of this flexure, material is added which provides the mounting for the second wafer. The basic design for the mechanism can be found in Figure 4.2.

A key advantage of using this setup is the relative simplicity of the mechanism. Increased design complexity results in smaller feature size, which complicates manufacturability and can reduce robustness of the design. A downside of not placing the flexure for the rotation at the center of the slit edge is the

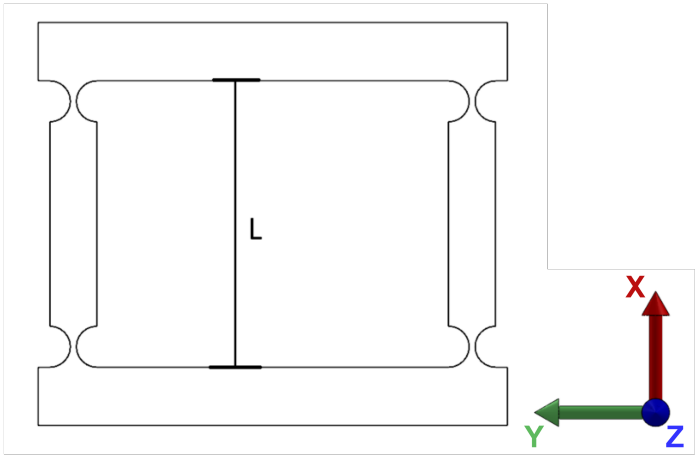

(a) Four-bar-notch block.

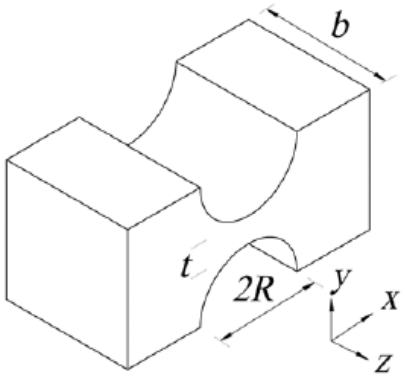

(b) Schematic of a circular notch joint.

Figure 4.1: Overview of the four-bar-notch block and circular notch joint, from Farhadi Machekposhti et al., 2015

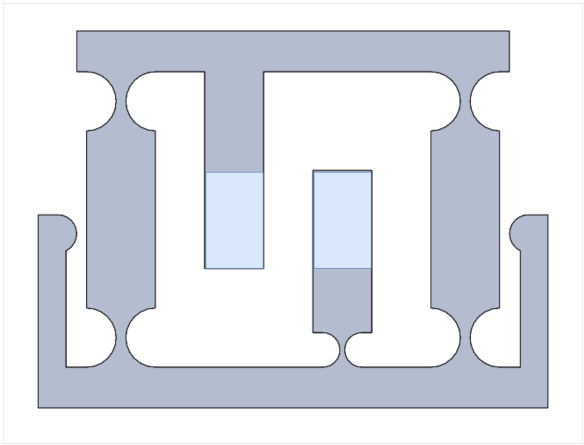

Figure 4.2: Base mechanism design. The locations where the wafers forming the slit are mounted are indicated in blue.

obvious coupling between rotation and translation. Although this is an issue, we can actively monitor the interference pattern at the camera. Changes in the width of the slit will immediately be apparent at the camera and thus can be accounted for.

Another advantage is the relatively compact design in combination with its simplicity. The space available for this mechanism, including its peripherals, has a diameter of $97.6\ \mathrm{mm}$, as shown in Figure 3.7b. This already forces the mechanism to be quite small in size, roughly $45 \times 55\ mm$, due to the space needed for mounting hardware and the actuation. Adding small details in an already small design domain will result in small features with higher manufacturing tolerances.

In the design shown there are four critical parameters that must be chosen carefully and directly impact the performance of the mechanism. They are:

- The minimum thickness of the flexure hinges, t.
- The radius of the flexure hinges, R.
- The thickness of the mechanism, b.
- The length of the rigid links, L

The considerations that are made in picking the right values for these parameters will be discussed in Sections 4.4 and 4.5. The flexure thickness, flexure radius, and mechanism thickness are defined in

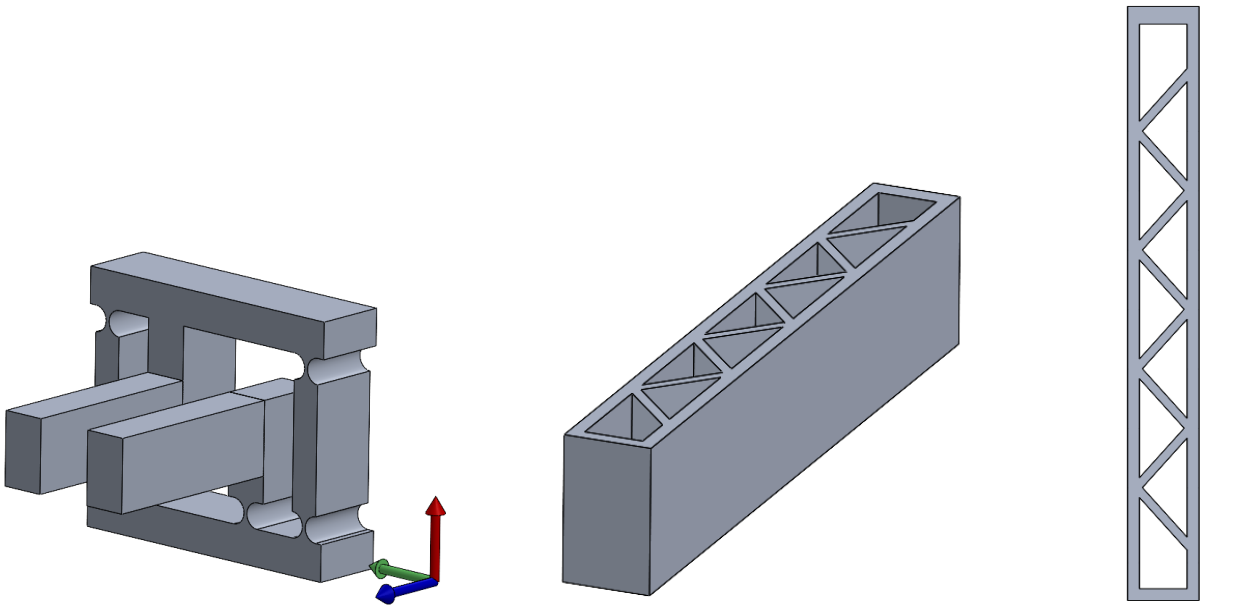

(a) Mechanism with simplified snouts

(b) Lightweight snout design

(c) Top view of the lightweight snout design

Figure 4.3: Design of the snout extension

Figure 4.1b. The rigid link length is defined as can be seen in Figure 4.1a.

A final addition to the mechanism is to include end stops, designed in such a way that the mechanism cannot be over actuated, preventing plastic deformation.

4.1.2. Snout design

As mentioned in Section 3.2, the slit must be placed close to the source. As seen in Figure 3.7a, it is evident that there is very little room to work close to the source. The diameter of the tube leading to the source is roughly $35\ mm$. A solution is to add a snout to the mechanism on which the wafers will be placed, which extends into the tube of the X-ray source. This is the simplest solution, as it requires very little adaptation of the mechanism. A simplified realization of this solution can be found in Figure 4.3a. The prerequisite is that the mechanism and snout are stiff enough to stay within the tolerances set in Section 3.3. Another method is to place the mechanism within the thinner tube of the X-ray source. However, the space in the tube is so limited that the chosen actuators cannot be placed in the tube. So, a transmission system would need to be designed between the slit mechanism and the actuation, which would be located in the six way cross. As the scope of this project was set as described in the introduction (1), these two ideas were not pursued further.

In order to improve the performance of the mechanism the weight of the snout should be minimized. This can be done by removing material in the center of the proposed snout. A minimum stiffness should be kept, so diagonal struts are added to the snout. Ideally material would be removed in two directions. However, to keep costs down and as simulations showed it would be sufficient, this is not done. Figures 4.3b and 4.3c show the final design of the snout.

4.1.3. Wafers defining the slit

The edges that define the slit are also an important point of attention. To actually produce a Fraunhofer pattern at the required $0.5\ \mu\mathrm{m}$ width of the slit for x-rays, the edge should be atomically smooth. To get such a smooth edge, silicon 100 wafers will be used.

As silicon 100 has a cubic crystal structure, silicon wafers can in theory be cleaved along the crystalline structure resulting in a perfectly straight edge. To ensure this actually happens, the wafer will first be partially etched, to give a predictable initialization point for the crack to propagate along the crystalline

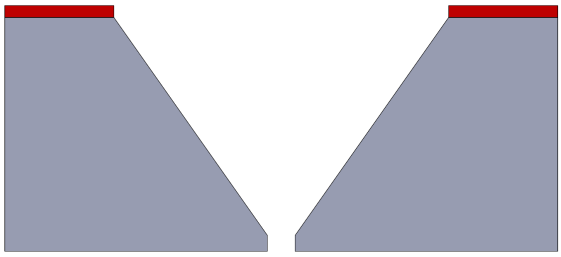

Figure 4.4: Schematic of a silicon wafer after etching and cleaving. The red portions indicate the etching mask.

structure. A mask will be applied to the wafer, aligned with the crystal structure. As the etching process starts, a V-groove will appear on the surface of the wafer. This groove is automatically aligned to the crystalline structure (Smith et al., 2015). By partially etching through the wafer this way, there will be a thinner weaker line in the wafer. This line can then be used as a starting point for the breaking, giving control over the break location. After the wafer is cleaved in two, a straight, smooth edge should ideally be formed. By controlling the etching depth, it can be ensured that enough material remains to reduce x-rays transmittance, as discussed in Section 3.3. Figure 4.4 shows a schematic of the wafers after cleaving.

Two wafer orientations were used during the testing of the mechanism, which will be discussed in Chapter 6. The standard symmetric mounting (Figure 4.5a) and an alternative mounting orientation designed to prevent the wafers from making contact and incurring damage (Figure 4.5b). To achieve this, one of the wafers is placed on a wafer of the same thickness. The tape used to bond the two wafers is used to provide 50 micron separation.

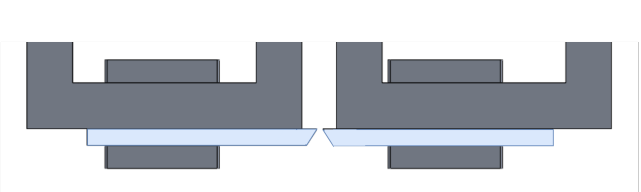

(a) The symmetric wafer orientation

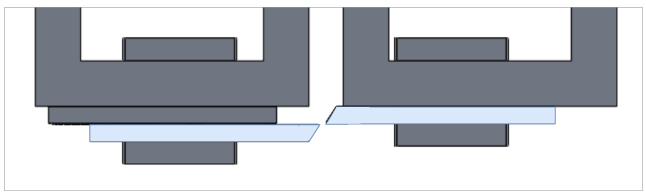

(b) The asymmetric wafer orientation used to prevent the wafers from making contact. The offset between the slit edges is $50\ \mu\mathrm{m}$.

Figure 4.5: The two used wafer orientations as mounted on the snouts using magnets. The wafers are indicated in blue.

As outlined in Section 3.3, the wafer planes must be perpendicular to the incoming X-ray beam. For the chosen design, there is no capability to adjust the plane alignment incrementally using a mechanism. Therefore, achieving this required perpendicularity will rely on proper surface finishing during manufacturing, which is expected to meet the requirements. If it turns out to be insufficient, surface coatings can be applied to the wafers to decrease the degree to which X-rays can penetrate through the wafers.

4.1.4. Actuation

the two degrees of freedom are actuated with off-the-shelf actuators that were found to have sufficient step size resolution, range of motion and actuation force.

The selected actuator is a linear piezoelectric inertia actuator (Thorlabs MPIA10VF). They offer a typical step size resolution of $10 - 30\ \mathrm{nm}$ with a maximum stroke of $10\ \mathrm{mm}$. This step size is more than adequate for the required tolerance and eliminates the need for a transmission system. They have a maximum recommended preload of $13\ \mathrm{N}$. The preload is taken as the maximum actuation load that can be achieved with this actuator for further calculations. They are mounted using a threaded barrel and locking nut, providing adequate mounting stability for the static operation required.

The actuator is also self locking when not supplied with a voltage, which is ideal for the set-and-hold type application that is necessary. Once the desired slit dimensions are reached, no continuous power

or control is required.

The actuators operate using an open loop, so its displacement is not internally measured. However, the optical system can inherently measure the width of the slit through the Fraunhofer pattern produced, and can be verified using Equation 2.1. Therefore, closed loop feedback is not necessary, as the measurement system indirectly provides positional feedback.

Ideally, both halves of the slit are actuated in the plane of motion. However, due to spatial constraints only the translation motion can be actuated in-plane. Instead, a lever arm is added to provide out of plane direct actuation for the rotational DoF. This keeps the direct actuation while maintaining mechanical simplicity.

Figure 4.6 shows the two actuation planes, highlighted in cyan and pink.

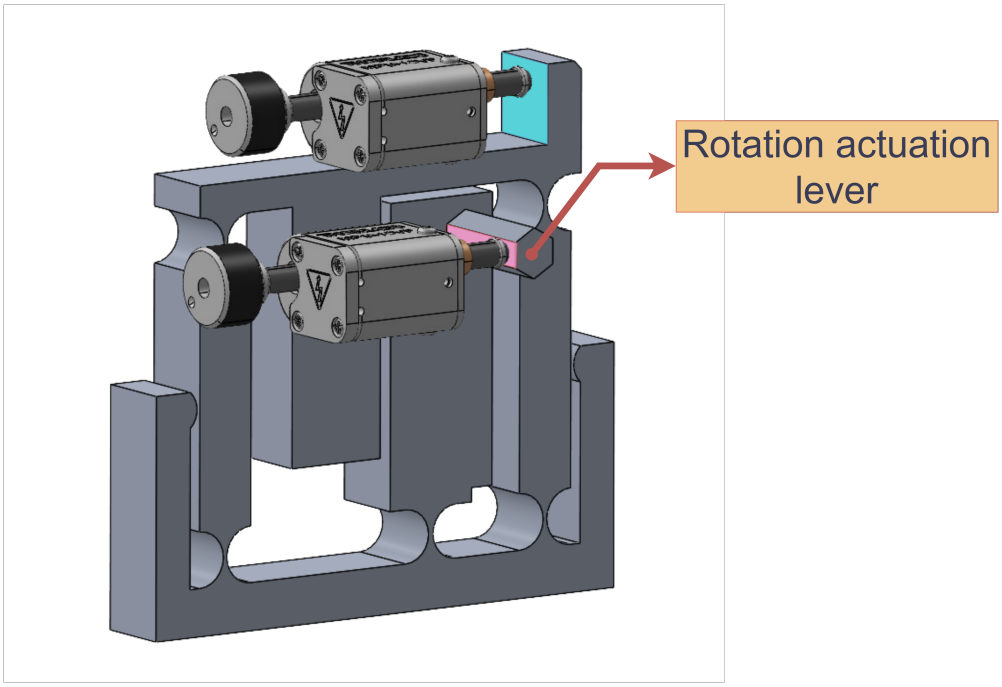

Figure 4.6: Actuator positioning relative to the mechanism.

The out of plane actuation will induce a moment on the hinge and thus small parasitic rotations. This will result in parasitic motions at the wafer, which must be kept in check. This is the most important point to consider when determining the exact dimensions of this hinge, which will be discussed in Section 4.5.5.

4.2. Mounting design

4.2.1. System mounting in the vacuum cross

The system has to be placed in the vacuum system, so requires a mounting system that fits in the available space but also must be compatible with the assembly procedure. The six-way cross, in which the mechanism will be installed, has a maximum inner diameter of $97.6\,mm$. The limited space available limits not only the design possibilities but also the possibility of assembling or adjusting components inside the vacuum cross. Therefore, the mounting was designed to allow complete assembly outside of the vacuum cross. Then, the entire assembly can be inserted at once. The chosen mounting method is to directly mount the mechanism to the vacuum system blind flange using a mounting platform placed on partially threaded rods. By drilling two threaded holes in the vacuum flange, the position of the whole system can be determined. Once the mechanism is attached to the flange, the flange can be mounted to the vacuum cross completing the assembly (Figure 4.7). This approach simplifies the assembly process, reduces the risk of misalignment, and avoids the need for adjustments within the

confined vacuum volume. The chosen support both gives the required structural support and offers initial alignment in the optical setup.

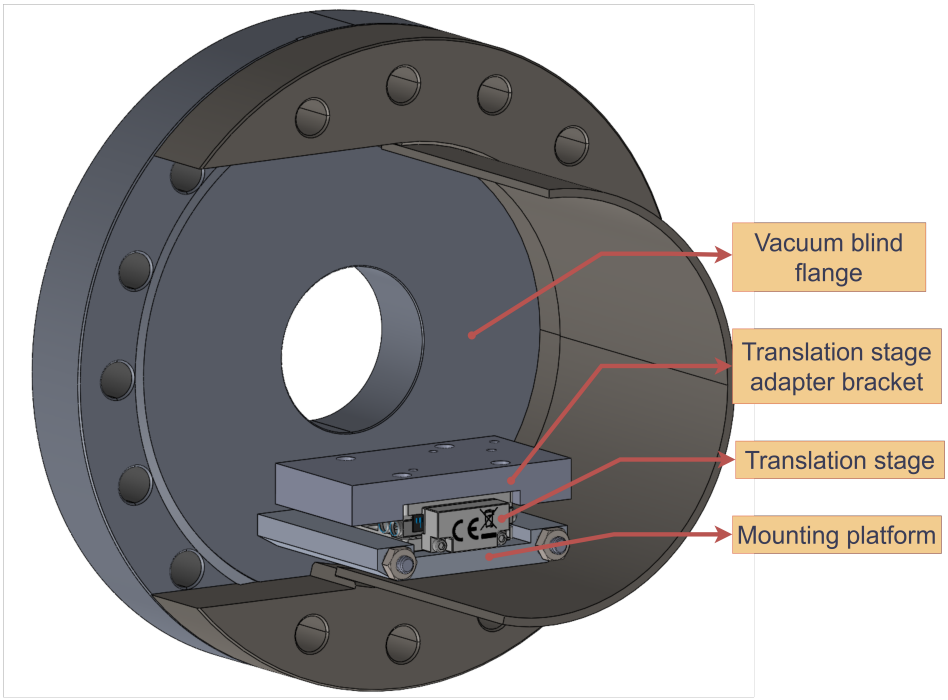

Figure 4.7: The mounting platform attached to the vacuum blind flange, including the translation stage and adapter bracket and a partially cut-away section of the six way vacuum cross.

4.2.2. Translation stage

As established in Section 3.3, the middle of the slit should be kept in position during operation. The selected slit mechanism concept provides only one translating DoF. Consequently, when the slit is closed, the center of the slit moves by half the displacement of the translating wafer. As described in Section 3.3, this can lead to smearing or loss of the fringe pattern.

To remedy this, a translation of the whole slit assembly is required. Rather than redesigning the slit mechanism, the mechanism and the actuators are mounted on a linear translation stage. This adds a second independent DoF. The slit width is determined by the movement of the individual wafers. The location of the optical axis is corrected by the translating stage. This decouples the slit adjustments from the optical alignment.

A vacuum compatible piezo linear translation stage (Thorlabs PD1XAV) was selected. The stage provides closed loop actuation with a nominal step size of $300\ \mathrm{nm}$. This is sufficient to correct for the displacement of the center of the slit. The translation stage is a compact low profile design ($30\ \mathrm{mm}$ height) that allows integration with the limited vertical space available. It supports a maximum off axis load of $3\ \mathrm{kg}$, so it can support the weight of the unsymmetrical mechanism.

In order to mount the various parts that are needed for the mechanism to work, an adapter bracket was designed. An image of this bracket mounted on the translation stage can be found in Figure 4.7, along with the mounting design to the vacuum system, as mentioned in the previous section. The translation stage therefore ensures that the slit adjustment does not alter the optical alignment of the system.

4.2.3. Actuator mounting

The function of the actuator mounting is to position the actuators whilst preserving the optical beam path from the slit to the optical bench entrance ports. Due to the relatively low loads of at most $26\ N$, which is not the typical operating force, the problem is more of geometric placement rather than structural strength. The chosen design can be found in Figure 4.8. The main reason for this is the simplicity of

the integration with the translation stage. Only one mounting point has to be considered at the bottom of the bracket.

Of course, this bracket is not infinitely stiff. It will also deform as a result of the force applied by the actuators. This deformation can easily be found using a structural FEA. For the combined actuation force of the actuators, the maximum deflection of the mounting points is about $2.5\ \mu\mathrm{m}$. Although this will affect the width of the slit, as the slit size is measured directly during operation this can be compensated for. The deformation therefore affects only the actuator displacement required to achieve a given slit width, rather than the achieved slit dimension itself. Furthermore, the deflection is only in the actuation direction and does not affect the other tolerances of the beam path. Additionally, it is unlikely that both actuators will be loaded to their maximum force. The actual displacement will be lower. Because the deformation is bounded, repeatable, and does not obstruct the optical path, the mounting stiffness is sufficient for the functional requirements of the system.

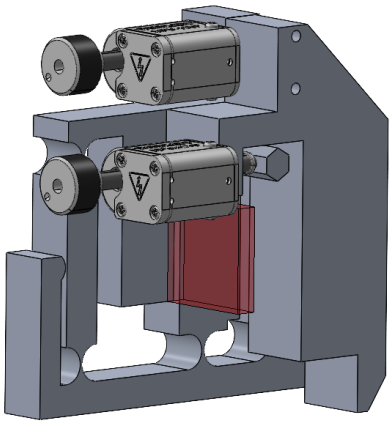

(a) The actuator mounting system including both actuators. The transparent red box shows the exclusion zone where nothing should be placed to avoid blocking the beam path.

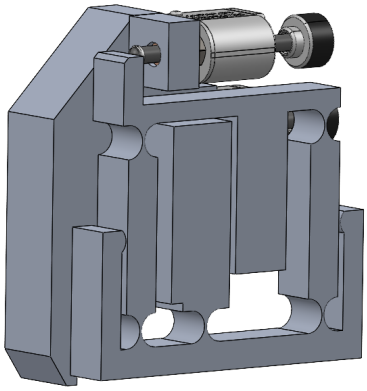

(b) The full actuator mounting shown from the opposite side.

Figure 4.8: Overview of the designed actuator mounting

4.3. System overview

This Section will be used to show overviews of the final design, both in isolation and as assembled in the six way cross. Figures 4.9,4.10, and 4.11 show the fully assembled mechanism, both in isolation and as installed in the vacuum system.

Alternate designs considered for the mechanism and actuation (mounting) can be found in Appendix H.

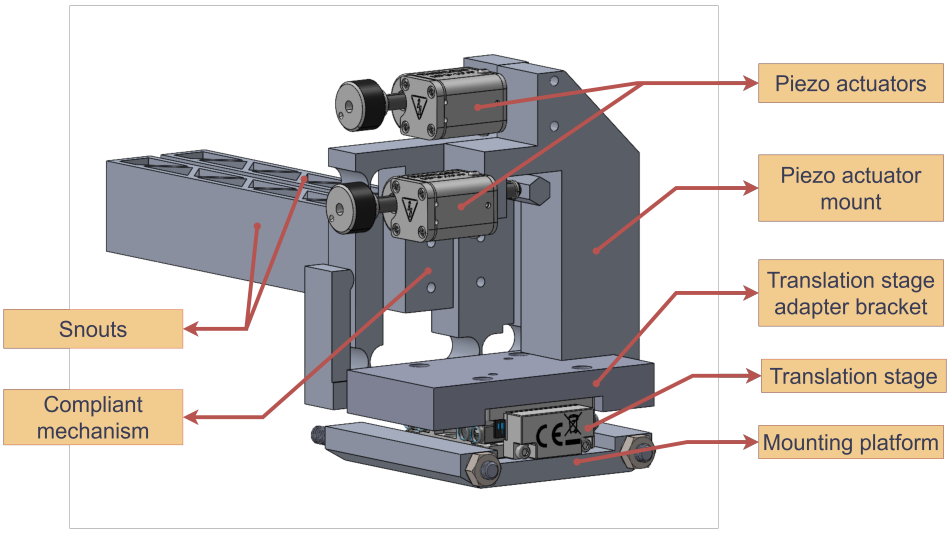

Figure 4.9: Complete design in isolation

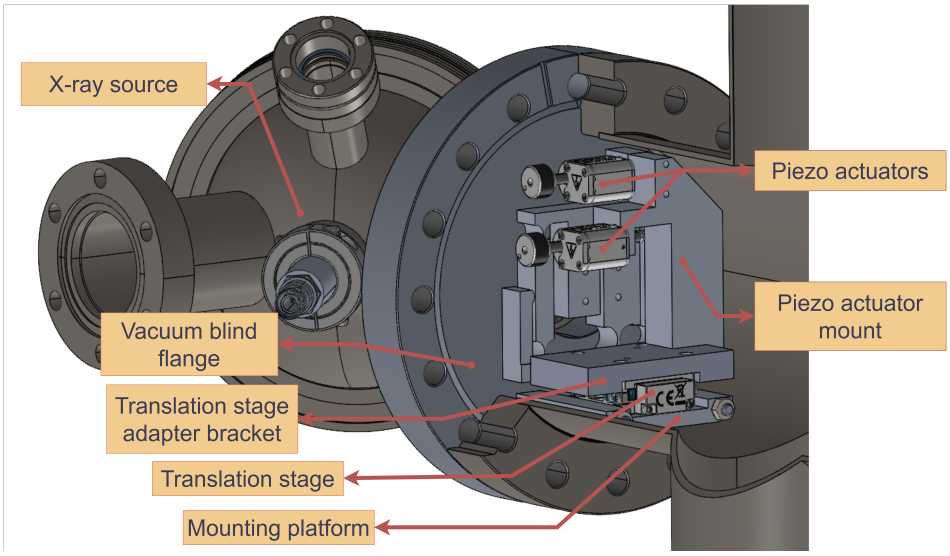

Figure 4.10: View of the mechanism as installed in the six way cross. On the left is the X-ray source. To the right is the direction of travel for the X-ray beam.

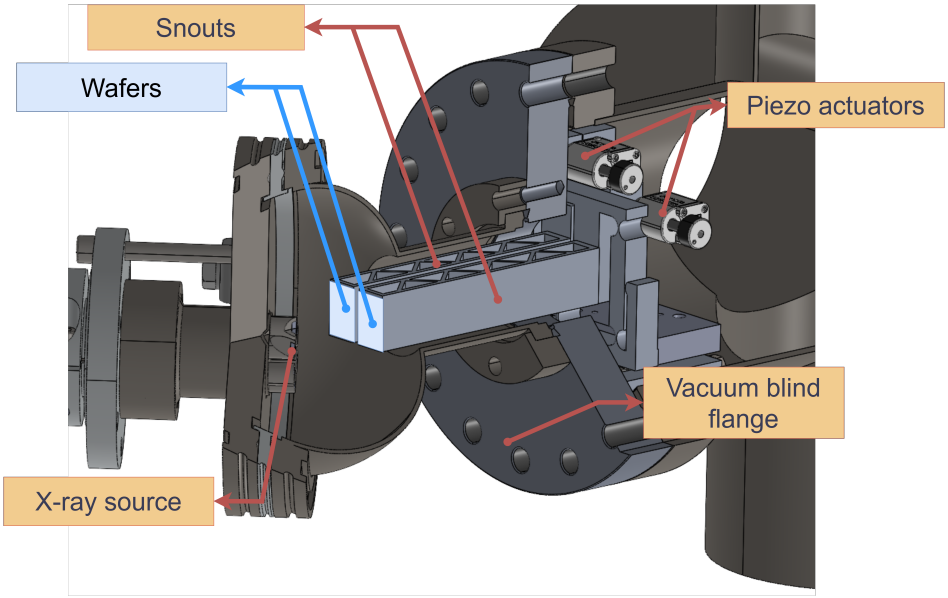

Figure 4.11: View of the mechanism as installed in the six way cross, including a view of the snout as extended into the X-ray source.

4.4. Mechanism detailing

4.4.1. Flexure parametrization

The dimensions of the hinge largely determine the range of motion of the mechanism. This can be seen easily by looking at the Equations for the angular range of motion of the CNJ from Farhadi Machekposhti et al., 2015:

$$\theta_z = \frac{\beta_1^2 \beta_2}{E(1+\beta_1)^{9/20}} \sigma_y \tag{4.1}$$

$$\beta_1 = \frac{t}{2R} \tag{4.2}$$

$$\beta_2 = \frac{3\pi}{(2\beta_1)^{5/2}} \tag{4.3}$$

The angular range of motion is determined by four parameters. The yield stress σ_y and Young's modulus E of the material used, the minimum thickness of the flexure t, and the radius of the flexure R. To obtain the total range of motion of the connecting bar of the mechanism, the angular range of motion should be multiplied by the length of the rigid link L. Figure 4.1b gives a more detailed view of the circular notch flexure, including the axis orientation for all Equations in this Section. Combining Equations (4.1) to (4.3) gives a clearer picture of how each parameter influences the angular range of motion:

$$\theta_z = \frac{3\pi t^2 \sigma_y}{4ER^2 \left(\frac{t}{R}\right)^{5/2} \left(\frac{t}{2R}+1\right)^{9/20}} \tag{4.4}$$

The relation between the Young's modulus E and the Yield stress σ_y with the range of motion is quite apparent. Increasing or decreasing either value linearly increases or decreases the angular range of motion. Finding the right material is thus of great importance. For this design, Aluminium 7075-T6 was selected for its low costs, good manufacturability, low weight, and relatively high yield strength. A complete discussion on material selection can be found in Appendix D. The relation between R, t and θ_z is less clear. Generally speaking it can be concluded that increasing t decreases the range of motion and increasing R decreases the range of motion. However, this is not a linear relationship. So, choosing these values is not necessarily an intuitive decision. This problem is amplified as the radius and thickness also influence the stiffness of the hinges, and thus the stiffness of the mechanism. As the chosen actuators have limited input force, there is also a constraint on how stiff the hinges may

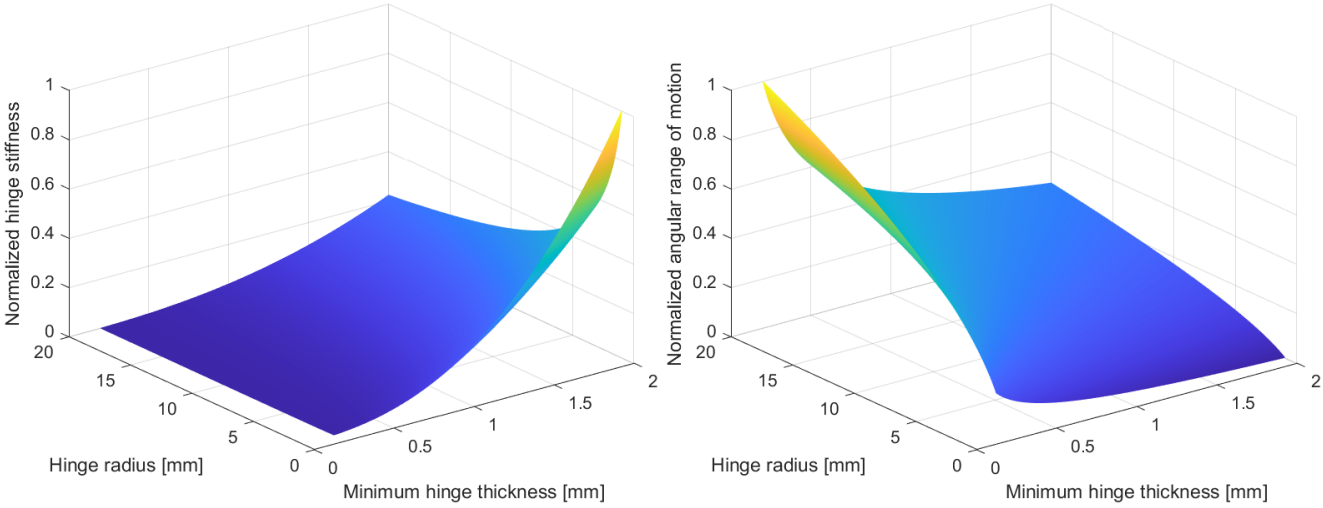

(a) Circular notch joint min-max normalized stiffness for R vs t

(b) Circular notch joint min-max normalized range of motion for R vs t

Figure 4.12: Surface plots showing the normalized hinge stiffness and angular range of motion for R and t.

be. The rotational stiffness of the hinge can be determined using the following Equation, also from Farhadi Machekposhti et al., 2015:

$$K_{\theta_z} = \frac{2Et^{5/2}b}{9\sqrt{R}\pi} \tag{4.5}$$

Again, there is a trade-off between the radius of the flexures and the minimum flexure thickness. The complexity of setting the correct hinge parameters becomes more apparent from this Equation for the stiffness. Figures 4.12a and 4.12b demonstrate the relation between the design parameters and the range of motion and stiffness. Firstly, it is evident that the stiffness and range of motion are conflicting parameters. Increasing the range of motion generally decreases the stiffness, and vice versa. Secondly, neither plot shows linear behavior for the relationship between the design parameters and the resulting parameter.

Another parameter is also added, b. This is the thickness of the plate out of which the mechanism will be made. This not only affects the in plane rotational stiffness K_{θ_z}, but it also influences the out of plane stiffness K_{θ_x}. As mentioned in Section 4.1.2, a snout will be placed on the mechanism to position the slit closer to the source. To stay within the set tolerances, the out of plane stiffness, K_{θ_y}, should be kept sufficiently high. The equations for the out of plane stiffness can be found in Appendix E.

The combination of these and more constraints makes this a complex problem for which to find an adequate solution. Choosing the four parameters manually would be both tedious and difficult to ground in proper reasoning. As such, it was decided to utilize parameter optimization to find the 'best' parameter values for the design case presented *for the translational DoF*. This parameter optimization will be further discussed in Section 4.5. The parameters for the rotational DoF are set partially manually and partially from the parameter optimization, which will be discussed further in Section 4.5.5.

4.5. Translation hinges parameter optimization

As discussed in Section 4.4.1, the complexity of the parameter choice requires a parameter optimization. Since the analytical equations used to describe the circular notch hinges and four-bar-notch block are available from Farhadi Machekposhti et al., 2015, this is possible. The combination of the objective function and constraints determines how the final design looks. So, it is crucial that they are defined properly. Similarly to topology optimization, this is also where the designer can have influence on the final results.

4.5.1. Objective function

Choosing the right objective function for an optimization is crucial for the final result. For this particular optimization problem there are many possibilities and choosing the right one depends on what is perceived as the biggest hurdle for the mechanism to overcome. In this Section, the objective function that was ultimately chosen for this optimization is presented.

The objective function for this optimization problem is to maximize the stiffness of the hinge, with a bias towards the hinge thickness. The objective function is:

$$f = -K_{\theta_z} \cdot t = -\frac{2Et^{5/2}b}{9\sqrt{R}\pi} \cdot t \tag{4.6}$$

Here K_{θ_Z} is defined in Equation 4.5. The choice for a bias towards thicker hinges is mainly practicality. A decrease in hinge thickness directly leads to higher manufacturing tolerances, which increases the chance of fabrication defects or failures. As such, at the request of the manufacturer, and as a measure to reduce cost and lead time, the hinges were optimized for maximum hinge thickness within the constraints set for this optimization problem. There are downsides to this bias towards hinge thickness, which will be discussed in Section 4.5.4.

Maximizing the stiffness of the DoF of the hinge was selected as the objective as it provides an indirect way of increasing the minimum eigenfrequency of the mechanism. As outlined in Section 3.3 on the performance requirements, there is a floor above which the eigenfrequency of the mechanism must lie. Ideally, this minimum eigenfrequency would be added directly to the optimization problem as a constraint. However, this would require the addition of a finite element analysis to the optimization loop. Although this is possible, setting it up was deemed out of scope due the associated time and effort. The alternative is to use a simplified version of the problem. For a simple single DoF mass-spring system, the natural eigenfrequency can be determined using:

$$\omega = \sqrt{\frac{k}{m}} \tag{4.7}$$

As the hinges ultimately will have very little impact on the total sprung mass of the system, increasing their stiffness will directly result in an increase in eigenfrequency.

To summarize, the problem to be solved is to choose the design variables such that a mechanism is achieved with sufficient eigenfrequency. Manufacturability is a second objective that needs to be considered. The objective of the optimization is to maximize the rotational stiffness and the thickness of the hinge. The ultimate goal is to provide an indirect maximization of the minimum eigenfrequency whilst ensuring manufacturability and robustness by avoiding arbitrarily thin hinges.

4.5.2. Constraints

There are four constraints used to further steer the optimizer to usable hinge parameters.

Minimum range of motion constraint

Firstly, there is a constraint on the minimum range of motion the mechanism. This constraint is directly in conflict with the objective function. Figures 4.12a and 4.12b show of this conflict. For the given design space, the effect of the design parameters is nearly opposite for the stiffness and range of motion of the hinge. The range of motion largely determines the range of motion of the mechanism. The exact formulation given in negative-null form is:

$$\frac{\delta_X}{1\ [mm]} - 1 \leq 0 \tag{4.8}$$

The range of motion of the four bar notch block is defined in Farhadi Machekposhti et al., 2015 as:

$$\delta_X = (L - 2 \cdot R) \cdot \sin(\theta_Z) \tag{4.9}$$

In this Equation, L is the link length, R is the hinge radius, and θ_Z is the angular range of motion of the hinge, as defined in Equations (4.1) to (4.3). The minimum range of motion that is needed is

0.5 mm as mentioned in Section 3.3. However, as an additional factor of safety to steer away from the absolute limit of the yield strength, the required range of motion is set to 1 mm. Equation 4.4 shows that θ_Z is defined as the angular range of motion that is just on the limit of the yield strength of the specified material. Analytically, using this limit is okay. Practically, this is not necessarily a wise decision. In reality, without appropriate tests there is always some uncertainty around what the precise yield strength of a material is. This means that the yield stress could accidentally be crossed, leading to plastic deformation of the hinges. Furthermore, the number of load cycles before fatigue failure reduces when the operating stress is closer to the yield stress. Figure 4.13 shows the fatigue stress model for Aluminium 7075-T6. At 400 MPa, the expected amount of cycles till failure is between 100 and 200. To increase both robustness of the design and increase the number of expected duty cycles, a lower maximum allowed stress is used. The specific value set was found through a combination of trial and error and discussion with Instrument scientists at SRON. Setting it to the fatigue strength would be a logical choice. However, for Aluminium 7075 T-6 this limit is too low to achieve the required range of motion for the available design space. Ultimately, 300 MPa was chosen. Figure 4.13 shows that at this stress level, around a 1000 load cycles can be expected until failure. At 300 MPa, a practical design can be found whilst offering enough duty cycles for the intended use of the mechanism.

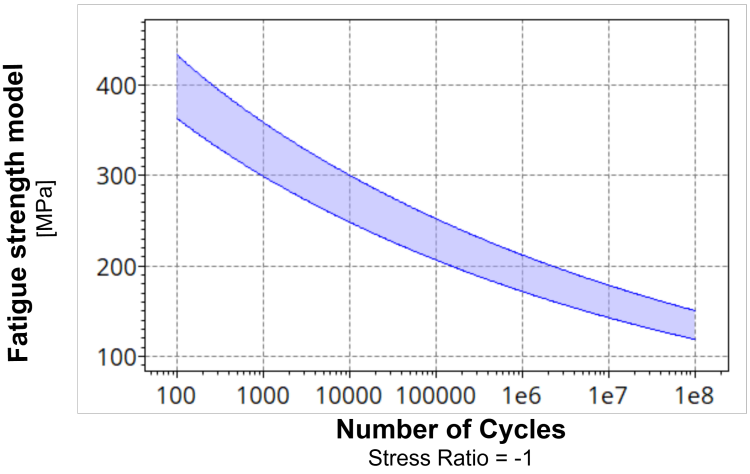

Figure 4.13: Relation between stress and number of cycles till failure for Aluminium 7075-T6, from the Granta Edupack software package.

Maximum stiffness constraint

The second constraint is the maximum mechanism stiffness constraint. As the chosen actuators, which are discussed further in Section 4.1.4, have a limited maximum actuation force, the mechanism has a maximum allowed stiffness. The constraint following from this requirement is:

$$\frac{K_X \cdot \delta_X}{13\ [N]} - 1 \leq 0 \tag{4.10}$$

13 is chosen as this is the maximum preload for which the actuators are expected to work, as mentioned in Section 4.1.4. At and above this load, the actuators are not guaranteed to achieve their specified step size, or can even be unable to move. So, by controlling the stiffness of the mechanism in combination with the range of motion set the maximum actuation force that will be needed can be set. This allowed stiffness is specified at the actuation point. That is the rigid bar at the top of the four bar mechanism. The equation for the apparent stiffness of the bar is also given in Farhadi Machekposhti et al., 2015 and is defined as:

$$K_X = \frac{4K_{\theta_Z}}{(L - l_j)^2} \tag{4.11}$$

l_j is the length of the joints and is equal to $2R$. To ensure operation with the expected step size of the actuators, a margin is built in. This margin is guaranteed by the specification to set the required range of motion to 1 mm for the optimization problem, as discussed in the previous Section on the minimum

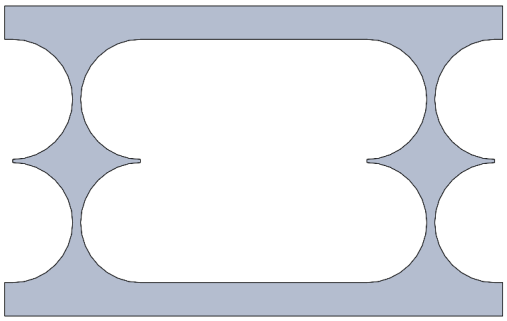

Figure 4.14: Joint length such that the link would be just the two joints

range of motion constraint. As this is more than the actual range of motion, it guarantees that, for the intended range of motion of 0.5 mm, the actuators operate to their specifications.

Link length constraint

The third constraint is used to ensure that the optimizer remains in the domain where the analytical model is valid. The analytical model assumes that the two compliant hinges are separated by a rigid link. In exploratory optimization runs, it occurred that the optimizer would find a parameter combination where the combined length of the notch joints was equal to or larger than the link length. When this happens, the structure no longer necessarily acts as two discrete hinges, but as one distributed compliant section.

Figure 4.14 illustrates the situation where the two hinges approach the total link length. At this point the structure no longer acts as two concentrated hinges, but rather as one distributed hinge, meaning the analytical equations used do not necessarily hold any longer.

To ensure that the optimizer acts in the regime where the analytical model is accurate, it was decided to enforce the link length to be at least three times the length of the notch joint. The factor three is chosen as a conservative estimate and is not necessarily the lower limit for which the analytical model holds. The constraint used in the optimization problem is the following:

$$-(L - 6R) + 1 \leq 0 \tag{4.12}$$

Thickness - Radius ratio constraint

Similarly to the constraint governing the link length, the equations used for these hinges do not necessarily hold for all ratios between the minimum thickness and radius of the hinge. Kuan Yong et al., 2008 shows that the equations for the rotational stiffness of the CNJ hold to below 6% error when compared to FEA results, for thickness ratios of $0.05 \leq t/R \leq 0.5$. Outside of this range of proportions, the error increases to a maximum of 12%. For the longitudinal stiffness K_x and shear stiffness F_y the error is much larger outside the given range. However, as the mechanism is not expected to be loaded along these directions and it does not affect the results of the optimization, this is not taken into account.

The employed constraints are:

$$-20\frac{t}{R} + 1 \leq 0 \tag{4.13}$$

$$2\frac{t}{R} - 1 \leq 0 \tag{4.14}$$

4.5.3. Parameter optimization formulation

To summarize, the full parameter optimization is as follows, with al constraints given in negative null form:

$$\min : K_{\theta z} \cdot t \tag{4.15}$$

$$s.t. : \frac{\delta_X}{1\ [\mathrm{mm}]} - 1 \leq 0 \tag{4.16}$$

$$: \frac{K_x \cdot \delta_x}{13[\mathrm{N}]} - 1 \leq 0 \tag{4.17}$$

$$: -(L - 6R) + 1 \leq 0 \tag{4.18}$$

$$: -20\frac{t}{R} + 1 \leq 0 \tag{4.19}$$

$$: 2\frac{t}{R} - 1 \leq 0 \tag{4.20}$$

4.5.4. Parameter optimization results

There are two limits that define the design space for this optimization problem. Namely, the maximum length of the links and the minimum plate thickness. The first is set to $46\ mm$, as this is the maximum length that would fit for the dimensions of the vacuum cross. The second is set to a minimum thickness $10\ mm$, as this ensures a minimum out of plane stiffness needed to avoid parasitic displacements due to gravity.

Without a lower limit on the plate thickness the optimizer will logically tend to the thickest hinge possible. To stay below the maximum stiffness set for the mechanism this will lead to lower plate thickness. This results in a very thin mechanism with very low out of plane stiffness.

Setting the minimum for this parameter manually instead of using a minimum out of plane stiffness is not immediately logical. The reason for not doing so is a result of the minimum eigenfrequency largely being determined by the thickness of the hinges. Multiple objective functions were explored for the design challenge. For each objective function, the eigenfrequency of the mechanism with added snouts was analyzed. From this analysis it became apparent that the minimum eigenfrequency largely depends on the thickness of the hinge.

Imposing a minimum out of plane stiffness results in lower hinge thickness and thus a lower eigenfrequency. Finding an out of plane stiffness ratio that is adequate whilst maintaining the eigenfrequency requirement proved to be trial and error. So, it is essentially equivalent to manually selecting the plate thickness. So, the choice was made to do this instead.

Running the optimization with these limits yields the following results for the flexures:

- Flexure thickness $t = 0.51$ mm
- Flexure radius $R = 3.52$mm
- Plate thickness $b = 10$mm
- Link length $L = 46$mm

Figure 4.15 shows the contour plot of the objective for t and R, with all constraint lines. It can be seen that the geometric constraints are inactive. The constraints on the required range of motion and maximum allowed stiffness are active. This is exactly the balance described in Section 4.4.1 between the range of motion of the hinge and its stiffness. The graph verifies that an optimal solution is in fact found for this optimization formulation. The contour plots for the other combinations of design variables can be found in Appendix E.

Using these found values results in the final geometry used for the mechanism, which can be found in Figure 4.16. Note that this optimization is used only for the hinges that provide the translational DoF.

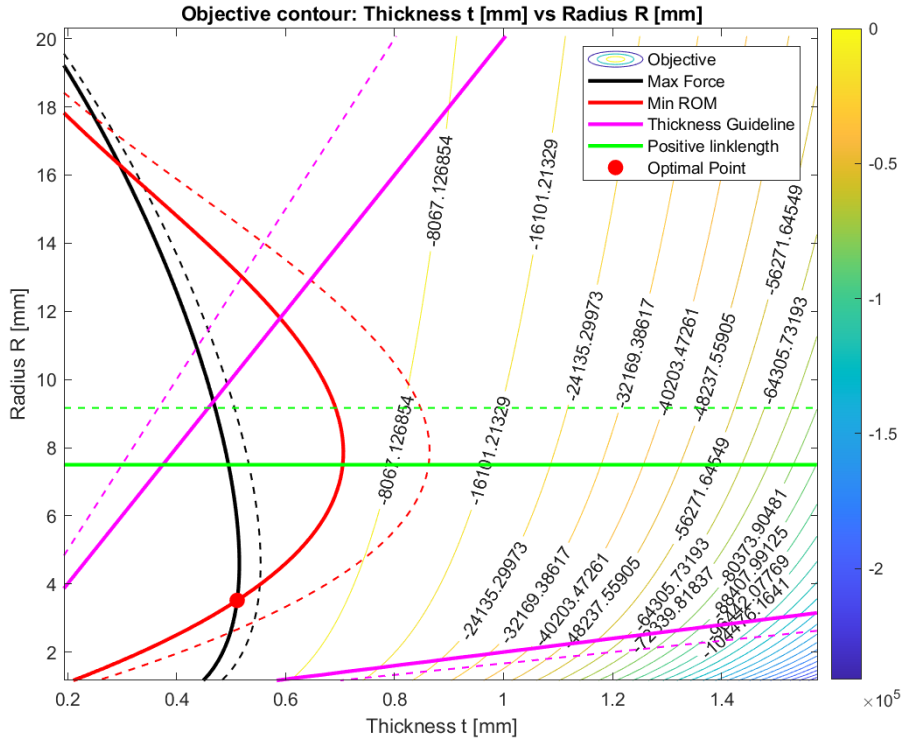

Figure 4.15: Contour plot of the objective function for the design space for t versus R. The dashed lines indicate the infeasible domain.

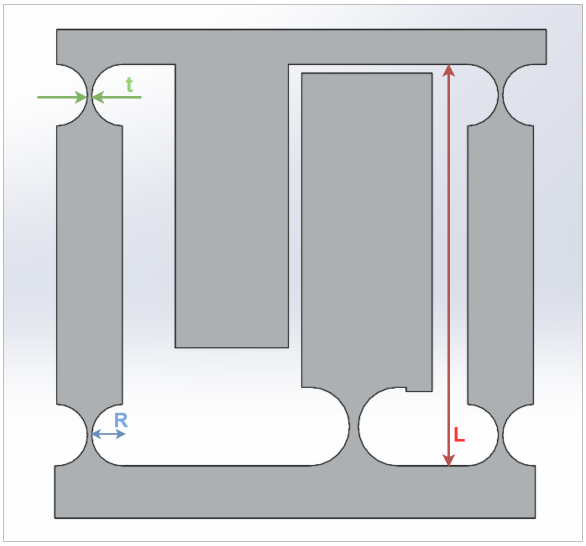

Figure 4.16: The mechanism with the dimensions found through the parameter optimization.

4.5.5. Rotation stage parameter choice

Although the parameters found through the parameter optimization are used for the translational DoF, they cannot be used directly for the rotational DoF. Where the translational DoF is provided by four CNJs, the rotational DoF is governed by only one CNJ. Using the parameters found in the optimization would result in a first eigenfrequency that is below the required $50\ \mathrm{Hz}$ set in Section 3.3. Consequently, the hinge parameters for the rotational hinge should be set differently from the parameters presented in the previous Section.

An additional challenge is the limited design space. As there is no room for in plane actuation for the

rotational DoF, a moment will be applied to the hinge, inducing a twisting motion. This twisting motion around the X-axis of the hinge is transferred to the wafers through the snout on which they sit (see Figure 4.1b for the axis orientation). The result of this is a parasitic motion at the slit in addition to the intended motion of the wafer.

The hinge geometry must be chosen such that the unintended motion at the wafer is kept within the performance limits set, in addition to the minimum eigenfrequency specified. The hinge design for the rotational DoF is therefore dominated by these two objectives. To keep the stiffness high enough for dynamic rigidity and directional stiffness to properly guide the motion.

Ideally, the hinge should be compliant in the intended DoF and kept stiff in the constrained direction. The ratio between the DoC and DoF stiffness determines how well the motion path is defined. A low ratio leads to relatively high parasitic displacements, while a high ratio would suppress the amount of parasitic displacements relative to the total output in the intended DoF cause by the out-of-plane actuation.

As the mechanism is made from a monolithic plate of Aluminium, the thickness of the plate b is controlled by the values found through the parameter optimization. The only open parameters that affect the hinge stiffness are the minimum hinge thickness t and the radius R of the notch. Analysis of the stiffness ratio shows that the radius R has little influence on the stiffness ratio. However, the minimum thickness t has a large effect on this ratio.

Decreasing the minimum thickness t increases the ratio between the two stiffnesses. This would improve the motion quality, and thus the parasitic displacement relative to the intended motion magnitude. However, this also directly leads to a reduction in the stiffness of the hinge and consequently the first eigenfrequency. Increasing the minimum thickness has the opposite effect. The stiffness and eigenfrequency increase, but the motion quality is lowered. As a stiffer hinge requires a larger actuation force, a larger moment will be applied to the hinge, increasing the relative parasitic motion. So, a compromise is needed. The hinge should be stiff enough to provide adequate eigenfrequency, but not so stiff that the out of plane actuation induces too large parasitic displacements. As discussed in Section 3.3, the minimum rotational range of motion required is $0.15°$. Counter-intuitively, the range of motion at maximum force input from the actuators should thus be higher than what is necessary from the performance requirements. This is done to reduce the parasitic motion at the output as a result of a smaller induced moment.

Looking back at Equation 4.4.1, the radius of the hinge can be used to reduce the stiffness. Making the hinge radius larger decreases the stiffness. Keeping the thickness high can be used to ensure manufacturability and the minimum eigenfrequency. This interplay can be used to find appropriate dimensions.

The chosen parameters for the hinge dimensions give a compromise between these competing objectives. The thickness t was chosen to give adequate stiffness for the required eigenfrequency, whilst keeping the parasitic motions in check. The radius helps in this problem.

Ultimately, the parameters were not chosen purely out of a structural perspective but from the need to control parasitic motions from the out-of-plane actuation. Specifically, a hinge radius of $4\ mm$ with hinge thickness of $1\ mm$ was chosen. As will be discussed in Section 4.6, these geometrical parameters ensure a rotational DoF that adheres to the performance requirements for typical operation.

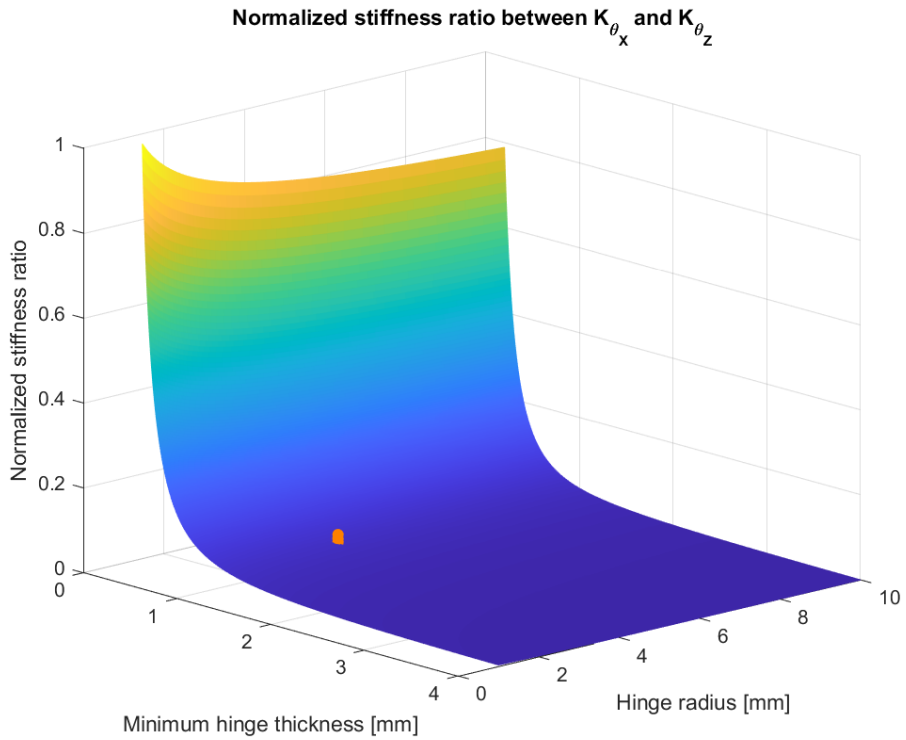

Figure 4.17: 3D surface plot showing the relation between design variables t and R with the ratio between DoF and DoC stiffness. The orange marker shows the chosen parameter values.

4.6. Mechanism performance validation

In this Section, the optimized design will be tested for the performance criteria set in Section 3.3 using COMSOL Multiphysics®simulations with geometric nonlinearity. First, the translation and rotation sides will be analyzed for the required range of motion, stiffness, and operating stress. Then, an eigenfrequency analysis will be performed to check whether the found dimensions result in an adequately high eigenfrequency. Finally, a check will be done on the parasitic displacement that occurs due to gravity.

4.6.1. Motion validation

To validate the motion path under force actuation, a simple stationary analysis in combination with a parametric sweep can be used. The mechanism is constrained at the bottom using a fixed constraint. The two load cases, namely the translation and rotation, are tested separately. For the translating half the actuation force is input in plane. Therefore, there should be no out of plane parasitic displacements due to the actuation force, so a 2D analysis is sufficient. For the rotating half this is not the case, as the actuation is out of plane. Table 4.1 shows the force displacement relation for both analytical equations and simulation. The difference in displacement from the two methods shows just over 5% difference. Generally, this means that the equations can be trusted. For the rotational degree of freedom, Table 4.2 shows the force deflection relation. Generally, a 10% difference is found where the simulated displacement is lower than that found in the analytical equations. This larger discrepancy is likely caused by simplifications taken for the analytical equations. Ideally, a pseudo-rigid-body-mechanism should be derived and analyzed. Generally, the behavior is close enough to accept that the simulation is likely accurate.

For the translating half the resulting displacements due to actuation are shown in Figure 4.18. The color distribution (the absence of a clear gradient) in this plot already hints at the fact that the motion resulting from the actuating force is generally okay. The maximum displacement is roughly $0.9\ mm$ for the maximum actuation force. So, the range of motion is adequate. There is a very slight rotation induced on the slit edge by the fact that the mechanism is actuated above the connecting rigid link. The parasitic displacements under actuation can be found in Table 4.3.

For the rotating half the actuation force is input out of plane. This causes a moment and rotation around

Force $[N]$	1	2	3	4	5	6	7	8	9	10	11	12	13
Sim. disp. $[mm]$	0.074	0.147	0.221	0.294	0.367	0.441	0.514	0.588	0.662	0.735	0.809	0.882	0.955
Ana. disp. $[mm]$	0.077	0.155	0.232	0.310	0.387	0.464	0.542	0.619	0.697	0.774	0.851	0.929	1.006
Relative error $[\%]$	5.3%	5.3%	5.3%	5.3%	5.3%	5.4%	5.4%	5.3%	5.3%	5.3%	5.3%	5.3%	5.3%

Table 4.1: Force deflection relation for the translating degree of freedom, both from the simulation and analytically derived equations.

Force $[N]$	1	2	3	4	5	6	7	8	9	10	11	12	13
Sim. rot. $[°]$	0.079	0.158	0.237	0.316	0.395	0.473	0.552	0.631	0.710	0.788	0.867	0.944	1.024
Ana. rot. $[°]$	0.087	0.174	0.261	0.349	0.436	0.523	0.610	0.697	0.784	0.871	0.959	1.046	1.133
Relative error $[\%]$	10%	10%	10%	10%	10%	10%	10%	10%	11%	11%	11%	11%	11%

Table 4.2: Force deflection relation for the rotational degree of freedom, both from the simulation and analytically derived equations.

the x-axis of the hinge (see Figure 4.1b for the axis orientation). Figure 4.19 shows the maximum displacement in Y caused by this out of plane actuation. At the maximum input force of $13\ [N]$ the displacement difference in Y between the extremities of the wafer is $21.1\ \mu m$. The distance between the two marked points is $11\ mm$. This equates to a rotation of $1.92\ mrad$. This is within the specification of $5\ \mathrm{mrad}$ set. The maximum, displacement in Y is just over the allowed $10\ \mu\mathrm{m}$ for the displacement of one slit edge. However, it is important to note that the needed range of motion will be lower than the maximum range of motion available. The maximum actuation force will not need to be used. So, the parasitic displacement found is acceptable for the typical operation.

All parasitic displacements due to actuation force can be found in Table 4.3. For the translation there is no out plane motion due to in plane actuation. Furthermore, the intended displacements are also marked with a dashed line.

	X disp. [μm]	Y disp. [μm]	Z disp. [μm]	X rot. [mrad]	Y rot. [mrad]	Z rot. [mrad]
Translation	–	3.83	1.3	–	–	0.25
Rotation	148.01	10.08	-96	0.11	–	1.92

Table 4.3: Overview of the parasitic displacements due to the actuation force.

4.6.2. Eigenfrequency analysis

As mentioned in Section 3.3, the mechanism should have a minimum eigenfrequency of at least $50\ Hz$ to stay well above the frequency peak of $50\ Hz$ found in the environment. For the analysis, the mechanism is constrained with a fixed constraint at the bottom. The snouts are attached to the mechanism, along with an added mass of $20\ \mathrm{g}$ at the end of the snouts to simulate the wafers attached with magnets. Figure 4.20 shows the first eigenfrequency along with corresponding mode shape and displacement magnitude. Important to note is the minimum eigenfrequency found, which is roughly $75\ Hz$. The mode shape also shows why it is crucial to have the eigenfrequency above this $50\ Hz$ peak. The eigenmode is precisely the motion that is used to open or close the slit. Exciting the mechanism at this frequency would thus yield a continuous change in the width of the slit. Table 4.4 gives the first six eigenmodes found. This Table shows that the dimensions found in the parameter optimization are adequate to deal with the frequencies occurring in the environment.

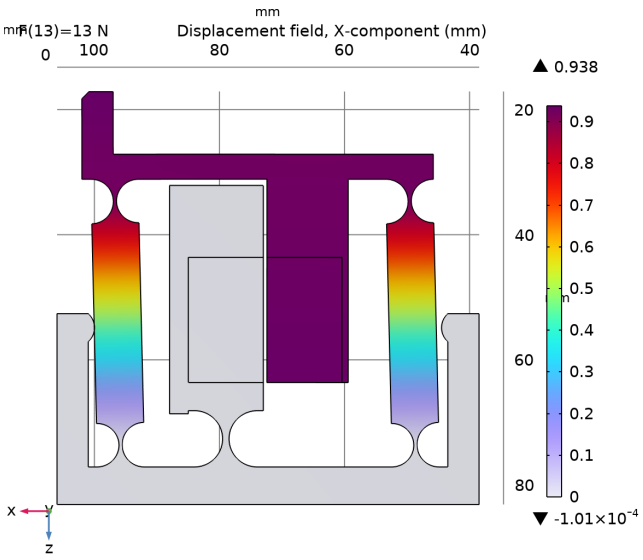

Figure 4.18: Translation verification of the mechanism.

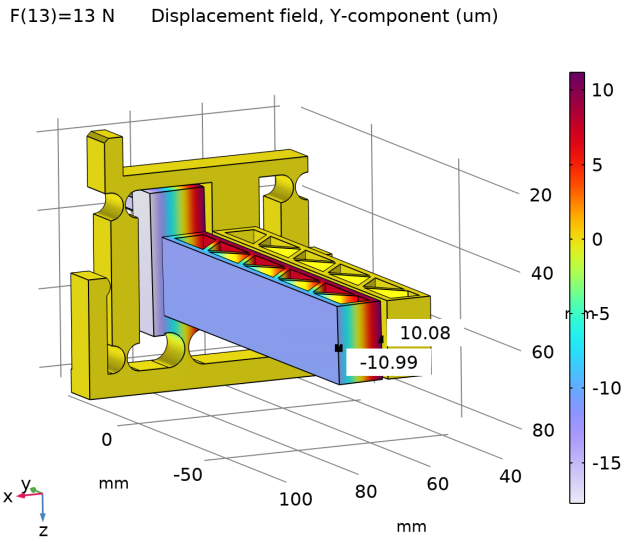

Figure 4.19: The parasitic displacements due to the out of plane actuation of the rotating half of the slit mechanism

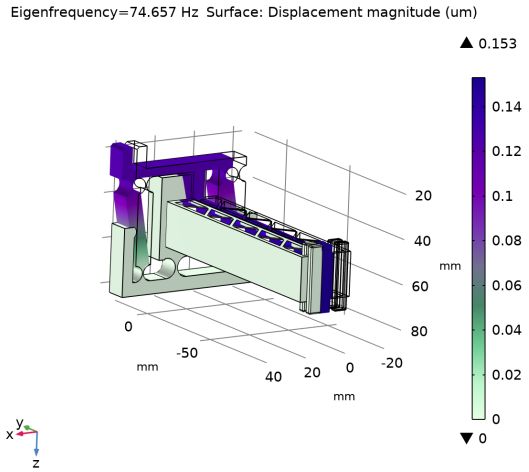

Figure 4.20: First eigenmode of the mechanism with snouts attached.

Mode number	**Eigenfrequency** $[Hz]$
1st	74.7
2nd	107.6
3rd	168.8
4th	258.2
5th	272.7
6th	302.7

Table 4.4: First six eigenfrequencies of the mechanism with snouts attached

4.6.3. Parasitic displacement due to gravity

Checking the parasitic displacements due to gravity is a simple task using COMSOL Multiphysics®. A static analysis is performed. The mechanism is again fixed at the bottom and gravity acts in the positive Z direction. Figure 4.22 shows the parasitic displacement magnitude for the mechanism. The exact values can be found in Table 4.5. All of these displacements lie well within the limits set in Section 3.3 or can be compensated using the actuators. Specifically, this is the case for the displacement in X. This is simply the movement that is used to make the slit wider or narrower. The displacements in Y and Z cannot be compensated, but are well within the limits set in Section 3.3. All rotations lie well within the tolerance budget too.

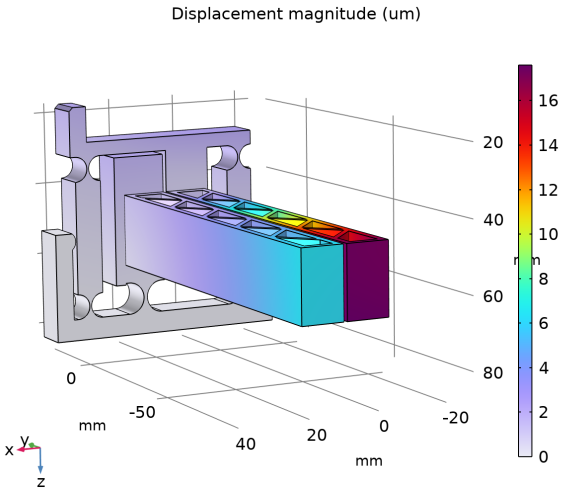

Figure 4.21: The total displacement due to gravity for the topology optimized domain.

	Translation half	**Rotation half**
X disp. $[\mu m]$	-1.6460	-0.21374
Y disp. $[\mu m]$	-1.6141	0.93248
Z disp. $[\mu m]$	-17.235	-6.1270
X rot. $[mrad]$	0.104	0.281
Y rot. $[mrad]$	0.00873	0.00651
Z rot. $[mrad]$	0.000421	0.0176

Table 4.5: Parasitic displacements due to gravity.

4.6.4. Stress analysis

The static analyses used to determine the quality of motion under actuation can also be used to determine whether the maximum stress constraints are adhered to. The stress is concentrated in the hinges. Close up images of the stress distribution in the hinges can be found in Figures 4.22a and 4.22b for the translation and rotation respectively. For translation, the maximum stress found is $269.3\ \mathrm{MPa}$. The maximum allowed stress from the optimization was set to $300\ \mathrm{MPa}$. So, the found stress is within the bounds set. For rotation, the maximum stress is $245.2\ \mathrm{MPa}$. The analysis is performed in 2D, in order to increase the mesh fidelity and improve analysis accuracy.

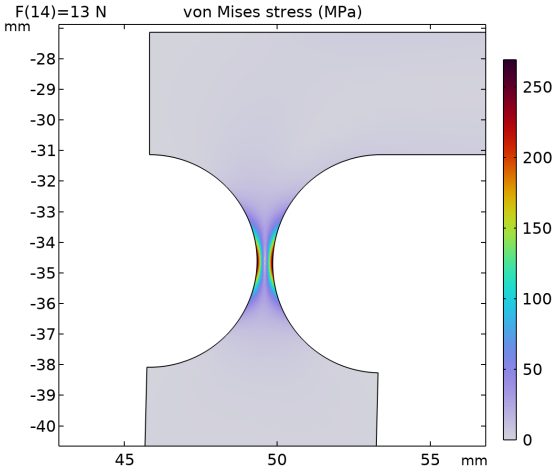

(a) Close up of the stress concentrations in one of the hinges for maximum translation actuation [MPa]. All hinges show the same stress distribution.

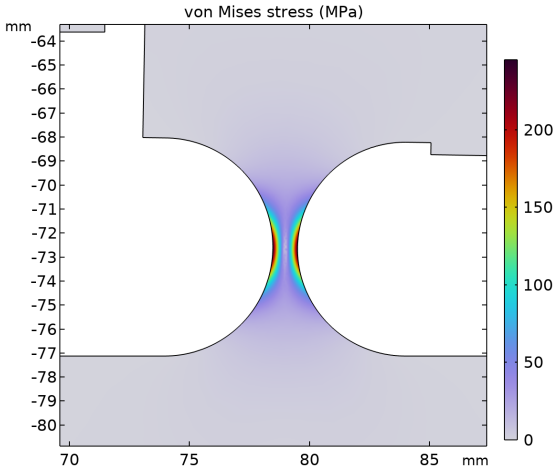

(b) Close up of the stress concentrations for maximum rotation actuation [MPa].

Figure 4.22: Analysis of the stress distribution for the two maximum actuation configurations.

5

Compliant mechanism topology optimization

In this Chapter, the topology optimization model used to build a compliant mechanism with required performance is discussed. First, the optimization domain is elaborated. The methods used to find a mechanism that fulfills the functions laid out in Chapter 3 are presented. Then, the complete optimization formulation is discussed and the final topology is shown. Finally, the performance of the optimized design is evaluated and the optimization scheme and results are discussed.

5.1. Topology optimization domain overview

To start, in order to increase the readability of this Chapter, the design domain will be discussed. The geometry, input and output ports, and regions of prescribed material and void will be presented.

Figure 5.1 shows the domain used for this optimization model. The domain geometry is taken to be the same size taken by the traditional mechanism as presented in the previous Chapter. The reason for this is that if the same domain is used, the optimized mechanism can in principle be placed into the system without any adaption. Of course, any domain could be usable. Using the same domain as used in the traditionally designed mechanism will also give a more direct comparison for the capabilities of topology optimization.

Looking at Figure 5.1, the domain is fixed at the bottom, indicated by the hashed block. The boundaries where forces are applied are indicated with the cyan lines. These are the inputs. The input at the top is used to actuate the left slit half, which is used for translation. The input inside the domain is used to actuate the rotation side, which is on the right.. The outputs are indicated with the yellow lines. These are used to measure the translations in X and Y. These are in almost the same positions as used for the traditionally designed mechanism, as will be discussed later. The pink dots are used to measure rotations, by taking the tangent of the difference in X displacement for each pair divided by their separation in Y. The thickness of the domain is set to $10\ \mathrm{mm}$, similar to the thickness of the traditionally designed mechanism.

The green shaded areas are prescribed material domains. The two regions near the center are the place where the snouts and wafers should be placed. The red shaded area in between the green region is a prescribed void region. This is the position of the slit. It is important to note that this region is kept wider than it should be in reality. This is done to help the optimizer. If this prescribed void region is kept at the $1.5\ \mathrm{mm}$ width used in reality, the optimizer will not be able to decouple the two halves. Decreasing the width of the gap after optimization is a very simple post processing step. The red shaded areas around the domain are also prescribed void domains.

It is important to note that the material stiffness used in this optimization problem is set to be 10 times lower than the stiffness of Aluminium. This is done to reduce computational costs. Although ideally the same material stiffness would be used, this would need significantly smaller mesh size than is realistically achievable with available hardware. This will be touched upon in section 5.6.

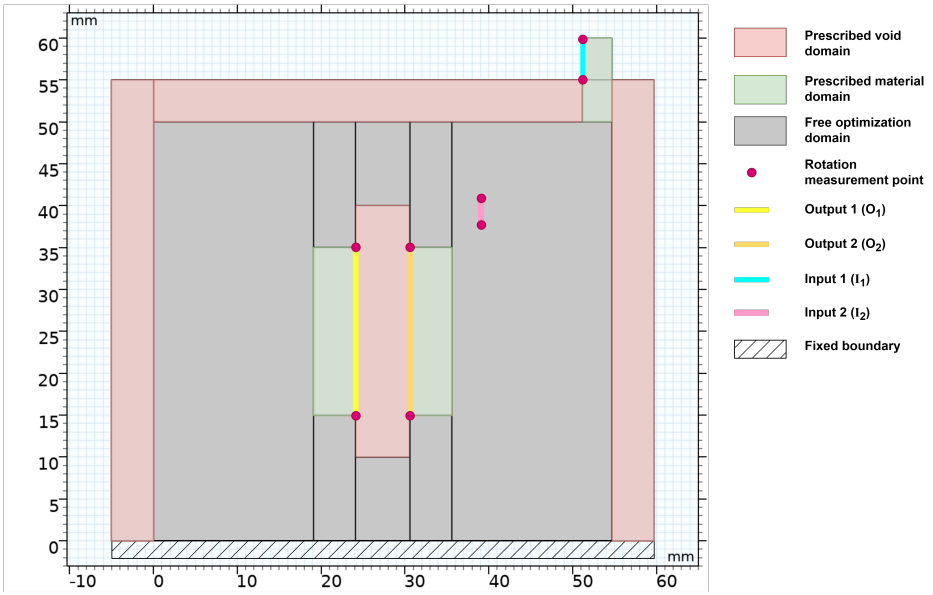

Figure 5.1: The topology optimization as setup in COMSOL Multiphysics®

5.2. Methods used for the design of the compliant mechanism

5.2.1. Compliance minimization using virtual springs

The basis of the optimization scheme is to optimize the compliance of the design domain Ω for a certain application (Liu and Korvink, 2009). By setting the right combination of the objective function and constraints, the design domain can be shaped to a desired mechanism.

There are multiple objective functions that can be used to do this. A very commonly used option is to use a weighted sum of the strain energy (SE) and mutual strain energy (MSE) of the design domain when subjected to one or more input forces F_i (Zhu et al., 2020). The SE is a structural function, whereas the MSE is a kinematic function. The MSE is used to maximize the amount of displacement or force exerted at the output. The SE is used to maximize the stiffness of the domain. By minimizing the SE the stiffness of the design domain is maximized, when subjected to an input force (Luo et al., 2005). In contrast, when maximizing the SE the stiffness is reduced.

Koppen et al., 2022 proposes an optimization scheme that uses prescribed displacements in combination with the maximization of only the strain energy of the different motion patterns, or degrees of freedom. For each *motion pattern*, or DoF, the SE is maximized or constrained. This method was tried for the design challenge of the slit mechanism, but was ultimately discarded as it was found to not be possible to integrate actuation points into this optimization scheme. A deeper view into this attempted optimization scheme can be found in Appendix I.

An important concept that can be used from Koppen et al., 2022 is to only use the SE to control the optimization scheme. Instead of using the MSE to set the flexibility of the output port, the strain energy can be used directly. How exactly this is done will be discussed in Section 5.2.1. Bypassing the MSE saves computational effort, as an extra load case is required to determine the MSE for each DoF.

So, the method used is the minimization of the strain energy subjected to several input forces, i.e. maximizing the stiffness of the domain. In order to create a mechanism that fulfills the requirements set in Chapter 3, several constraints are added to control stiffness of required degrees of freedom, parasitic motions, and input and output decoupling, which are discussed in coming Sections. As there are two degrees of freedom at two outputs that need individual control for the design challenge of this report, the FEM analysis is split into two load cases. One for each degree of freedom. The final objective function is to minimize the sum of their strain energies. The general optimization formulation is as follows.

$$\min: \quad J(\mathbf{x}) = SE_1 + SE_2 \tag{5.1}$$

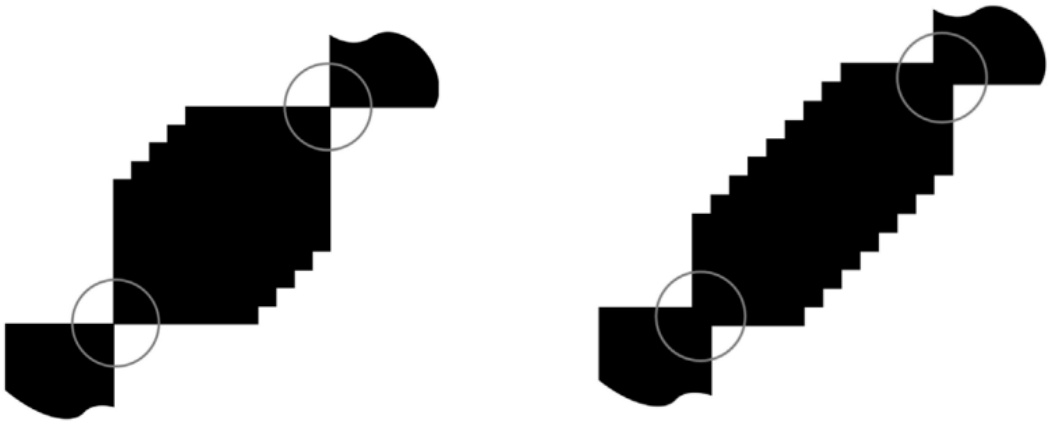

(a) One node connected hinges.

(b) De facto hinges.

Figure 5.2: Two images showing the point flexure problem that often arises from compliant mechanism topology optimization schemes, from Seltmann and Hasse, 2023.

The complete optimization model will be discussed in Section 5.3.

A critical part of the optimization scheme used is to implement virtual springs in the design domain. The springs are added at the input and output of the mechanism, as can be seen in Figure 5.3. These virtual springs are set to relatively high stiffness and are used to combat the problem of so called *de facto* hinges or one node hinges (Rahmatalla and Swan, 2005). These are regions where the deformation is concentrated, which results in high stress peaks. The reason for this is that the compliant mechanisms are optimized to have a low strain energy for degrees of constraints, whilst maximizing a displacement at the output through the mutual strain energy. The optimal topology for this are rigid links, which would have no strain energy, connected through revolute joints which can be used to generate large output displacements (Zhu et al., 2020). In a compliant mechanism this is approximated with the lumped designs as seen in Figures 5.2a and 5.2b. Because the virtual springs have a relatively high stiffness a high virtual force is also needed to find usable topologies. The result is that the output displacement found is not representative of the load case that will be used in reality. The displacement cannot be used to directly evaluate the stiffness of the domain. So, a method should be found to set the maximum allowed stiffness for the optimization problem.

Stiffness Control

To properly control the stiffness of the topology optimization, the strain energy of the design domain can also be used, as described by Koppen et al., 2022. There are four sources that can input or store energy in the optimization setup. The input force will perform work, W_{in}. The virtual springs at input and output will convert some of that work into potential energy, $U_{p,in}$ and $U_{p,out}$. The remaining energy will be stored in the strain that is caused by deformation of the domain, W_s. Figure 5.3 shows the location of the virtual springs. They only act in the X-axis. For the rotation half the springs are added at the points used to define the rotation. The total strain energy can be used to define the stiffness of the optimization domain. Assuming that all potential energy stored in the deformation of the domain is conserved, the domain can be compared to a spring. If the Equation for the potential energy stored in a spring is applied to the outputs of the domain, the apparent stiffness of the output points can be approximated by rewriting the Equation for the potential energy stored in a spring and substituting the potential energy by the strain energy of the domain:

$$W_{p,\ spring} = \frac{1}{2}\, k \cdot u^2 \tag{5.2}$$

Substitute $W_{p,\ spring}$ for W_s and solve for k:

$$k = \frac{2\ W_s}{u^2} \tag{5.3}$$

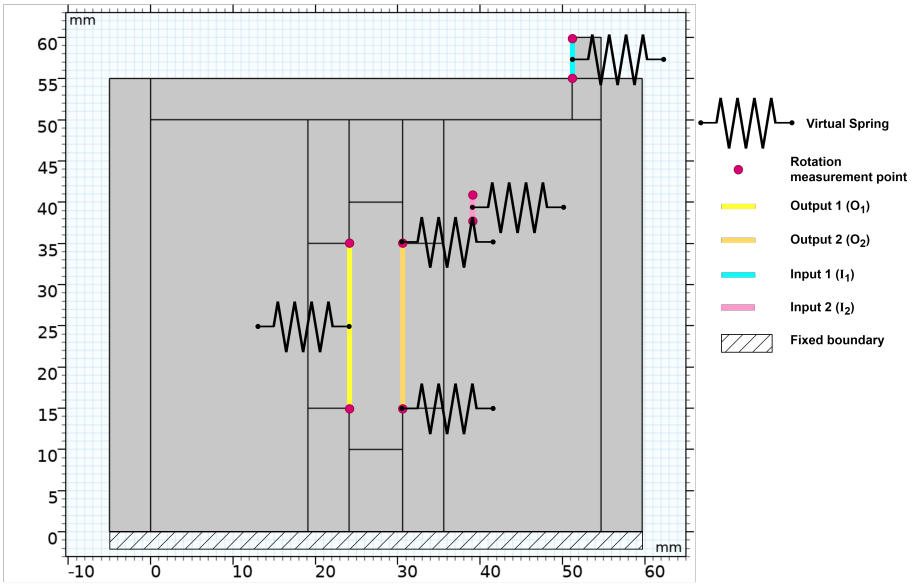

Figure 5.3: Schematic showcasing the virtual spring setup for the optimization domain. The input forces are collocated with the springs that are present at the inputs.

The total strain energy is available as a built in variable in COMSOL Multiphysics®. However, there is an issue with using the strain energy directly. The total strain energy for the domain is derived from an integration of the strain energy density over the domain. The strain energy density for linear elastic materials is derived from the double dot product of the stress and strain tensor in COMSOL for linear elastic materials, from the COMSOL Structural Mechanics User's Guide (COMSOL AB, 2025).

$$W_{s,el} = \frac{1}{2}\epsilon_{el} : (\sigma + \sigma_0) \tag{5.4}$$

It is based on the strain ϵ_{el} of each element and the stress σ plus the initial stress σ_0 in that element. The total strain energy is then found by taking the integral of the strain energy density over the full domain Ω. Although the void elements physically represent that there is no material, because the SIMP method requires the elements to maintain a finite density, there will be stress present in these elements. As the strain is determined solely by the deformation of the mesh elements, the strain energy for the void elements will not be zero. So, these void elements will still contribute to the total strain energy, increasing the apparent stiffness of the output. If the topology is then extracted and tested using a normal FEM analysis, the stiffness of the topology will be lower than that found in the topology optimized domain. This issue of strain energy in the void elements is amplified when disconnects appear in the material domain, where mesh elements are stretched further due to higher displacements. To remedy this, penalized strain will be used to calculate the stiffness. By applying the SIMP method to the strain energy of each element, the strain energy for the void elements will be penalized so that they do not contribute to the stiffness calculation. The total penalized strain energy density Equation is defined as follows:

$$W_{s,pen} = \int_{\Omega} Ws \cdot \bar{\tilde{\rho}}(\mathbf{x})^p dA \cdot d \tag{5.5}$$

Here, $\bar{\tilde{\rho}}(\mathbf{x})$ is the projected density of each element after filtering and d is the thickness of the domain Ω. This equation can be used to replace the strain energy in Equation 5.2.1 to find the penalized stiffness:

$$k = \frac{2\, W_{s,pen}}{u^2} \tag{5.6}$$

Elastic strain energy from the built in COMSOL variable [J]	Penalised strain energy [J]	Stiffness from strain energy from the built in COMSOL variable [N/mm]	Stiffness from penalised strain energy [N/mm]	Stiffness from verification study [N/mm]
0.449	0.320	9.913	7.126	7.024

Table 5.1: Stiffness comparison study. The optimized mechanism is extracted from the optimization domain to a mesh using threshold projection. This leads to a hard 1-0 boundary. The extracted domain is then analyzed using a structural FEA using a force-displacement analysis.

This equation can be used to set the maximum stiffness. In the form of an optimization constraint, it is as follows:

$$\frac{2\,W_{s,pen}}{u^2} \leq k_{req,i} \tag{5.7}$$

Where $k_{req,i}$ is the required maximum stiffness for DoF i.

Penalized stiffness validation

Figure 5.4 illustrates that the strain energy does not accurately represent how of the void elements contribute to the total strain energy. The load case for his optimization is shown in Figure 5.4a.

Comparing Figures 5.4a and 5.4b it becomes evident that some void elements have strain energy densities similar to the material elements. This leads to an overestimation of the stiffness of the optimization domain, since the void elements will also contribute to the total strain energy and therefore the apparent stiffness found through Equation 5.2.1. In reality, this would not be the case.

Table 5.1 compares the stiffness found when using the strain energy as a measure of the domain stiffness for the two cases analyzed along with the stiffness of the topology found from a validation study. The results show that the stiffness of the penalized SE more accurately approximates the stiffness of the optimized topology. A small difference remains, as the edges of the material domain are smooth gradients rather than a sharp $1-0$ boundary as would be the case with a physical mechanism. Even so, this approximation can still be deemed sufficiently accurate to predict the stiffness of the optimized topology.

An important point to note is that the penalized strain is only used for the constraints used to set the maximum apparent stiffness. The strain energy built in as a variable is still used in the objective function.

Motion generation

The mechanism must generate an output motion to set the width of the slit. As discussed, the output motion cannot be set directly using the output displacements, because the topology domain contains virtual springs and a virtual input force. Therefore, a different method is required.

This is achieved using the stiffness control constraints from Equation 5.2.1. The stiffness is defined by dividing the strain energy by the output displacements. By choosing the correct displacements, the required motion paths will automatically be determined.

For the translating half of the mechanism, the strain energy is divided by the output displacement in the X direction. To adhere to the upper limit set for the stiffness, the output displacement in X must achieve sufficient displacement. In this way, the optimizer generates a mechanism that produces the required translating motion through the penalized stiffness Equation.

The same principle holds for the rotation, where the stiffness is determined by the magnitude of the resulting rotation. By limiting the rotational stiffness, the optimizer is driven to produce the required rotational motion.

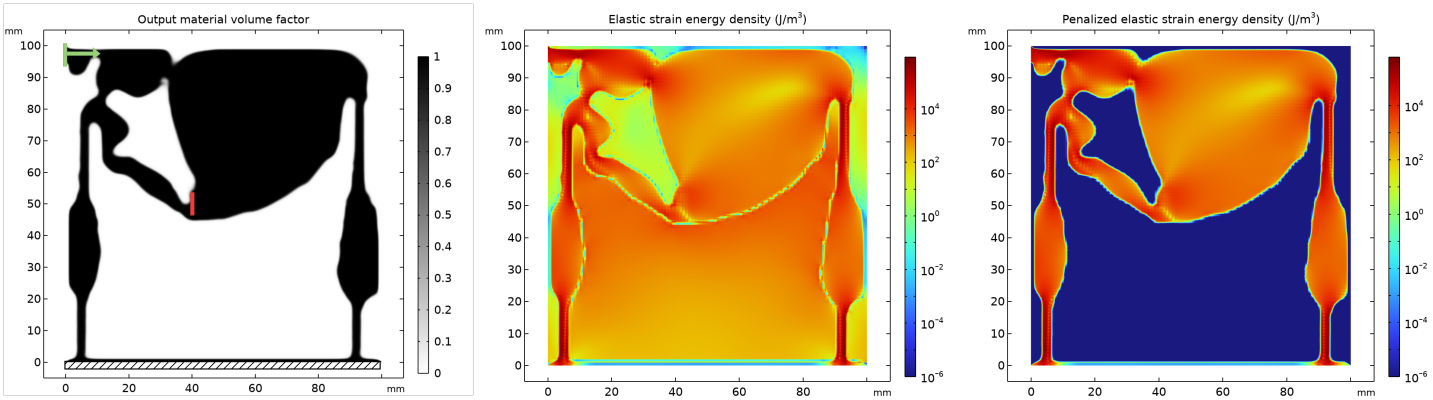

(a) Optimized topology **(b)** Strain energy density **(c)** Penalized strain energy density

Figure 5.4: Topology optimized domain for a translating mechanism. Figure 5.4a gives the optimized topology for the optimization formulation used. The red boundary shows the output point, where translation in X is measured. The green boundary gives the force input. At both boundaries, virtual springs are added. The domain is fixed at the bottom. Figure 5.4b gives the strain energy density of the domain. Figure 5.4c gives the penalized strain energy density of the domain. Note that the scales for these two Figures are logarithmic.

5.2.2. Parasitic motion suppression

As discussed in Section 3.3, there are stringent requirements on the allowed displacements of the wafers that form the slit mechanism. As the inputs for the optimization schemes are forces and not prescribed displacements, the output motions are not necessarily constrained to move in the desired direction. So, it is necessary to add constraints to limit these parasitic motions. Dirksen et al., 2012 presents a method to deal with these parasitic motions. They suggest a method to produce a path-following output motion using the output displacement vector $\mathbf{u}_{out}$ where constraints are set on the minimum and maximum output displacements u^{min} and u^{max} for each component of the displacement vector. As discussed in Section 5.2.1, the desired output motion will be determined using the stiffness constraints. So, there is no need to set any minimum output constraint. However, the maximum output constraint can be used to minimize parasitic motions. They propose the simple inequality constraint:

$$g(\mathbf{x}) = u_i - u^{max} \leq 0 \tag{5.8}$$

The same constraint can, of course, also be used to constrain allowed rotations. Then, instead of setting a maximum linear displacement, a maximum angular displacement should be set. To find the rotation of the outputs, the method described in Section 5.1 can be used. For the slit mechanism optimization, the parasitic displacements are allowed up to 0.1 mm for translations and 1 mrad for rotations.

5.2.3. Decoupling of degrees of freedom

As there are two degrees of freedom present, it is important to make sure that the two are decoupled. Although coupled DoFs can be controlled, it is much more complex than uncoupled DoFs. Especially as the chosen actuators are open-loop, so influence from parasitic displacements in the mechanism cannot be tracked directly. Zhu et al., 2018 proposes decoupling constraints for Multi-Input-Multi-Output mechanisms, for full output and input decoupling. Here, fully decoupled means that any input force F_{Ii} at input point Ii only results in one output u_{Oi} at output point Oi. Any parasitic displacements at a different output point Oj should be minimized.

The same holds for input coupling. Input force F_{Ii} should not cause any displacements at another input port Ij. The parasitic displacement at input Ij could cause the input port to be loaded by a parasitic force. This added force could exceed the maximum preload on the actuator, limiting or stopping the actuation.

For the output decoupling the constraint is as follows:

$$\eta_{j,i} = \left(\frac{\tilde{u}_{Oj,i}}{u_{Oi}} \right)^2 \leq \eta^* \tag{5.9}$$

$\tilde{u}_{Oj,i}$ is the displacement of output port j at point Oj, caused by input force F_{Ii} at input point Ii. Again, u_{Oi} is the displacement found at the intended output corresponding to input force F_{Ii}. The coupling is controlled using η^*. This factor determines the maximum allowed ratio between intended output displacement u_{Oi} and unintended output displacement $u_{Oj,i}$. For the optimization problem of the slit mechanism, it is set to 10^{-3}, as then a movement of $1\ \mathrm{um}$ will result in a displacement of only $1\ \mathrm{nm}$ at the other slit edge. Then, even though the two DoFs are technically coupled, they practically do not affect each other.

As mentioned, the inputs should also be decoupled. Zhu et al., 2018 proposes two similar constraints:

$$\xi_{j,i} = \left(\frac{\tilde{u}_{Ij,i}}{u_{Oi}}\right)^2 \leq \xi^* \tag{5.10}$$

$$\xi_{j,i} = \left(\frac{\tilde{u}_{Ij,i}}{u_{Ii}}\right)^2 \leq \xi^* \tag{5.11}$$

The same principles hold for these constraints as for the output decoupling. Here, the unintended displacement at input port Ij is denoted by $u_{Ij,i}$. In the optimization for the slit mechanism, six decoupling constraints are used. Two for the output decoupling and four for the input decoupling.

5.2.4. Robust optimization

A robust formulation of the topology optimization scheme is employed. The reason for this is two fold. Firstly, robust optimization schemes can be used to obtain topologies that are resilient to manufacturing errors (Sigmund, 2009). Secondly, the optimization scheme proposed by Sigmund, 2009 can be used simultaneously to impose minimum length scale control on the optimization domain, which can be used to combat the one node and de facto hinge problem highlighted earlier and ensure that the found topologies are in fact manufacturable.

Sigmund, 2009 proposes an optimization scheme were three cases are evaluated in each design iteration, originally intended for the design of MEMS devices where over and under etching is a common problem. However, for every manufacturing method the same uncertainty, removal of too much or too little material, is present to an extent. The smaller the features, the greater the relative effect of the uncertainty of the manufacturing. So, designs should be found that are robust to this issue.

For the optimization, a nominal case, an eroded case, and a dilated case are used. Sigmund, 2009 implemented the three cases by adjusting the threshold value θ_t for a smoothed Heaviside projection. The Heaviside projection raises all density value of each element above the chosen threshold to 1 and reduces all values below the threshold to 0 and is applied to the filtered density field. As the filtered density shows a gradient at each material-void boundary, changing the threshold value will move the exact location of the boundary in the final density domain. Lowering the threshold value will make the material domain larger and vice versa. For each optimization iteration step, the goal of the optimizer is to maximize the performance of the worst performing of the three cases.

$$\min : \max\left(\mathbf{f}(\bar{\tilde{\rho}}^e(\rho)), \mathbf{f}(\bar{\tilde{\rho}}^i(\rho)), \mathbf{f}(\bar{\tilde{\rho}}^d(\rho))\right) \tag{5.12}$$

With $\tilde{\rho}^d$, $\tilde{\rho}^i$ and $\tilde{\rho}^e$ denoting the density fields for the dilated, intermediate and eroded density fields. By maximizing the performance of the worst case scenario, in principle the final topology should be resilient to manufacturing errors. The three cases are defined with thresholds θ_t, 0.5, and $1 - \theta_t$. Generally speaking, a lower threshold value will result in more robust designs (Wang et al., 2011).

The projection is implemented in COMSOL Multiphysics® using a Hyperbolic tangent projection (HTP) instead of a smoothed Heaviside projection, as also proposed by Wang et al., 2011. Although they are numerically different, they achieve the same result and can be used in the same manner. The HTP can also be used for a secondary purpose. As mentioned earlier, the minimum length scale can be set using this robust optimization scheme, assuming that all three cases have the same topology. This can be used to remove one node and de facto hinges. The minimum length scale is determined by the density filter radius R and the threshold value θ_t (Wang et al., 2011). Wang et al., 2011 sets the relation for the minimum length scale with these two parameters using the relation found in Figure 5.5. Here b is the required length scale. Changing the values for R and θ_t can be used to set the required minimum

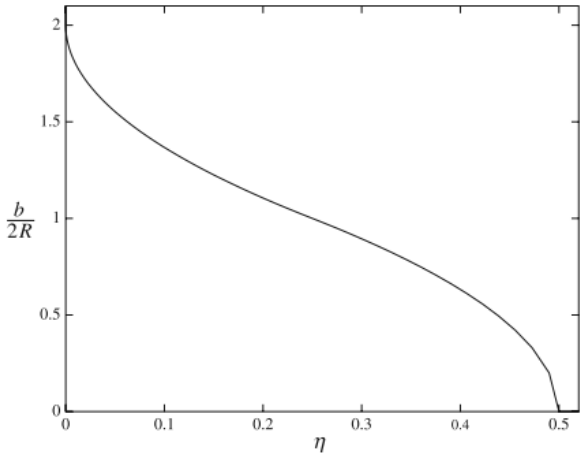

Figure 5.5: Relation used to determine parameters R and η for a wanted minimum length scale, from Wang et al., 2011. η is equal to θ_t.

length scale. Importantly, although two differing combinations of R and θ_t can give the same length scale, they do not necessarily result in the same topology. As mentioned earlier, lower thresholds result in more robust topologies.

For the slit mechanism optimization, the minimum length scale is set to 0.75 mm. This done by setting the filter radius to 0.33 mm, with the threshold value θ_t set to 0.4.

5.3. Complete optimization setup

Now that all the different optimization methods used for the design challenge at hand have been discussed, the final optimization formulation can be presented. To start, the mathematical problem formulation will be given. Then, the used optimization algorithm and sensitivity analysis are briefly discussed.

5.3.1. Optimization formulation

The optimization formulation is as follows, with all constraints set in negative-null form:

$$\min_{\boldsymbol{\rho}} : \max\left(f(\bar{\tilde{\rho}}^e(\boldsymbol{\rho})), f(\bar{\tilde{\rho}}^i(\boldsymbol{\rho})), f(\bar{\tilde{\rho}}^d(\boldsymbol{\rho}))\right) \tag{5.13}$$

$$\text{met}: \; f = (SE_1(\boldsymbol{\rho}) + SE_2(\boldsymbol{\rho})) \cdot V \cdot P \tag{5.14}$$

$$\text{s.t.} : \mathbf{K}(\bar{\tilde{\rho}}^e)\mathbf{u^e} = \mathbf{f} \tag{5.15}$$

$$: \mathbf{K}(\bar{\tilde{\rho}}^i)\mathbf{u^i} = \mathbf{f} \tag{5.16}$$

$$: \mathbf{K}(\bar{\tilde{\rho}}^d)\mathbf{u^d} = \mathbf{f} \tag{5.17}$$

$$: \frac{V}{V^*} - 1 \leq 0 \tag{5.18}$$

$$: \frac{2Ws_{pen}}{u_{O1,u}^2 \cdot k_{req,T}} - 1 \leq 0 \tag{5.19}$$

$$: \frac{2Ws_{pen}}{u_{O2,\theta}^2 \cdot k_{req,R}} - 1 \leq 0 \tag{5.20}$$

$$: \frac{(\tilde{u}_{Oi,j}/u_{Oj})^2}{\eta^*} - 1 \leq 0 \tag{5.21}$$

$$: \frac{(\tilde{u}_{Ii,j}/u_{Oj})^2}{\xi^*} - 1 \leq 0 \tag{5.22}$$

$$: \theta_{O1}/\theta^{max} - 1 \leq 0 \tag{5.23}$$

$$: v_{Oi}/v^{max} - 1 \leq 0 \tag{5.24}$$

$$: u_{O2}/u^{max} - 1 \leq 0 \tag{5.25}$$

$$: \theta_{Ii}/\theta^{max} - 1 \leq 0 \tag{5.26}$$

θ gives the rotation angle of inputs and outputs. u is displacement in X and v is displacement in Y. Additionally, as the load cases for the two degrees of freedom are handled in two different static structural FEAs, in reality there are two displacement fields u_1/v_1 and u_2/v_2. The rotation of each

element is also not an inherent variable that is accessible in COMSOL Multiphysics®. It is defined through the displacement fields u_i and v_i. The sole design variable is the density of each element $\rho_e \in [0, 1]$.

To further elaborate the model, all equations will be handled in order. To start, Equations 5.13 and 5.14 define the objective function to be minimized for this optimization problem. Equation 5.13 gives the robust formulation of the optimization problem, where the maximum value of the three cases is minimized. The three cases are calculated simultaneously. Equation 5.14 gives the actual objective function that is taken as the performance of the current iteration. Note the addition of V and P. These two scalar factors are added to reduce the presence of non-contributing material, as will be elaborated further in Section 5.6.3. Again, the compliant mechanism is divided into two cases, so for each iteration 6 FEA models are solved.

Equations 5.15 - 5.17 give the governing state equations that are used to solve the displacements for the optimization domain.

The standard volume constraint is handled using Equation 5.18. The maximum allowed volume is set to 0.4 of the total domain.

The stiffness is controlled using Equations **??** and **??**. These are the first non-standard constraints used in this topology optimization. It is important to note that for this optimization, to improve the convergence of the optimization, the allowed stiffnesses are relaxed. Specifically, $k_{req,T}$ (translation stiffness) is set to $30\ \mathrm{N/mm}$ and $k_{req,R}$ (rotation stiffness) is set to $40\ N \cdot m/rad$

The decoupling as described in Section 5.2.3 is governed by Equations **??** - **??**. Each degree of freedom needs both output and input decoupling, which requires three Equations. This results in a total of six Equations.

Finally, the parasitic motions are kept in check using the final eight constraints, Equations **??** - **??**.

5.3.2. Load case setup

As discussed in Section 5.2.1, virtual springs and loads are used to create a compliant mechanism. Specifically, the input forces F_{in} are set to $3000\ \mathrm{N}$. The virtual springs for the translating DoF are set to a stiffness of $200\ \mathrm{N/mm}$. The springs only act in the direction of the input force and output motion and have the same stiffness for both input and output. The springs used for the rotational DoF was set to $40\ \mathrm{N/mm}$. They are added to outer points of the slit edge, as shown in Figure 5.3. As will be discussed further in Section 5.6.5, the exact stiffness and input force used in the optimization has a large effect on the final topology. Unfortunately, finding the right combination is somewhat trial and error. The main criteria for the choice of stiffness and input force was reduction of disconnects in the dilated domain.

5.3.3. Numerical Implementation

Details regarding the numerical implementation of the given objective formulation will be discussed in this Section. Further supporting material regarding the numerical implementation can be found in Appendix G.

Mesh

For this optimization problem, the optimization domain was discretized using a 300×300 grid of square elements, resulting in a mesh size of $0.18\ \mathrm{mm}$. Given the minimum feature size of $0.75\ \mathrm{mm}$ (as given in Section 5.2.4), the smallest allowed features will be roughly 4 mesh elements wide. While a higher mesh density would improve the accuracy of the displacement calculations, the computational costs increase drastically with higher mesh fidelity. Furthermore, the goal of this research is not to find perfect correlation between the optimization domain and the finalized product. It is rather focused on finding a methodology. The given mesh size offers a balance between computational costs and accuracy.

Continuation scheme

To prevent the optimizer from converging to local minima prematurely, a continuation scheme is employed. The steepness of the projection slope β is doubled after each 150 iterations, starting at an initial value of $\beta = 2$ with a total of three increments. Similarly, the SIMP penalization factor p is increased from 3 to 4 after 300 iterations to further drive the optimizer to a discrete topology. In total, 600 iteration

steps are allowed. As discussed in the previous Section, each iteration step takes roughly 1 minute. So, the total optimization takes approximately 10 hours.

5.3.4. Sensitivity analysis

The sensitivities needed for this optimization are scheme are handled by COMSOL Multiphysics®, using the adjoint method as discussed in Section 2.2.2.

5.4. Final topology

The final topology found using the optimization scheme presented is shown in Figure 5.6. The design shown is the dilated design, as this was least susceptible to disconnects out of the three realizations. The optimizer was not able to find a design that adhered to all constraints given. This will be discussed further in Section 5.6.2. However, the dilated design gives a topology that is close to being in the feasible domain. Although it does not comply with all the performance requirements set in Section 3.3, as will be discussed later in Section 5.5, the functional requirements are met. The optimized domain could be used to provide an adjustable slit.

Because the actuators are placed in the same position as in the traditional design, the topology is similar. For both, the motion guidance of the translating half is given by two parallel links of equal length, connected by a rigid bar at the top. The major difference is the rotation side, which for the topology optimized version has its center of rotation in the middle of the slit, as can be seen in Figure 5.7b. Towards the top left of the design, there are pieces of material that do not seem to add functionality. This is discussed in Section 5.6.3. The mechanism in its displaced states can be seen in Figures 5.7a and 5.7b. Notable is the apparent absence of coupling between the two slit halves. Furthermore, there are no parasitic displacements at both inputs and both outputs. These two claims are further supported by the data in Table 5.2, which show the values for each constraint used. As the constraints are placed in negative null form, a negative value indicates the constraint is respected. It can be seen that for the dilated design, which is the design considered, only the two stiffness constraints and parasitic displacement at the translation input are violated (technically, the last decoupling constraint is not adhered to either, but the deviation is negligible). Possible reasons for this will be discussed in Section 5.6.2. For the rotating degree of freedom, although the constraint is violated, the stiffness is still low enough that it adheres to the performance requirements set as will be discussed in the following section.

Constraint	Value
Translation par. disp. Y	-9.54E-04
Rotation par. disp. X	-0.00379
Translation par. rotations	-0.00583
Rotation par. disp. X (2)	-0.0123
Par. disp. input 1 in Y	2.0283
Par. disp. input 2 in Y	-0.03413
Par. rotations input 1	-0.41583

Constraint	Value
Decoupling outputs 1	-0.45554
Decoupling outputs 2	-0.50758
Decoupling inputs 1	-0.40519
Decoupling inputs 2	6.39E-04
Translation stiffness	4.0839
Rotation stiffness	0.48924

Table 5.2: Overview of the constraint values for each used constraint, split for brevity.

Figure 5.6: The final topolgy found using the optimization problem presented.

(a) The final topology in its translated position.

(b) The final topology in its rotated position

Figure 5.7: overview of the topology optimized domain in its actuated positions. The black outline shows the undeformed state. Note that for both of these actuated positions are a scaled version of the movement, to better showcase the motion path.

5.5. Topology performance analysis

To analyze the mechanism, the topology was extracted to SolidWorks, where any non-contributing material was removed. Afterwards, the 2D optimized domain is extruded. Material is added for the rotating actuation point, to accommodate the same actuation mechanism as is used in the traditional design. Then, the optimized mechanism is imported back into COMSOL Multiphysics®and analyzed in the same manner as described in Chapter 4. Additionally, a validation of the stiffness constraints is performed.

5.5.1. Motion analysis

To determine the performance of the motion quality, two things are measured using COMSOL simulation. The parasitic displacements under maximum actuation force is measured and a force deflection analysis is made.

To validate the motion paths under actuation, a stationary force deflection analysis is used. Similar to the method described in Section 4.6.1, the mechanism is fixed at the bottom and actuated at the actuation points using an increasing force. For the analysis between the in plane displacements, a 2D simulations are sufficient. For the out of plane input for the rotation DoF, it is not.

Force [N]	1	2	3	4	5	6	7	8	9	10	11	12	13
Disp. [mm]	0.027	0.054	0.081	0.108	0.135	0.162	0.189	0.216	0.242	0.269	0.296	0.323	0.350

Table 5.3: Force deflection relation for the translating DoF.

Force [N]	1	2	3	4	5	6	7	8	9	10	11	12	13
Rot. angle [°]	0.03	0.06	0.09	0.11	0.14	0.17	0.20	0.23	0.26	0.28	0.31	0.34	0.37

Table 5.4: Force displacement relation for the rotating DoF.

Tables 5.3 and 5.4 show the force deflection relation for the two DoFs. Firstly, the translating DoF is too stiff, as mentioned earlier. For the translation the displacement at maximum input should be $1\ \mathrm{mm}$. The actual displacement is $0.35\ \mathrm{mm}$. This means the mechanism does not qualify for the requirements set in Section 3.3. For the rotation the displacement should be $0.15°$ per the performance requirements set, where it is actually $0.37°$. The force deflection curve shows a linear relation for both DoFs. However, the motion clearly shows parasitic displacements, as presented in Table 5.5 and Figure 5.8. The maximum parasitic displacement is $196\ \mu\mathrm{m}$ in Y, and $50\ \mu\mathrm{m}$ in Z. Even though the translation in Y is within spec, the translation in Z is not.

For the translating side, the displacement in Y is $8\ \mu m$ for the maximum input force, when normalized to $1\ \mathrm{mm}$ output displacement. This is far below the allowed per the performance requirements and equal to the performance of the traditional design. For the rotating side, the displacement of the center of rotation is $0.004\ \mathrm{mm}$ and 0.046 respectively for X and Y, which is well within the performance requirements. The center of rotation is also located in the center of the slit edge, where it is not for the traditional mechanism. So, there is no coupling between in plane rotation and displacement of the slit edge, which would result in easier control of the slit dimensions.

	X disp. [μm]	Y disp. [μm]	Z disp. [μm]	X rot. [mrad]	Y rot. [mrad]	Z rot. [mrad]
Translation	–	3.83	1.3	–	–	0.25
Rotation	279	196.5	52.1	1.406	1.604	–

Table 5.5: Overview of the parasitic displacements due to the actuation force.

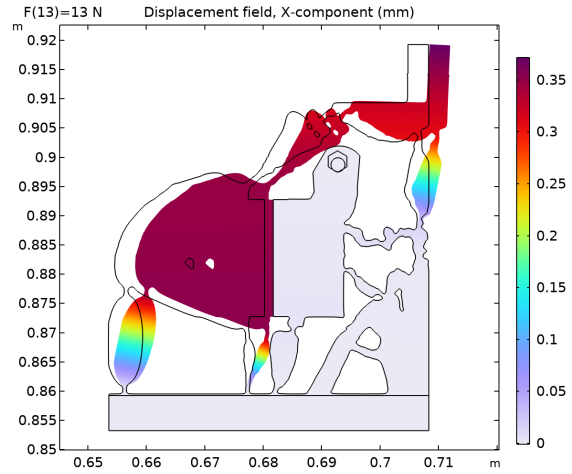

(a) Displacement due to actuation of the translating degree of freedom, scaled ten times to improve readability. The color bar shows the total displacement. The black wire frame shows the undeformed geometry. As the actuation is in plane 2D analysis is sufficient.

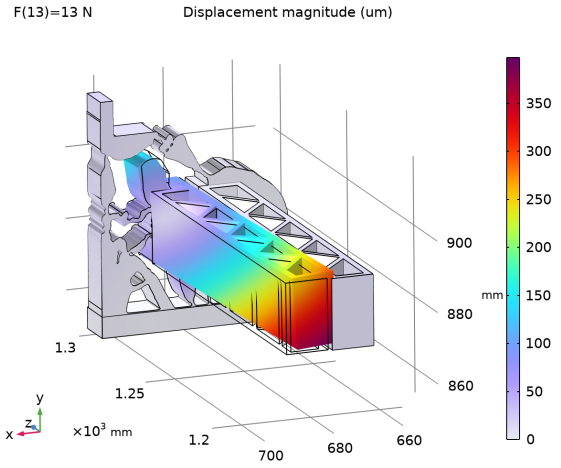

(b) Displacement due to actuation of the rotating degree of freedom, scaled ten times to improve readability. The color bar shows the total displacement. The black wire frame shows the undeformed geometry.

Figure 5.8: Figures showcasing the motion paths for the two DoFs under actuation input.

5.5.2. Eigenfrequency analysis

As stated in the performance requirements, the minimum eigenfrequency should be above $50\ \mathrm{Hz}$. The first six eigenfrequencies of the optimized mechanism can be found in Table 5.5.2. The first eigenfrequency is found at $107\ \mathrm{Hz}$, which is higher than that of the traditional design. The eigenmode of the first eigenfrequency is shown in Figure 5.5.2. In contrast to the traditional design, the first eigenmode is the vibration of the rotating half of the mechanism.

However, it should be noted that the total stiffness of the translation half is too high. This means that the eigenfrequency of the mechanism would be lower if the stiffness was as high as allowed by the constraints. How much lower the first eigenfrequency would be exactly is difficult to say. If the system is modeled as a simple mass-spring system, it can be approximated using $\omega = \sqrt{\frac{k}{m}}$. Assuming a stable moving mass, the eigenfrequency drops with the square root of the stiffness ratio. The stiffness found for the translating half is $37\ \mathrm{N/mm}$, where it should be $13\ \mathrm{N/mm}$. The eigenfrequency that corresponds to this motion path is $115\ \mathrm{Hz}$. The expected eigenfrequency would be about $68\ \mathrm{Hz}$. This is very similar to what is achieved using the parametric optimization for the traditional design. This would be logical using the equation presented, as the traditional design has a translation stiffness of $13\ \mathrm{N/mm}$, which should have roughly the same sprung mass as the optimized design.

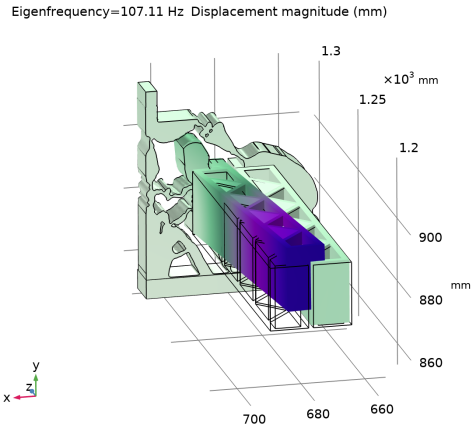

Figure 5.9: The eigenmode shape corresponding to the first eigenfrequency.

Mode number	**Eigenfrequency** $[Hz]$
1	107.11
2	115.38
3	144.52
4	213.78
5	286.16
6	551.62

Table 5.6: First six eigenfrequencies of the topology optimized mechanism.

5.5.3. Parasitic displacements due to gravity

The parasitic displacements induced by gravity are determined through a 3D stationary analysis. The total displacement magnitude and shape can be seen in figure 5.10. To properly analyze the performance of the optimized mechanism the displacement should be decomposed along the three axes. The maximum displacements and rotations can be found in Table 5.7, for both wafer planes that compose the slit. The results show that the displacement induced by gravity are within the bounds set by the performance requirements.

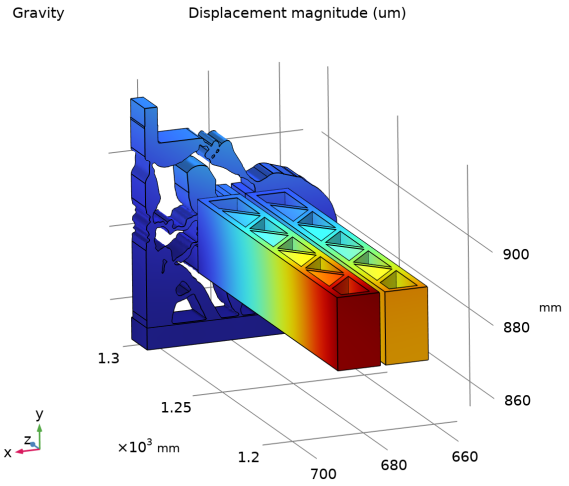

Figure 5.10: The total displacement due to gravity for the topology optimized domain.

	Translation half	Rotation half
X disp. $[\mu m]$	10.589	-0.12263
Y disp. $[\mu m]$	-24.108	-19.67
Z disp. $[\mu m]$	-3.0818	-2.7198
X rot. $[mrad]$	0.2348	0.1924
Y rot. $[mrad]$	-0.1002	-0.000768
Z rot. $[mrad]$	0.0115	-0.00248

Table 5.7: Parasitic displacements due to gravity.

5.6. Topology optimization discussion

Although the topological optimization offers a powerful tool in finding innovative designs, there are challenges present in the optimization scheme that limit the practical implementation of the raw optimization result. A discussion regarding these issues, and some mitigation strategies, can be found in this Section.

5.6.1. Out of plane actuation

Although the optimization was carried out in 2D, the rotational DoF is actuated out of plane. Although 2D validation studies show that the rotational DoF could perform better when implemented in plane, in reality because of the 3D actuation the performance is actually worse for this DoF. In the future this optimization would ideally be carried out using a 3D design space.

5.6.2. Constraint violations

Due to the large number of constraints present in this optimization problem, it cannot be guaranteed that all constraints are met during the optimization. This presents two problems. Firstly, it means that performance requirements set through the constraints are not necessarily met. Secondly, it might lead to optimizer not following the objective function well.

One potential method to deal with this is the constraint penalization factor. Increasing this factor places more emphasis on adhering to the constraints, whilst putting less emphasis on the objective. Altering this penalty function is an option that can be used to alleviate the issue of constraint compliance.

Another method is to relax the constraints. Although this of course means that the performance requirements are lowered, the influence of the objective value is increased. This could lead to better overall performance, at the cost of, for example, more parasitic displacements. However, none of these three solutions worked in practice.

The issue is exemplified by the use of the robust formulation. The optimizer seeks to adhere to all constraints for each of the optimization cases simultaneously. Although the general topologies of the three cases are the same, the thickness of all members in the topology differ, leading to disconnects

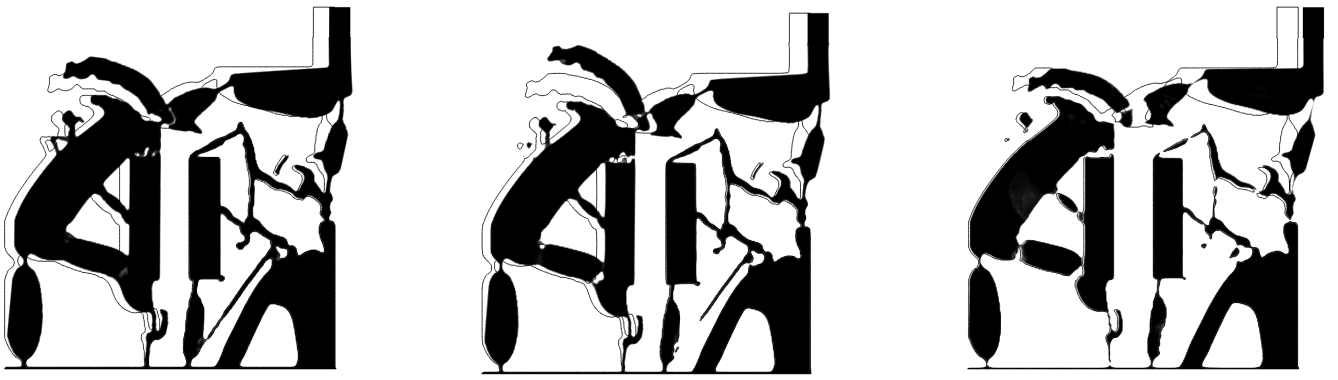

(a) Dilated design under translating actuation. **(b)** Intermediate design under translating actuation. **(c)** Eroded design under translating actuation.

Figure 5.11: The three designs used for the robust formulation when actuated for translation. The Figures demonstrate the issue discussed in Section 5.6.2.

in one or more optimization realizations (Figure 5.11). This can lead to very different displacement behavior for each optimization case and differing constraint values.

Since the apparent stiffness of the output is measured by its displacement under load, the optimizer thinks that the stiffness is very high as there is no output motion when the design is disconnected, whilst in reality it would be very low. This creates a conflict. Removing more material increases the disconnects in the domain and increases the perceived stiffness. Adding material increases the stiffness of already connected domains. This greatly reduces the theoretically viable design space. Reducing the minimum length scale and reducing the mesh size could be a remedy for this issue. However, for the attempted solution, this did not work. The computational cost also increased from roughly 10 hours to over 2 days. Further increases in fidelity are outside of the capabilities of available hardware.

5.6.3. Non-contributing material

Another issue that arises in this optimization problem is that of non-contributing material. As can be seen in Figure 5.12a, appendages are added to the stiff sections of the links. Plots of the the strain energy density show that the appendages lower the local strain energy density and consequently lower the total elastic strain (Figure 5.12c). However, in practice, this does not necessarily contribute to the design objective of increasing the mechanism stiffness. Although it does not negatively affect the practical stiffness, it does negatively affect the manufacturability of the domain. So, these material sections should be avoided. To achieve this, a combination of mass and perimeter bias is applied in the objective function.

First, to promote lower material usage, the average volume fraction V is added as a weight factor to the objective function. Lowering the average volume fraction then directly improves the objective function. The difficulty lies in the conflict between the SE and material fraction. The material will only be removed if the gain from reducing V is higher than the reduction in the SE.

To further bias the optimization, perimeter control is also introduced. Proposed by Haber et al., 1996, the density gradient $\delta\rho$ is used as an estimate of the perimeter $|\delta\Omega_s|$ of the solid material region. In the transition region from material to void, the gradient of the density field is high. By normalizing the gradient and summing the total normalized gradient over the design domain, the total perimeter can be transformed into a scalar quantity, P. As these appendages increase the perimeter of the material domain, this bias should lead to cleaner edges of the material domain and fewer of these appendages.

The perimeter found using the normalization of the gradient of the topology found can be seen in Figure 5.12b.

A final and simple addition can also be to lower the allowed volume fraction. This forces the optimizer to choose more critically where to place the material. However, this increases user input, which is not necessarily desired.

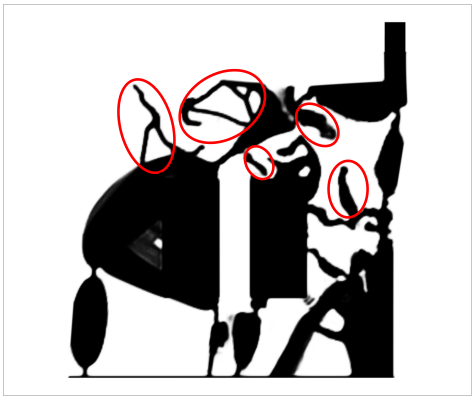

(a) An overview of the non-contributing material in the optimized topology. The non-contributing material is highlighted with red circles.

(b) The solid region perimeter $|\delta\Omega_s|$ found by normalizing the gradient of the density field of Ω.

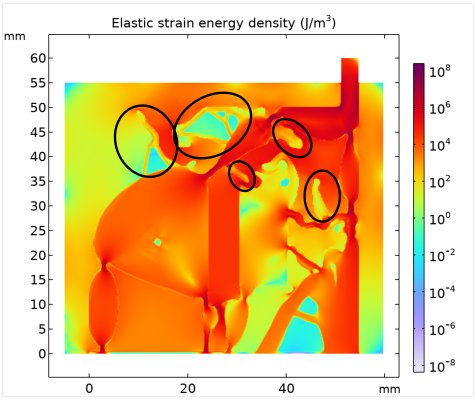

(c) The strain energy density of the final topology. The encircled areas indicate the non-contributing material. Note that the scale is logarithmic.

Figure 5.12: Overview of the non-contributing material, the normalized perimeter, and the strain energy density distribution.

5.6.4. Optimization termination

Ideally, a topology optimization is terminated when it reaches its optimality criterium. When using the GCMMA method, terminating based on the optimality criterium guarantees convergence to Karush-Khun-Tucker (KKT) conditions (Svanberg, 2002). When KKT conditions are met, it is guaranteed that constraints are adhered and that at least locally no improvement in the objective function can be found (Nocedal and Wright, 2006). However, due to the complexity of the slit optimization formulation, this is not achieved, as is often the case for structural optimization problems. So, instead, the optimization is terminated based on iteration count. Terminating before reaching KKT conditions could lead to an incompletely evolved topology, as it generally takes many iterations for the structure to develop properly (Bendsøe and Sigmund, 2004). This optimization was terminated after 600 iterations, as stated in Section 5.3.3. For the final hundred iterations of the optimization, the topology changes only slightly. Although, again, it cannot be guaranteed that this leads to the global optimum, this indicates the optimization at least comes close to a local optimum.

5.6.5. Effect of virtual spring stiffness

As previously touched upon in Section 5.2.1, virtual springs are added to the design domain to help reduce the amount of one node hinges in the final topology. The stiffness of these virtual springs has a significant effect on the final topology, as can be seen in Figure 5.13.

If they are set incorrectly, disconnects may even appear in the final topology. As the void regions still have finite stiffness, they can transfer loads. For certain combinations of virtual spring stiffness and virtual input force, it might be beneficial for the objective function to leave these areas where hinges would form as voids instead.

For relatively simple problems that have low computational costs (in order of minutes) an appropriate stiffness can be found through trial and error. For more computationally expensive optimizations, such as the final formulation presented in this Chapter, where the optimization run takes approximately 10 hours, this approach is impractical. As the influence of the virtual stiffness is so large, it is difficult to determine what the ideal virtual spring stiffness is for the final optimization domain.

(a) Optimized topology for a spring stiffness of $25\ [N/mm]$

(b) Optimized topology for a spring stiffness of $100\ [N/mm]$

(c) Optimized topology for a spring stiffness of $200\ [N/mm]$

Figure 5.13: Different realizations of a 1 DoF translation mechanism for increasing spring stiffnesses, with all other parameters kept equal. The input force is applied at the top left of the domain. The intended output is in the middle of the domain. Notice the disconnects in the middle of the domain in Figure 5.13c. Virtual springs are placed at the input and output, as described in Section 5.2.1.

6

Testing and results

This chapter describes the performance testing of the manufactured mechanism and discusses the results. It begins by briefly outlining the motivation for performing these tests. Then, the methodology and setup for the test is presented. The chapter is concluded by showing the testing results.

6.1. Test strategy

Simulations use ideal conditions, with perfect manufacturing tolerances and perfect assembly. Whether the simulated performance can be translated to a practical setup needs to be verified. The ultimate goal of these tests was to find out whether the mechanism can produce a slit with adequate dimensions. The required parallelism along with the average slit width was the main thing to verify. In addition to this, the actuation will be characterized. Typical step size will be analyzed, along with a repeatability study.

6.1.1. Experimental setup

For the experimental verification an optical test was performed. The purpose of this verification was to determine whether the mechanism is capable of achieving the slit dimensions required for the XRI test bed. In principle, all specified performance requirements should be addressed. However, this was not feasible within the available time frame and with the metrology resources available. Consequently, the tests are limited to the most critical performance requirements, namely the width of the slit and the parallelism between the slit halves. The following Section describes the experimental setup and measurement approach.

To validate the functioning of the mechanism was placed on an optical breadboard in an optical setup. The setup consists of four major components: a $405\ \mathrm{nm}$ laser light source, a beam expander used

to illuminate the whole slit at once, the mechanism itself with snouts attached mounted on a spacer and translation stage, and a camera placed behind the slit to measure the diffraction pattern. For the desired slit width, the diffraction angle is $54°$. So, using the snout, the slit is moved within the camera body to fit the diffraction patterns on the camera's sensor. A schematic diagram of the setup can be found in Figure 6.1.

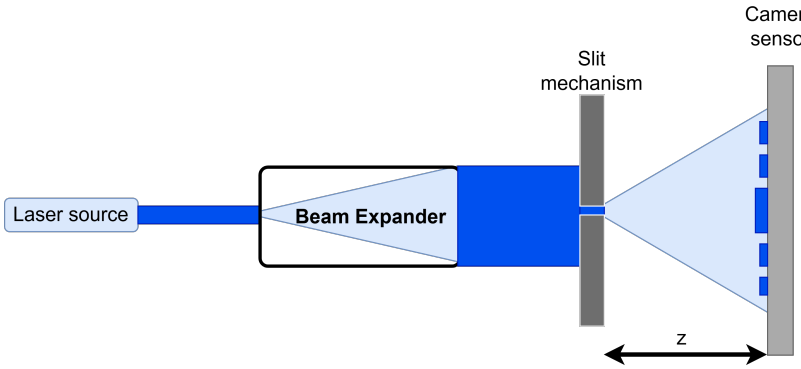

Figure 6.1: A schematic representation of the test setup. z is the distance between the slit and the sensor, and is critical to properly analyze the diffraction patterns measured.

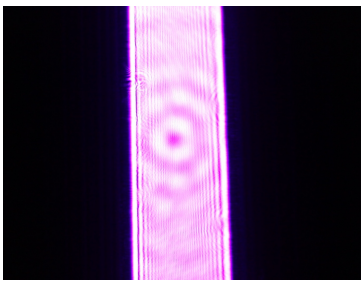

Figure 6.2: An image of the light used to illuminate the slit. The wafers are removed to align the mechanism and light source with each other. To improve readability, a small cutout of the full height of the wavefront is shown.

There are three critical alignments to make for this setup. Firstly, the laser should be aligned perpendicular to the slit. Secondly, the beam expander needs to be placed both parallel to and in line with the laser beam, to minimize distortions of the light. Thirdly, the light beam used to illuminate the slit needs to be centered on the slit. Finally, it is crucial that the distance from the slit to the sensor is known so that the only unknown variable is the dimension of the slit.

Figure 6.2 shows the wavefront produced by the laser and beam expander combination used to illuminate the slit. There are two noteworthy points about this wavefront that will be elaborated further in Chapter 7. Namely, the visible airy disk and the diffraction bands. Photos of the actual setup can be found in Figures 6.3a and 6.3b.

In order to reduce reflections in the setup, acktar black foil was added to cover the inside of the mechanism, the snouts, and the wafers. Unfortunately, the foil did not fully eliminate the reflections.

6.1.2. Test method

To determine the width of the slit, the diffraction patterns were captured and converted to positional data through the camera sensor pixel dimensions. A rough initial estimate was made using the Fraunhofer relation (Equation 2.2). This estimate can be used as a starting point for fitting of the data to a theoretical diffraction pattern. A 40-pixel thick horizontal slice was extracted from each image (a typical observed diffraction pattern was roughly $1000 - 1200$ pixels high), which was then averaged vertically to obtain a 1D intensity profile with an improved signal-to-noise ratio. By limiting the averaging height, it was ensured that slight tilt of the whole slit does not artificially broaden the intensity profile.

Wafer offsets along the optical axis ($h_z \approx 10\mu\text{m}$ for symmetric and $\approx 55\ \mu\text{m}$ for asymmetric mounting, see Section 4.1.3) introduce a predictable asymmetry in the observed Fraunhofer pattern. These can

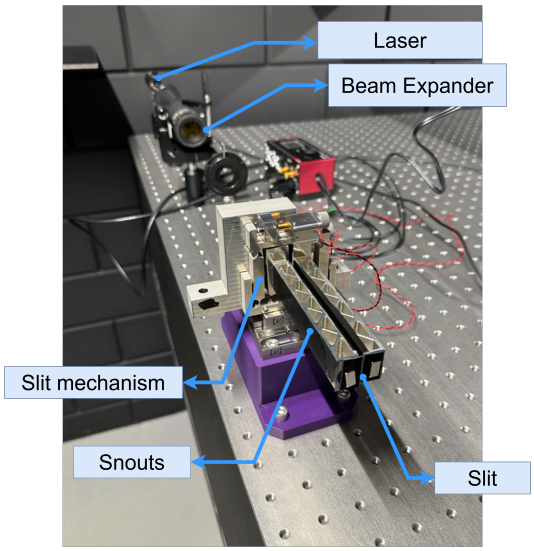

(a) Overview of the optical table with the testing setup. The camera would be installed at the end of the snout.

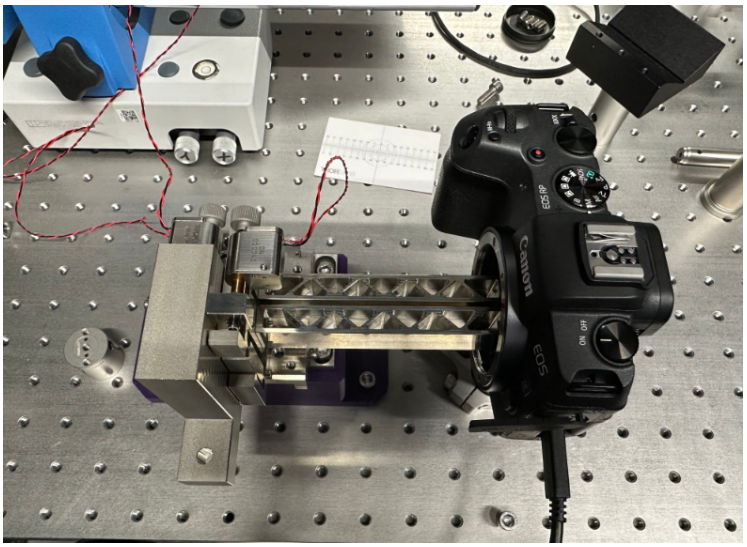

(b) Overview of the measurement setup with the camera in place. The snouts protrude into the camera body to bring the slit closer to the sensor.

Figure 6.3: Photos of the test setup used to verify the slit dimensions.

be accounted for by calculating an effective slit width a_{eff} following Vlieg et al., 1997:

$$I(\theta) = I_0 \left[\frac{\sin(\beta)}{\beta} \right]^2 \tag{6.1}$$

$$\text{with} : \beta = \frac{\pi \; a_{eff} \; \sin\theta}{\lambda} \tag{6.2}$$

$$: a_{eff} = a \; + \Delta x \; \cdot \frac{h_z}{z} \tag{6.3}$$

$$: \theta = \sin\left(\frac{\Delta x}{z}\right) \tag{6.4}$$

$$\tag{6.5}$$

In this equation a_{eff} is the effective width of the slit as a result of the offset between wafers as described by Vlieg et al., 1997, a is the actual width of the slit, h_z is the offset between wafers along the optical axis, Δx is the horizontal position on the camera sensor, and z is the distance from the slit to the camera sensor. Minor angular offsets of the incident laser light was neglected, following careful alignment (Appendix B for details on alignment).

Automated fitting proved unfeasible for the found intensity profiles, due to a plethora of measurement artifacts. These include: sensor noise, stray light, and internal reflections. So, the data was fit manually. Figure 2.5 shows the normalized intensity profile of a nominal Fraunhofer diffraction pattern, in addition to an image of the pattern. An example of a measured intensity profile, along with a fit, can be found in Figure 6.4b. By using the peak to peak distance most of the artifacts mentioned could be accounted for. While manual fitting introduces a degree of subjectivity, discrepancies remained discernible to $0.1\ \mu\text{m}$. Due to the stability of the laser source and as no temporal fluctuations are present in the diffraction pattern, using a single image per slit width was deemed sufficient for the characterization.

Verification of minimum slit width

The method for the primary test, the verification of the minimum slit width, is very simple. The slit will be closed in steps making sure that adequate parallelism is maintained. By monitoring the diffraction pattern it can be checked whether the slit gives adequate performance. To find the width of the slit, images of the diffraction pattern will be taken periodically. To eliminate the influence of the slit edge roughness, the horizontal slice used for the intensity profile is taken from the same pixel height for each

image. This corresponds to a constant position along the slit, meaning the same section of the wafers for each intensity profile. Then, the intensity profile is extracted and plotted against a theoretical fit to find the width of the slit.

Assessment of slit parallelism

The parallelism of the slit can be qualitatively verified using the diffraction bands that are seen on the camera. If there is a difference in angle between the wafers, the diffraction band will change in width along the slit length. To quantify the angle, equations (6.2), (6.3) and (6.5) can again be used. Only now are slices taken every 40 pixels over the length of the slit. Then, a linear fit is used to determine the slope of the width of the slit, which can be equated to the angular offset.

Actuation characterization

To characterize the actuation, the theoretical intensity plots will be manually fitted to the experimental data. The initial slit width is chosen based on two criteria. Firstly, that the camera can resolve the resulting Fraunhofer pattern. Secondly, that the movement of the slit causes a large enough change in the diffraction band width to be discernible. The mechanism will be translated using regular step intervals, after which a photo will be taken and the intensity distribution will be analyzed. Intervals of 50 steps will be used. As the nominal step size of the actuators is $10 - 30$ nm, this should result in $0.5 - 1.5\mu$m step in translation. The test will be repeated for 10 step increments. Like the verification of minimum slit width test, the horizontal slice is taken at the same vertical position, to eliminate the effect of slit roughness.

6.2. Testing results

6.2.1. Minimal slit dimension test

To verify the performance of the slit at its lower limits, the slit width was incrementally reduced as previously mentioned. Figures 6.4a and 6.4b show the image of the diffraction pattern and the mean intensity plot of a 5.8 μm slit width. Qualitatively, several observations can be made. To start, horizontal fringes are present in the central band seen in Figure 6.4a. Furthermore, the diffraction bands show irregular, serrated edges rather than smooth transitions. These two phenomena are visible in all images presented in this Section, suggesting they are a systematic feature in the setup.

A third phenomenon, observed for most images presented in this Section, is that the left side of the diffraction pattern is obscured by reflections. Although the measured intensity profile can still be fitted to the theoretical model, the reflections introduce additional uncertainty.

Furthermore, the slit displays a slight angular misalignment. This is accounted for by the fact that the intensity is averaged over only a thin horizontal slice. Although this will slightly reduce the spacing between maxima, the low height of the slice renders the effect negligible. Finally, the width of the central band tapers towards the bottom of the slit. This is the effect of physical damage to the wafer edge. A small chip out of the corner of the slit increases the width of the slit at this point, which results in a narrowed diffraction pattern. This effect can be used to find the center of the slit, which helps improve the accuracy of the manual fitting. The left side of the diffraction pattern is obscured by internal reflections.The right side clearly shows the secondary diffraction bands. Figure 6.4b shows the theoretical fit to the measured intensity plot. It can be seen that the central and higher order maxima align well. As the camera sensor is overexposed, the central band does not show the typical central peak. The theoretical intensity plot is shifted upward to match the experimental data.

Figures 6.5a and 6.5b show the diffraction pattern for a slit with a width of 4 μm. This is the threshold where the central diffraction band is still clearly visible but where reflections obscure the second minima on the left side. The diffraction pattern is still clearly recognizable and can be fitted to a theoretical intensity plot well. Figure 6.5b shows the theoretical fit to the mean intensity plot. Like the previous set of images, the intensity pattern is shifted upwards as the central band is overexposed. Here, the central and second maxima fit well to the theoretical intensity plot. However, the higher order maxima no longer align well in their position along the X-axis. The intensity still aligns well. Furthermore, the first minimum can not be seen on the left side of the diffraction band due to the reflections falling on the camera sensor.

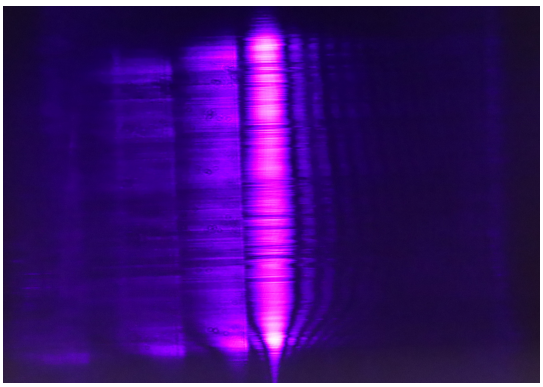

(a) Image of the diffraction pattern.

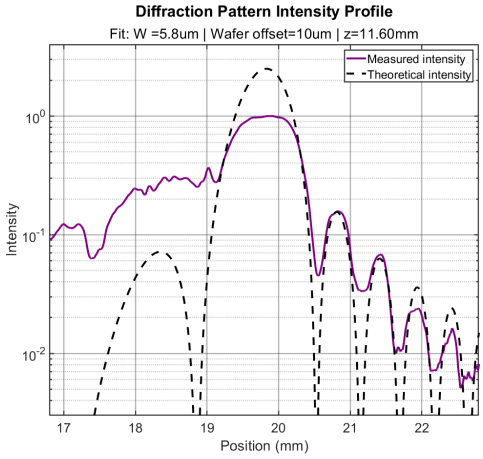

(b) Intensity plot taken from the mean of a 40 pixel high slice out of Figure 6.4a, including a theoretical fit for $5.8\ \mu\mathrm{m}$ that was shifted upwards. This data was found using the red channel from the color data of the image.

Figure 6.4: Fraunhofer diffraction pattern and intensity plot corresponding to a $5.8\ \mu m$ wide slit.

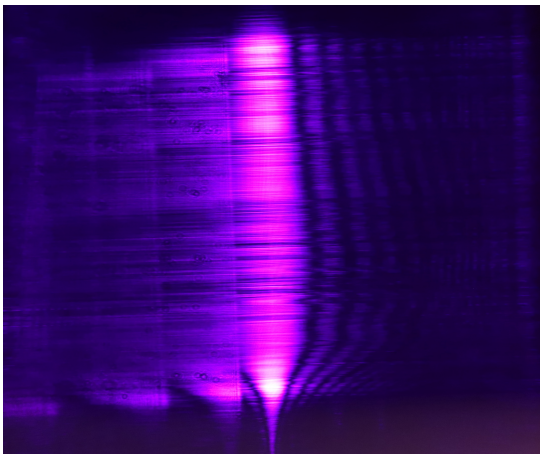

(a) Image of the diffraction pattern.

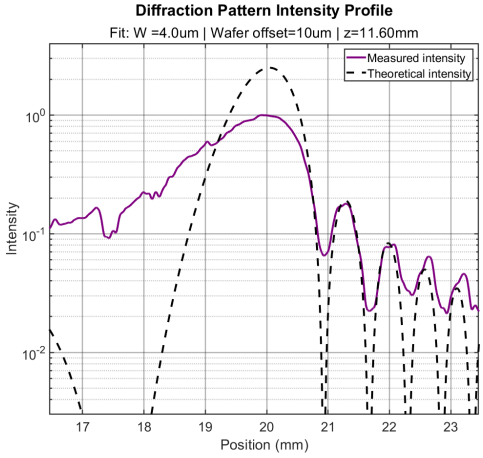

(b) Intensity plot taken from the mean of a 40 pixel high slice out of Figure 6.5a, including a theoretical fit for $4\ \mu\mathrm{m}$ that was shifted upwards. This data was found using the red channel from the color data of the image.

Figure 6.5: Fraunhofer diffraction pattern and intensity plot corresponding to a $4\ \mu m$ wide slit.

Figures 6.6a and 6.6b show the diffraction pattern and intensity plot for slit width of $3.2\ \mu\mathrm{m}$. This is the threshold where the Fraunhofer patterns starts collapsing. The diffraction bands on the right hand side are still visible, as is the central maximum. However, if the slit is closed further, the center of the intensity plots disappears.

Figure 6.7a shows a diffraction pattern where the central band has disappeared. The typical Fraunhofer diffraction pattern is no longer identifiable. The pattern shows a significant loss of symmetry. Although diffraction bands are still visible on the right hand side, the central band and diffraction bands on the left have dissipated. This is the effect that arises due to a small offset along the optical axis between the two wafers (Vlieg et al., 1997), as described in Section 6.1.2. The influence of this effect increases as the slit narrows. A theoretical fit that takes this effect into account can be seen in Figure 6.7b. The manual fit indicates that the slit width is $1.8\ \mu\mathrm{m}$ wide, for a 10 micron offset between wafers. However, the absence of any diffraction bands on the left side of the central band should be noted, where they

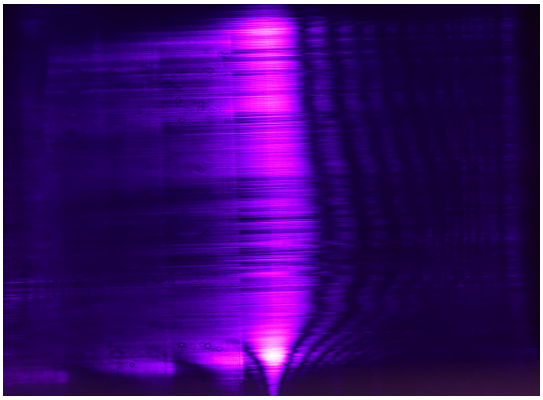

(a) Image of the diffraction pattern.

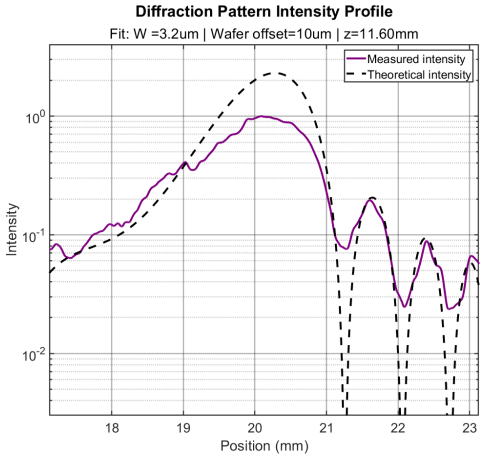

(b) Intensity plot taken from the mean of a 40 pixel high slice out of Figure 6.6a, including a theoretical fit for $3.2\ \mu\mathrm{m}$ that was shifted upwards. This data was found using the blue channel from the color data of the image.

Figure 6.6: Fraunhofer diffraction pattern and intensity plot corresponding to a $3.2\ \mu m$ wide slit.

are still expected from the theoretical intensity profile. Furthermore, the normalized intensity of the plot also does not align well.

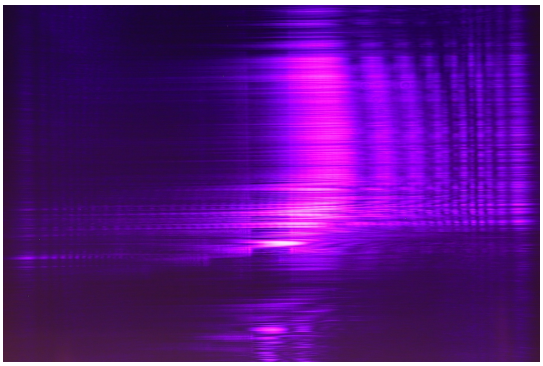

(a) Image of a Fraunhofer diffraction pattern where the expected diffraction pattern is no longer clearly visible. The image shows significant asymmetry, and a loss of intensity where the central band is expected to be due to the offset between wafers.

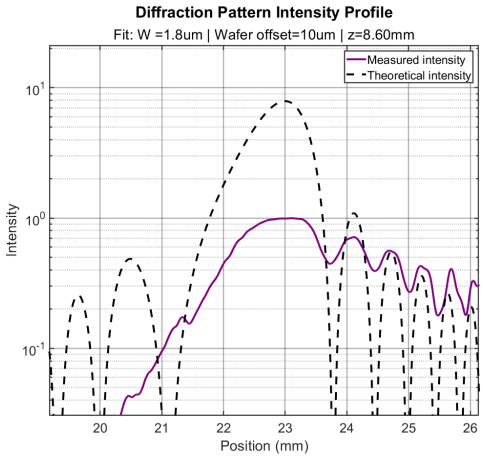

(b) Intensity plot taken from the mean of a 40 pixel high slice out of Figure 6.7a, including a theoretical fit for $1.8\ \mu\mathrm{m}$ with an offset of 10 micron between slit edges. This data was found using the red channel from the color data of the image.

Figure 6.7: Fraunhofer diffraction pattern and intensity plot corresponding to a $1.8\ \mu\mathrm{m}$ wide slit.

6.2.2. Assessment of slit parallelism

To verify angular control of the mechanism, the two slit edges were mounted askew. The rotational DoF was then incrementally actuated to achieve the required parallelism. As there is no live readout of the width of the diffraction pattern, the parallelism was visually assessed by monitoring the width of the central maximum for every actuation step. The higher order diffraction bands proved a particularly secondary aid, as they show exaggerated angles for low slit widths. Figure 6.8a displays the diffraction pattern used to determine how well the slits can be aligned. The diffraction pattern visually indicates that the slit edges are parallel. This can be especially seen from the secondary bands.

To quantitatively analyze the angular alignment of the slit, the width was analyzed for every 40 pixels

along its entire length. The intensity plots used can be found in Appendix C. A linear regression was applied to the data to find the angular alignment, to account for the slit roughness. Two fits were performed: One with all data points included and one where the apparent outliers at the extremities of the slit are excluded. Figure 6.8b presents the scatter plot including the two linear regressions, with outliers marked in magenta. The slopes associated with these two linear fits are $-0.5025\ \mu\mathrm{m/mm}$ and $0.0201\ \mu\mathrm{m/mm}$ respectively. For the comprehensive fit this equates to an angle of $0.5025\ \mathrm{mrad}$ ($103\ \mathrm{arcsec}$), with an R^2 value of 0.4, indicating only slight correlation. When outliers are excluded, the slope equates to an angular alignment of $0.0201\ \mathrm{mrad}$ ($4.15\ \mathrm{arcsec}$), with an R^2 value of 0.004 indicating no linear relationship.

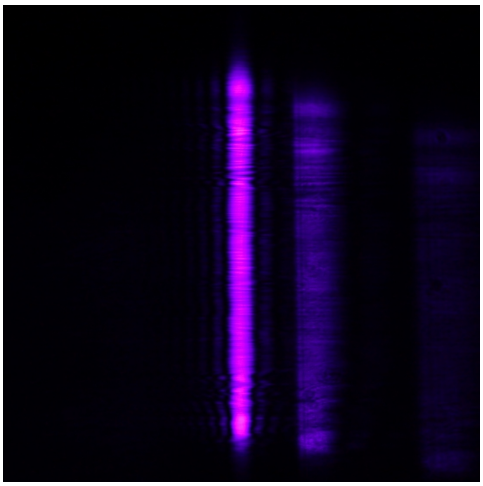

(a) The diffraction pattern used to characterize the parallelism achievable with the mechanism, corresponding to a slit width of roughly $20\ \mu\mathrm{m}$. The faint wide band on the right of the image is a reflection artifact.

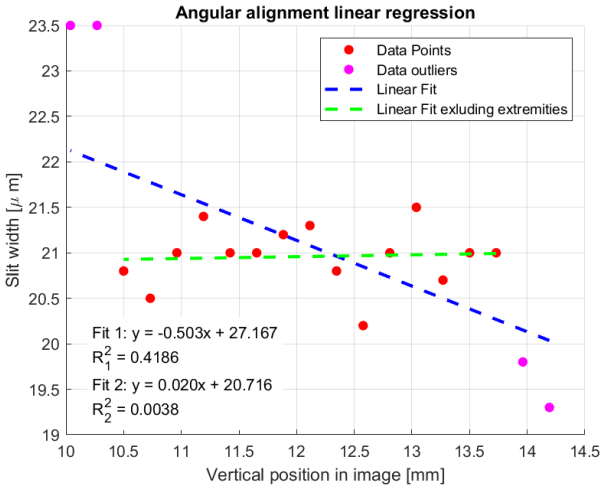

(b) Scatter plot showing the width of the slit for every 40 pixels along the slit length. Two linear fits are added, one for all data points, and one that excludes the apparent outliers at the extremities of the slit.

Figure 6.8: Image of the Fraunhofer pattern used to determine the achievable parallelism, along with the scatter plot including linear regressions.

6.2.3. Actuation characterization

To characterize the actuation performance, the mechanism was incrementally closed at regular intervals whilst measuring the relative displacement for each step. Scatter plots including linear regression fits will be presented this Section, with the intensity profiles used for analysis available in Appendix C.

The first actuation characterization test was performed for 50 step increments. The average step size for the used actuators is $10 - 30\ \mathrm{nm}$ depending on operating conditions. So increments of $0.5 - 1.5\ \mu\mathrm{m}$ are expected. Figure 6.9 shows the scatter plot from this, including the linear fit. The found slope suggest that the actual increments are $1.363\ \mu\mathrm{m}$, with an R^2 value of 0.9986, indicating good fit quality. This means that the average step size of the actuators for the 50 increment steps is $27.26\ \mathrm{nm}$, which is within the expected range.

To take this a step further, Figure 6.10 shows a scatter plot for 11 increments of 10 actuation steps, which should correspond to a displacement of $0.1 - 0.3\ \mu\mathrm{m}$ each. A linear fit indicates that the average displacement for each increment in reality is $0.22\ \mu\mathrm{m}$, with an R^2 value of 0.994, indicating very high fit quality. This equates to a step size resolution of $22\ \mathrm{nm}$ per step, which is comparable to the 50 step increment test.

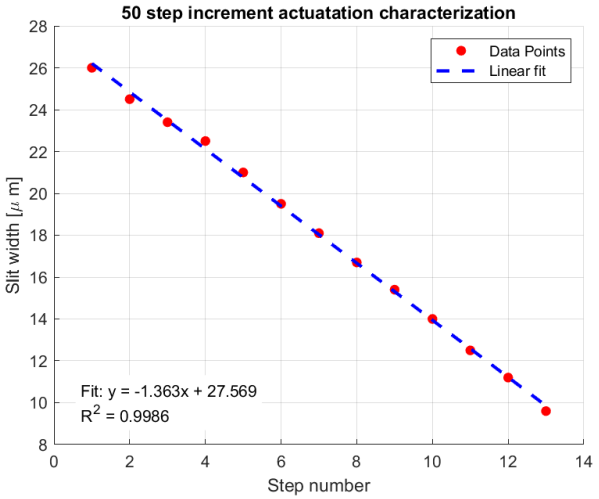

Figure 6.9: Scatter plot including a linear fit for the 50 step increment characterization test.

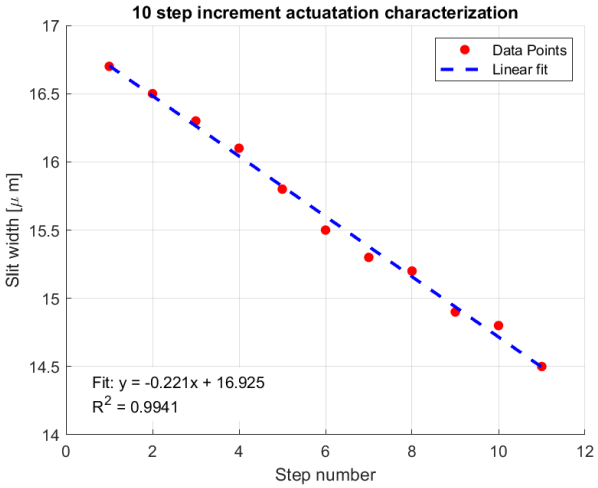

Figure 6.10: Scatter plot including a linear fit for the 10 step increment characterization test.

7

Discussion and Future work

7.1. Discussion

Since the TO results were analyzed and discussed in Chapter 5, this Chapter focuses on discussion points regarding the traditional design and testing results. First, discussion surrounding the design synthesis will be handled. Then the results from chapter 6 will be discussed.

7.1.1. Mechanism synthesis discussion

Lack of full design space study

The design phase was started using a baseline mechanism on which to build. The reason for this was that this would leave time to develop the TO model. It can be questioned whether this was the right way to structure this research. By exploring the full design space, better alternative designs could have been found. Of course, it should be noted that the mechanism as is designed is adequate for the performance requirements.

Parametric optimization

As mentioned, the parametric optimization was performed using Matlab. Realistically, the parametric optimization should have been performed using COMSOL Multiphysics®. Then, the eigenfrequency could have been implemented directly as a constraint, instead of using the maximization of hinge stiffness as a proxy. Furthermore, the constraints on the parasitic displacements could have been added directly as constraints too. This could have resulted in even higher performance of the mechanism.

Furthermore, instead of choosing the parameters for rotating DoF manually, a parametric optimization using COMSOL Multiphysics®should have been performed too.

7.1.2. Discussion of achieved results

Manual fitting of the the theoretical Fraunhofer patterns

As discussed in Section 6.2, a manual fitting of the Fraunhofer patterns to the found intensity distributions was adopted. Although this is a valid method for determining the slit width, it introduces a degree of subjectivity compared to automatic curve-fitting tools. Automatic curve fits were attempted, but could not accurately converge on the found intensity profiles. Consequently, the determination of confidence intervals would rely on qualitative assessment rather than statistical computation. In other words, they would be inherently arbitrary. For this reason, it was chosen to omit them, acknowledging that the accuracy of the fits is subject to the authors estimation. Nevertheless, discrepancies in the results remained clearly discernible down to a level of$0.1\ \mu\mathrm{m}$ for all manual performed. Still, the absence of automated verification is a limitation in the statistical rigor of the results.

Minimum slit width

The results shown in Chapter 6 indicate that the mechanism can potentially achieve the $0.5\ \mu\mathrm{m}$ slit width. However, it was not possible to reproduce this result directly using the Fraunhofer pattern. The normal diffraction pattern breaks down around a slit width of $3\ \mu\mathrm{m}$. This can be explained by the offset between wafers. The theoretical pattern for a 0.5 micron slit for various axial offsets can be found in Appendix C, which showcases what type of intensity profile is expected. A manual fit indicates that a slit width of $1.8\ \mu\mathrm{m}$ was possibly achieved. However, as the center of slit disappears an extra variable is introduced in the manual fitting process, increasing uncertainty around the results.

Slit parallelism

The value of $R^2 = 0.0038$ for the parallelism test excluding outliers indicates that the variation in slit width is dominated by experimental noise. In this case, it is likely the roughness of the slit edges. When including the outliers, the value for R^2 is 0.4186, suggesting relatively low correlation between the fit and measured data. Their exclusion can be justified by two factors. Firstly, the abrupt change between the outliers and the rest of the dataset does not align with a consistent angular offset. Furthermore, the laser beam diameter was reduced by an iris. The positions of the outliers coincides with the edge of the reduced beam. The sudden jump between subsequent measurements could be an effect from the iris on the light.

When the outliers are excluded from the data, it can be concluded from R^2 that no systematic change in width can be discerned. The considered length of the slit is $3.2\ \mathrm{mm}$ long. Taking into account that a difference in $0.1\ \mu\mathrm{m}$ is discernible by visual assessment of the diffraction pattern, this suggest that the angular offset is below $0.1\ \mu\mathrm{m}$ over the measured slit length. This equates to $0.03125\ \mathrm{mrad}$, or 6.45 arcsec, which is within performance requirements set.

Actuation characterization

The actuation characterization tests performed in Section 6.2.3 demonstrate largely consistent step size. The linear regression fit for the actuation characterization indicates an average step size of $0.22\ \mu\mathrm{m}$ per 10 step increment. This equates to an actuation resolution of $22\ \mathrm{nm}$. The 50 step increments show a slightly higher average step size of $27\ \mathrm{nm}$. The discrepancy in the individual step size may be attributed to the higher maximum stepping speed for the 50 increment test. A higher stepping speed could be accompanied by a larger step size.

Although the minimum slit width was not demonstrated, this actuation step size is an indicator that the target width could be achieved with further tuning of the setup.

7.1.3. Test setup limitations

Imperfect incoming light source

As illustrated in Figure 6.2, multiple aberrations are visible in the wavefront of the light source. Firstly, the airy disk caused by the combination of the laser and beam expander. Secondly, diffraction bands that arise from the light diffracting from the mechanism itself. This non-uniform wavefront in combination with the very thin slit might be an additional source of uncertainty in the measured diffraction patterns.

Imperfect slit

As mentioned in 6.2, the diffraction bands show serrated edges, where smooth transitions are expected from a theoretical Fraunhofer diffraction pattern. This is caused by imperfect slit edges. The cleaving method used did not produce the effect described in Section 4.1.3. Rather than two straight parallel edges resulting from cleaving, the cleave followed the etch angle for one of the two etched surfaces, resulting in a sharp rather than a blunt edge. Although this does not matter for the transmittance when using $405\ \mathrm{nm}$ light, the sharp edge is extremely fragile and prone to damage. As the width of the slit reduces, the tolerances on the slit edge become increasingly stringent. The serrated edge introduces variation of the seen slit width along the slit length, as seen by the scatter plots produces for the angular alignment.

Angular misalignment in the test setup

Another possible cause for the diffraction pattern breaking down on one side is misalignment of the various parts in the whole setup. Both beam misalignment and camera sensor misalignment can be the cause of this, as they both introduce path length differences. Misalignment of the mechanism can also introduce measurement errors. However, careful alignment as described in Appendix B should mitigate this issue.

For the system that is to be deployed in the XRI vacuum setup, this limitation should not be present due to high manufacturing tolerances and careful selection of dates for each part.

Offset between wafers along the optical axis

Furthermore, the introduction of an axial offset between the wafers along the optical axis diminishes the clarity of the experimental results. Although the resulting behavior from this is expected and consistent with theory, it negatively impacts the definition of the diffraction pattern. Since the central maximum disappears, another variable is introduced in the manual fitting of the intensity profile. Normally, identifying the exact center of the diffraction pattern is straightforward. This effect, along with the limitations of the measurement setup previously highlighted, makes it difficult to judge the validity of the smallest measured slit width.

Internal reflections

As both the camera sensor and the mechanism and snout are made of reflective surfaces, there were stray reflections falling on the sensor. These reflections reduce the signal-to-noise ratio and subsequently decrease the reliability of the measurements. The reflections were one of the reasons that the automatic curve fitting was not possible.

Measurement imperfections

The physical alignment and measurement of the experimental setup introduced further uncertainties. Although the optical table on which the setup was mounted uses tight tolerances, the spacer on which the mechanism was mounted was manufactured using loser tolerances.

Furthermore, the distance between the slits and the camera sensor (L) was measured using a vernier caliper, which has a finite accuracy. In addition, the measurement was further complicated by limited physical access, requiring a visual estimation, as the vernier calipers could not be placed directly against the mechanism to measure the distance to the sensor. Although the distance is stable across one measurement test, it is still an additional source of inaccuracy for the found width of the slit, as the slit width was derived from the Fraunhofer model assuming a specific sensor distance.

7.2. Recommendations for future work

Based on the findings from this research, there are some areas where future work can improve the performance of the slit mechanism and the maturity of the TO.

Testing in vacuum

The current optical setup is a great method to characterize the performance of the mechanism. However, it would be of great benefit if the full system is tested in vacuum, utilizing an actual X-ray source. This will further test the capabilities of the mechanism, as the tolerances for these much lower wavelengths are even more stringent.

Testing with x-rays
Ultimately, the mechanism should also be able to produce the required diffraction pattern for x-rays. Testing with x-rays will bring advantages and disadvantages. Using x-rays, the produces diffraction pattern is actually less sensitive to the offset between wafers, as follows from Vlieg et al., 1997. However, the angular alignment of the beam to the wafers is more stringent, as the wafers become slightly transparent to x-rays.

Wafer slit edges
The jagged slit edges of the wafers used for the slit are a source of uncertainty in the measurement setup. Testing with idealized slit edges will eliminate this uncertainty and may allow the Fraunhofer pattern to be observed at a slit width of $0.5\ \mu\mathrm{m}$ slit width. Furthermore, while a sharp point is sufficient for visible light, it is not adequate for x-rays, as stated in Sections 3.3 and 4.1.3.

Removal of reflections and stray light
Currently the camera sensor is being exposed to light artifacts from reflections. Applying anti-reflective coatings like acktar black foils to all relevant reflective surfaces will likely eliminate these reflections. This will greatly improve the signal to noise ratio. This in turn could allow automatic curve fitting to be used, enhancing objectivity of the results.

Slit actuation
To minimize the variance in step size observed in Section 6.2.3, the stepping speed should be set to the lowest possible value. Furthermore, it is best to actuate with small increments, as this limits the variance between stepping increments.

Feasibility of the optimized domain
Although the current TO formulation proves capable of creating a multi DoF mechanism, there is the shortcoming that the constraints are not being adhered. This is the place where the largest gains can be made immediately. By either changing the constraints or optimization scheme this issue could be alleviated, greatly enhancing the ability to directly implement the mechanism into the XRI setup.

3D optimization
Performing TO using a 3D instead of 2D model would be another place where gains could be made. 3D optimization could yield more robust, novel topologies that are better suited for the challenges of XRI. In addition, the performance requirements for the out of plane parasitic displacements could be added directly as constraints, instead of being something to validate after the optimization.

Stress constraints
Currently no attention is paid to the stress build up in the optimized domain under actuation. The reason for this is twofold. Firstly, it adds another layer of complexity to an already highly complex optimization problem. Secondly, due to the virtual springs and accompanying unrealistically high displacements, stress constraints can not be added directly to the optimization model. Adding stress constraints will greatly help the direct applicability of the TO in a practical setup, as long term durability of the found topologies can then be ensured.

8

Conclusion

At the start of this MSc thesis, two main questions were asked. The first goal was to develop a high-precision adjustable slit mechanism for XRI, based on the following research questions:

The second objective was to explore the capabilities of topology optimization to produce a better alternative to a traditionally designed counterpart.

Traditional design and experimental verification

This research aimed to develop a high aspect ratio adjustable slit for the XRI test bed. This goal was approached using the following main question:

How can a high aspect ratio adjustable slit mechanism be designed to provide control over slit width and angular alignment to adhere to the requirements of the XRI test bed?

To further focus the research to achieve this goal, two sub questions were posed. The first is:

Which mechanism and actuation method yield sub micron precision and control to produce an adjustable slit with the required dimensional tolerances?

Using traditional design methods, a monolithic compliant mechanism was designed, parametrically optimized, and manufactured. High-precision piezo inertia actuators were selected to provide the sub-micron actuation resolution. To maintain sufficient alignment, a mounting system including a piezo translation stage were designed to mount the mechanism in the XRI test bed. Simulations validated that the design complies with the set performance requirements regarding required eigenfrequency and parasitic displacements within the typical operating range.

The second sub question evaluated the designs performance:

To what extent does the developed prototype meet the operational requirements for the specified slit dimensions?

To answer this question, experimental verification was performed using diffraction analysis with a $405\ \mathrm{nm}$ laser source. Although the threshold for producing a clear Fraunhofer diffraction pattern was $3.2\ \mu\mathrm{m}$, analysis using manual fits suggested slit widths as small as $1.8\ \mu\mathrm{m}$. However, the required $0.5\ \mu\mathrm{m}$ width was not reliably achieved. Angular alignment tests showed angular alignment of $4.15\ \mathrm{arcsec}$, indicating that the mechanism is able to achieve the required parallelism. Actuation characterization tests show step size resolution of $0.1 - 0.2\ \mu\mathrm{m}$. Although this is not a guaranty, it indicates the potential of the mechanism to produce the required dimensions. In conclusion, the designed and manufactured mechanism provides the necessary angular alignment needed for the XRI system, where further research is necessary to find the required width. Furthermore, the adequacy of the mechanism for x-rays is as of yet unproven.

Topology Optimization

The second goal of this thesis was to find an alternative design using TO that outperforms the traditional counterparts. The research was guided by the central research question:

'Can topology optimization be used to generate a slit mechanism that performs better than a traditionally designed counterpart?'

To address this, the first sub-question investigated the necessary methodological framework:

Which methods need to be combined to find a mechanism that meets the design challenges?

It was found that five optimization methods had to be combined to come to a functional and decoupled topology. Using compliance minimization as a foundation, the TO formulation was extended with parasitic motion suppression, decoupling, stiffness constraints, and a robust formulation. This combined approach was essential to tailor the compliant mechanism produced to the requirements of the design challenge.

The second sub-question addressed the role of the designer:

Where is designer input necessary to find a practically viable solution and where can this be minimized?

The results indicate that user intervention remains critical, particularly to tune the virtual load setup and deal with non-contributing material. Furthermore, the GCMMA optimizer struggled with adhering to all constraints set, meaning that further tuning of the constraints and problem formulation is necessary.

To come back to the main research question, simulated validation of the TO design on face value showed to outperform the traditional design, specifically in a higher achieved eigenfrequency. However, due to the constraint violations and subsequent overall stiffer design direct comparison is complicated, as a lower domain stiffness is accompanied by a totally different topology. The results do show that TO is a viable and promising alternative to produce these complex multi DoF compliant mechanisms, though as of yet it can not be employed without designer oversight.

Final remark

While the traditional design has the potential to be used in the XRI test bed, further research is needed to prove that the required slit dimensions can be achieved. Topology Optimization gives a path to future iterations with potentially improved performance, provided the constraint violations are tackled.

References

Akiyama, K., Alberdi, A., Alef, W., Asada, K., Azulay, R., Baczko, A.-K., Ball, D., Baloković, M., Barrett, J., Bintley, D., Blackburn, L., Boland, W., Bouman, K. L., Bower, G. C., Bremer, M., Brinkerink, C. D., Brissenden, R., Britzen, S., Broderick, A. E., … Ziurys, L. (2019). First M87 Event Horizon Telescope Results. I. The Shadow of the Supermassive Black Hole. *The Astrophysical Journal Letters*, *875*(1), L1. https://doi.org/10.3847/2041-8213/ab0ec7

Avantier Inc. (2023). *Forgetting the diffraction limit: Avoid optical pitfalls part 2*. Avantier. Retrieved May 2, 2026, from https://avantierinc.com/resources/diffraction-limit/

Bendsøe, M. P. (1989). Optimal shape design as a material distribution problem. *Structural Optimization*, *1*(4), 193–202. https://doi.org/10.1007/BF01650949/METRICS

Bendsøe, M. P., & Sigmund, O. (2004). *Topology Optimization*. Springer Berlin Heidelberg. https://doi.org/10.1007/978-3-662-05086-6

Bendsøe, M. P., & Kikuchi, N. (1988). Generating optimal topologies in structural design using a homogenization method. *Computer Methods in Applied Mechanics and Engineering*, *71*(2), 197–224. https://doi.org/10.1016/0045-7825(88)90086-2

Bourdin, B. (2001). Filters in topology optimization. *International Journal for Numerical Methods in Engineering*, *50*(9), 2143–2158. https://doi.org/10.1002/nme.116

Bruns, T. E., & Tortorelli, D. A. (2001). Topology optimization of non-linear elastic structures and compliant mechanisms. *Computer Methods in Applied Mechanics and Engineering*, *190*(26-27), 3443–3459. https://doi.org/10.1016/S0045-7825(00)00278-4

Cash, W. (2003). X-Ray Interferometry. *Experimental Astronomy*, *16*(2), 91–136. https://doi.org/10.1007/s10686-004-2523-5

Cash, W., Shipley, A., Osterman, S., & Joy, M. (2000). Laboratory detection of X-ray fringes with a grazing-incidence interferometer. *Nature*, *407*(6801), 160–162. https://doi.org/10.1038/35025009

COMSOL AB. (2025). *Structural mechanics user's guide* [pp 521-522]. Version COMSOL Multiphysics ® 6.4. COMSOL AB. Stockholm, Sweden.

den Hartog, R. H., Uttley, P., Willingale, R., Hoevers, H., den Herder, J.-W., & Wise, M. (2020). The development of a testbed for the x-ray interferometry mission, 100. https://doi.org/10.1117/12.2562831

Dirksen, F., Berg, T., Lammering, R., & Zohdi, T. I. (2012). Topology synthesis of large-displacement compliant mechanisms with specific output motion paths. *PAMM*, *12*(1), 801–804. https://doi.org/10.1002/PAMM.201210384

Farhadi Machekposhti, D., Tolou, N., & Herder, J. L. (2015). A Review on Compliant Joints and Rigid-Body Constant Velocity Universal Joints Toward the Design of Compliant Homokinetic Couplings. *Journal of Mechanical Design*, *137*(3). https://doi.org/10.1115/1.4029318

Fowles, G. R. (2012). *Introduction to modern optics*. Dover Publications, Inc.

Goodman, J. W. (2000). *Statistical optics* [Relevant sections: Chapter 5]. Wiley-Interscience.

Guest, J. K., Prévost, J. H., & Belytschko, T. (2004). Achieving minimum length scale in topology optimization using nodal design variables and projection functions. *International Journal for Numerical Methods in Engineering*, *61*(2), 238–254. https://doi.org/10.1002/nme.1064

Haber, R. B., Jog, C. S., & Bendsoe, M. P. (1996). *A new approach to variable-topology shape design using a constraint on perimeter* (tech. rep.). Springer-Verlag.

Koppen, S., Langelaar, M., & van Keulen, F. (2022). A simple and versatile topology optimization formulation for flexure synthesis. *Mechanism and Machine Theory*, *172*. https://doi.org/10.1016/j.mechmachtheory.2022.104743

Kuan Yong, Y., Lu, T.-F., & Handley, D. C. (2008). Review of circular flexure hinge design equations and derivation of empirical formulations. *Precision Engineering*, *32*, 63–70. https://doi.org/10.1016/j.precisioneng.2007.05.002

Lawrence Berkeley National Laboratory's. (2010). X-ray interactions with matter [Online; accessed 27-January-2026]. https://henke.lbl.gov/optical_constants/

Lazarov, B. S., & Sigmund, O. (2011). Filters in topology optimization based on Helmholtz-type differential equations. *International Journal for Numerical Methods in Engineering*, *86*(6), 765–781. https://doi.org/10.1002/nme.3072

Liu, Z., & Korvink, J. G. (2009). Using artificial reaction force to design compliant mechanism with multiple equality displacement constraints. *Finite Elements in Analysis and Design*, *45*(8-9), 555–568. https://doi.org/10.1016/J.FINEL.2009.03.005

Luo, Z., Chen, L., Yang, J., Zhang, Y., & Abdel-Malek, K. (2005). Compliant mechanism design using multi-objective topology optimization scheme of continuum structures. *Structural and Multidisciplinary Optimization*, *30*(2), 142–154. https://doi.org/10.1007/s00158-004-0512-y

Monnier, J. D. (2003). Optical interferometry in astronomy. *Reports on Progress in Physics*, *66*(5), 789. https://doi.org/10.1088/0034-4885/66/5/203

Nocedal, J., & Wright, S. J. (2006). *Numerical optimization* (2nd ed.). Springer.

Rahmatalla, S., & Swan, C. C. (2005). Sparse monolithic compliant mechanisms using continuum structural topology optimization. *International Journal for Numerical Methods in Engineering*, *62*, 1579–1605. https://doi.org/10.1002/nme.1224

Seltmann, S., & Hasse, A. (2023). Topology optimization of compliant mechanisms with distributed compliance (hinge-free compliant mechanisms) by using stiffness and adaptive volume constraints instead of stress constraints. *Mechanism and Machine Theory*, *180*. https://doi.org/10.1016/j.mechmachtheory.2022.105133

Sigmund, O. (1997). On the Design of Compliant Mechanisms Using Topology Optimization*. *Mechanics of Structures and Machines*, *25*(4), 493–524. https://doi.org/10.1080/08905459708945415

Sigmund, O. (2007). Morphology-based black and white filters for topology optimization. *Structural and Multidisciplinary Optimization*, *33*(4-5), 401–424. https://doi.org/10.1007/s00158-006-0087-x

Sigmund, O. (2009). Manufacturing tolerant topology optimization. *Acta Mechanica Sinica/Lixue Xuebao*, *25*(2), 227–239. https://doi.org/10.1007/s10409-009-0240-z

Smith, C. L. C., Stenger, N., Kristensen, A., Mortensen, N. A., & Bozhevolnyi, S. I. (2015). Gap and channelled plasmons in tapered grooves: a review. https://doi.org/10.1039/c5nr01282a

Svanberg, K. (1987). The method of moving asymptotes—a new method for structural optimization. *International Journal for Numerical Methods in Engineering*, *24*(2), 359–373. https://doi.org/10.1002/NME.1620240207

Svanberg, K. (2002). A class of globally convergent optimization methods based on conservative convex separable approximations. *SIAM Journal on Optimization*, *12*(2), 555–573. https://doi.org/10.1137/S1052623499362822

Tonomura, A., Endo, J., Matsuda, T., Kawasaki, T., & Ezawa, H. (1989). Demonstration of single-electron buildup of an interference pattern. *American Journal of Physics*, *57*(2), 117–120. https://doi.org/10.1119/1.16104

Uttley, P., Hartog, R. d., Bambi, C., Barret, D., Bianchi, S., Bursa, M., Cappi, M., Casella, P., Cash, W., Costantini, E., Dauser, T., Trigo, M. D., Gendreau, K., Grinberg, V., Herder, J. W. d., Ingram, A., Kara, E., Markoff, S., Mingo, B., … Wise, M. (2021). The high energy Universe at ultra-high resolution: the power and promise of X-ray interferometry. *Experimental Astronomy*, *51*(3), 1081–1107. https://doi.org/10.1007/S10686-021-09724-W

Vlieg, E., De Vries, S. A., Alvarez, J., & Ferrer, S. (1997). Slits as adjustable pinholes for coherent X-ray scattering experiments. *Journal of Synchrotron Radiation*, *4*(4), 210–213. https://doi.org/10.1107/S0909049597003919

Wang, F., Lazarov, B. S., & Sigmund, O. (2011). On projection methods, convergence and robust formulations in topology optimization. *Structural and Multidisciplinary Optimization*, *43*(6), 767–784. https://doi.org/10.1007/s00158-010-0602-y

Willingale, R. (2004, October). A practical system for x-ray interferometry. In G. Hasinger & M. J. L. Turner (Eds.). https://doi.org/10.1117/12.552917

Zhu, B., Chen, Q., Jin, M., & Zhang, X. (2018). Design of fully decoupled compliant mechanisms with multiple degrees of freedom using topology optimization. *Mechanism and Machine Theory*, *126*, 413–428. https://doi.org/10.1016/j.mechmachtheory.2018.04.028

Zhu, B., Zhang, X., Zhang, H., Liang, J., Zang, H., Li, H., & Wang, R. (2020). Design of compliant mechanisms using continuum topology optimization: A review. *Mechanism and Machine Theory*, *143*, 103622. https://doi.org/10.1016/J.MECHMACHTHEORY.2019.103622

Zubir, M. N. M., Shirinzadeh, B., & Tian, Y. (2009). Development of a novel flexure-based microgripper for high precision micro-object manipulation. *Sensors and Actuators, A: Physical*, *150*(2), 257–266. https://doi.org/10.1016/j.sna.2009.01.016

A

Slit dimension tolerances

The tables for the tolerances, including an overview of what is meant with each DoF:

DOF	Tolerance	Schematic
Translation in X *	$\pm 10\ \mu$m	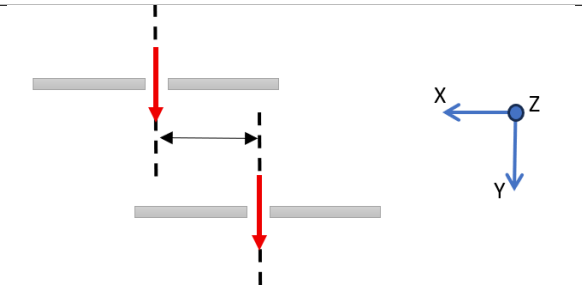
Translation in Y	± 5 mm	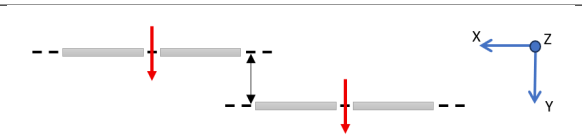
Translation in Z	± 1 mm	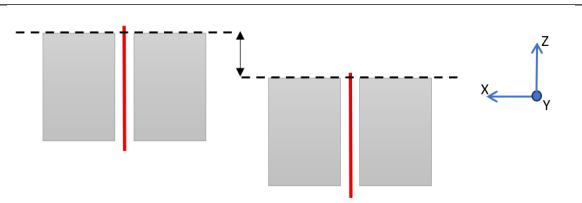
Rotation around X	± 1 degree	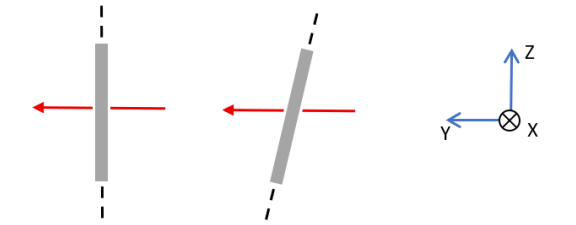
Rotation around Y	± 1 degree	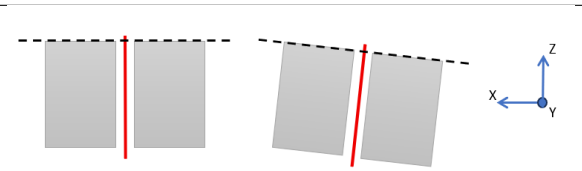
Rotation around Z	± 5 mrad	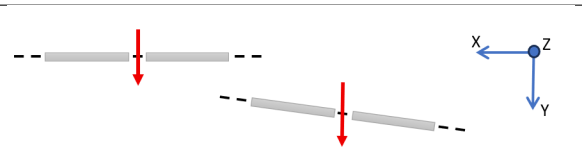

Table A.1: Positioning tolerances for the slit assembly as a whole. Note that in these Tables, the red arrow/line indicates the X-ray beam, which moves in positive Y. The dashed lines are added as reference lines to increase readability. The gray areas represent the wafers that are used to create the slit.

DoF	Tolerance	Schematic
Translation of one wafer in X *	$0.1\ \mu m$	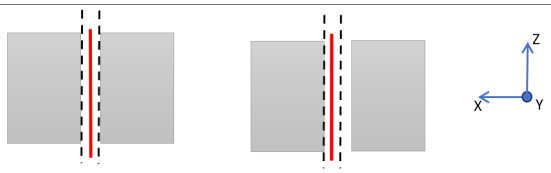
Translation of one wafer in Y	$\pm 20\ \mu m$	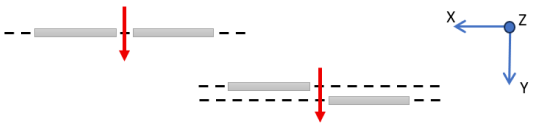
Translation of one wafer in Z	$\pm 1\ mm$	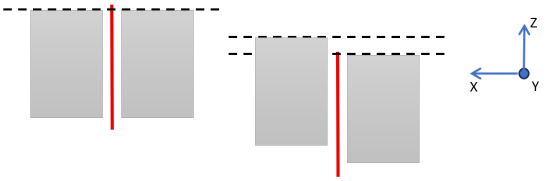
Rotation of one wafer around X	$\pm\ 1°$	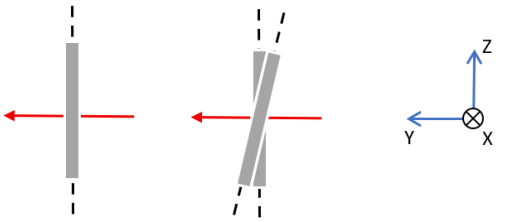
Non parallel slit edge *	± 10 arcsec	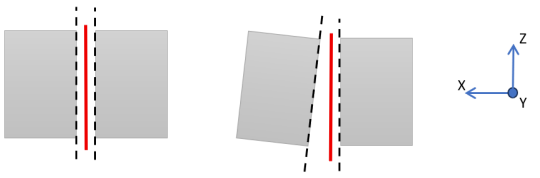
Rotation of one wafer around Z	± 5 mrad	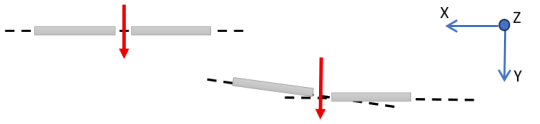

Table A.2: Tolerances for relative positioning errors between the two wafer edges.

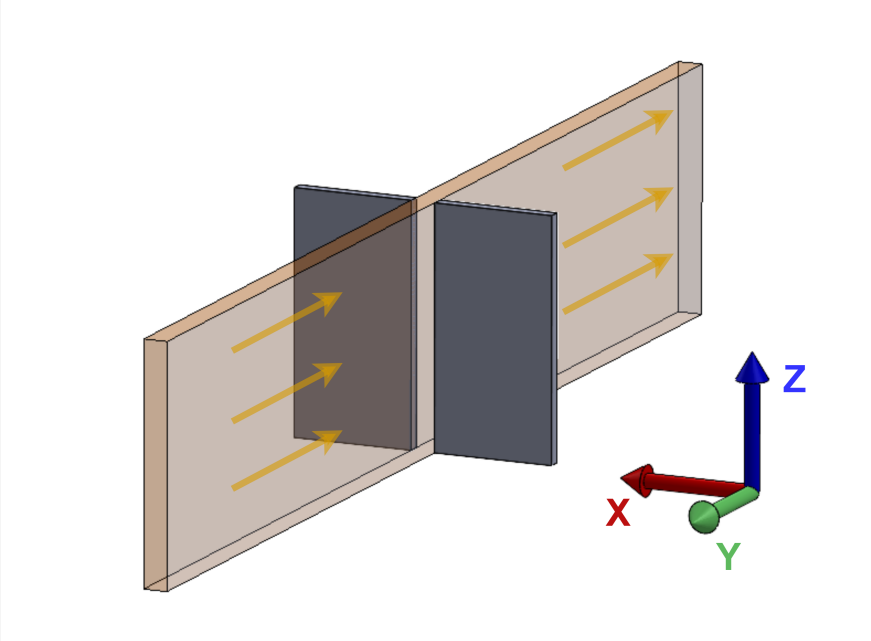

Figure A.1: Definition of the axis orientation used for Table A.1 and A.2. The wafers are depicted by the gray boxes. The beam path is shown with the transparent orange box, moving toward the negative Y direction.

B

Test setup

B.1. Setup alignment

As mentioned in Chapter 6, a laser in combination with a beam expander was used to provide a light source for the verification. To properly align the laser and beam expander, the following method was used.

B.1.1. Laser alignment

First, the laser was placed on an optical table along with two irises in the intended beam path. Then, the iris closest to the laser source was closed gradually, until the laser beam no longer passed through the iris. When this happened, the pointing of the laser beam was adjusted until the laser passed through the iris again. This was repeated until the diameter of the laser beam was larger than the pupil of the iris, and was nicely centered on the pupil. Then, the iris was opened again. The second iris is then gradually closed using the same method. When the laser again is larger the pupil of the second iris and the laser passes through its middle the alignment should be okay. This can be verified by alternating closing either iris. If the observed laser beam narrows and widens symmetrically, the laser is aligned well.

A schematic can be seen in Figure B.1.

B.1.2. Beam expander alignment

After this, the beam expander is placed in the beam path of the laser. By partially covering the entrance lens of the beam expander with a piece of paper, the location of the laser beam can be determined in relation to the beam expander. After the entrance lens is aligned, a tip-tilt stage is used to align the rest of the beam expander. The airy disk present in the resulting widened beam can be used to check this alignment. If the beam gives perfect airy disks (Figure B.2), the beam expander is properly aligned with the laser source.

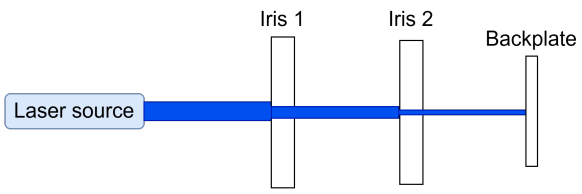

Figure B.1: Schematic of the setup used to align the laser source.

Figure B.2: An example of an airy disk pattern, as would be found from a perfectly aligned beam expander, from Avantier Inc., 2023.

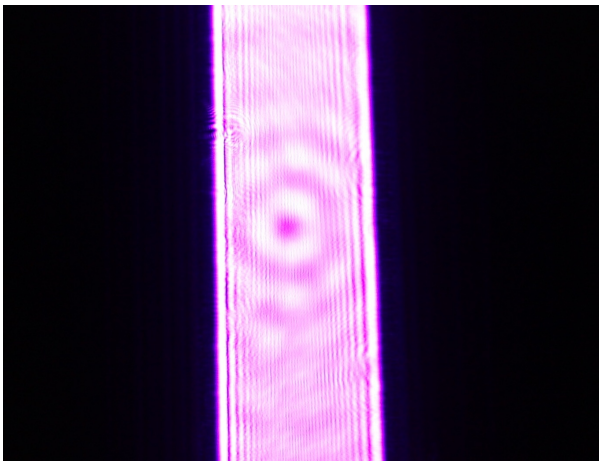

Figure B.3: Image of the light beam captured without any wafers mounted. The (near) vertical diffraction bands can be used to determine the angular alignment.

B.1.3. Mechanism alignment

To properly align the mechanism the camera can be used. By removing the wafers from the snouts, the incoming wavefront can be analyzed. As the wavefront diffracts from the sharp mechanism edges, (near) vertical diffraction bands can be seen in the detected image (Figure B.3). These diffraction bands can be used to judge the alignment of the mechanism. If the width of the bands from the two mechanism edges is symmetrical, the mechanism is aligned properly. However, this is a qualitative visual assessment, so the exact angular orientation is unknown.

B.1.4. Camera alignment

To align the camera, the lens mount ring can be used in unison with the diagonal bars present in the snouts. As the dimensions of the snout and the distance from the camera's lens mount ring to the sensor are known, they can be used to determine the distance between the slit and sensor. To do so, a visual assessment was done, where the mount ring was aligned with a distinct point on the snout. To control the angular alignment, the second snout is used. The plane used to align the camera is indicated in Figure B.4.

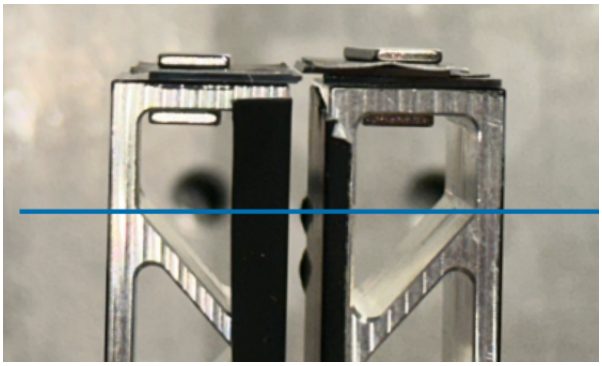

Figure B.4: Alignment plane used to determine the distance from the slit to the sensor.

B.2. Mechanism operation strategies

There are two methods to achieve the required dimensions for the slit.

The first option is to place the wafers on the slit in the open position, and align them as well as possible by hand. Then, by using the diffraction pattern the wafers can be brought into position step by step. It is critical to alternate actuating the translation and rotation stage, at each step observing the diffraction pattern. First, by translating the wafers closer together, the diffraction pattern gets wider. As this happens, the angle between the wafers is indicated by a gradual widening or narrowing of the Diffraction pattern. Figure B.5 shows this effect. Perhaps counter-intuitively, the diffraction pattern shows the reverse angle of the angle between the wafers. This is because a wider slit gives a narrower diffraction pattern, and vice versa. If the slit is closer at the top than the bottom, the diffraction pattern will be wider at the top than the bottom. So, after an angular difference between slit edges becomes apparent, the rotation side needs to be actuated to alleviate the difference. When the diffraction appears straight again, the translation stage is once again actuated. This loop continues until the angles are achieved.

The second option is to mount the slits on the mechanism when the translation is displaced to its maximum displacement. Then, by placing the wafers on the mechanism touching each other, the slits are automatically aligned. Then, only the translation stage should need to be actuated to open the slit by half a micron. In theory this is a much simpler method. However, touching the wafers together could lead to damage of the wafer edges.

The first method was adopted and proved quite effective.

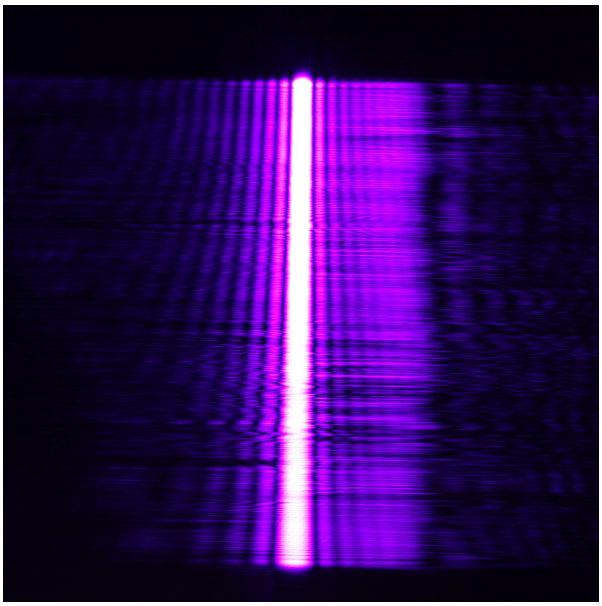

Figure B.5: An example of two misaligned slit halves. The diffraction bands peak to peak distance increases as you move along the slit, indicating an angular offset.

C

Optical test results

C.1. Angular alignment intensity plots

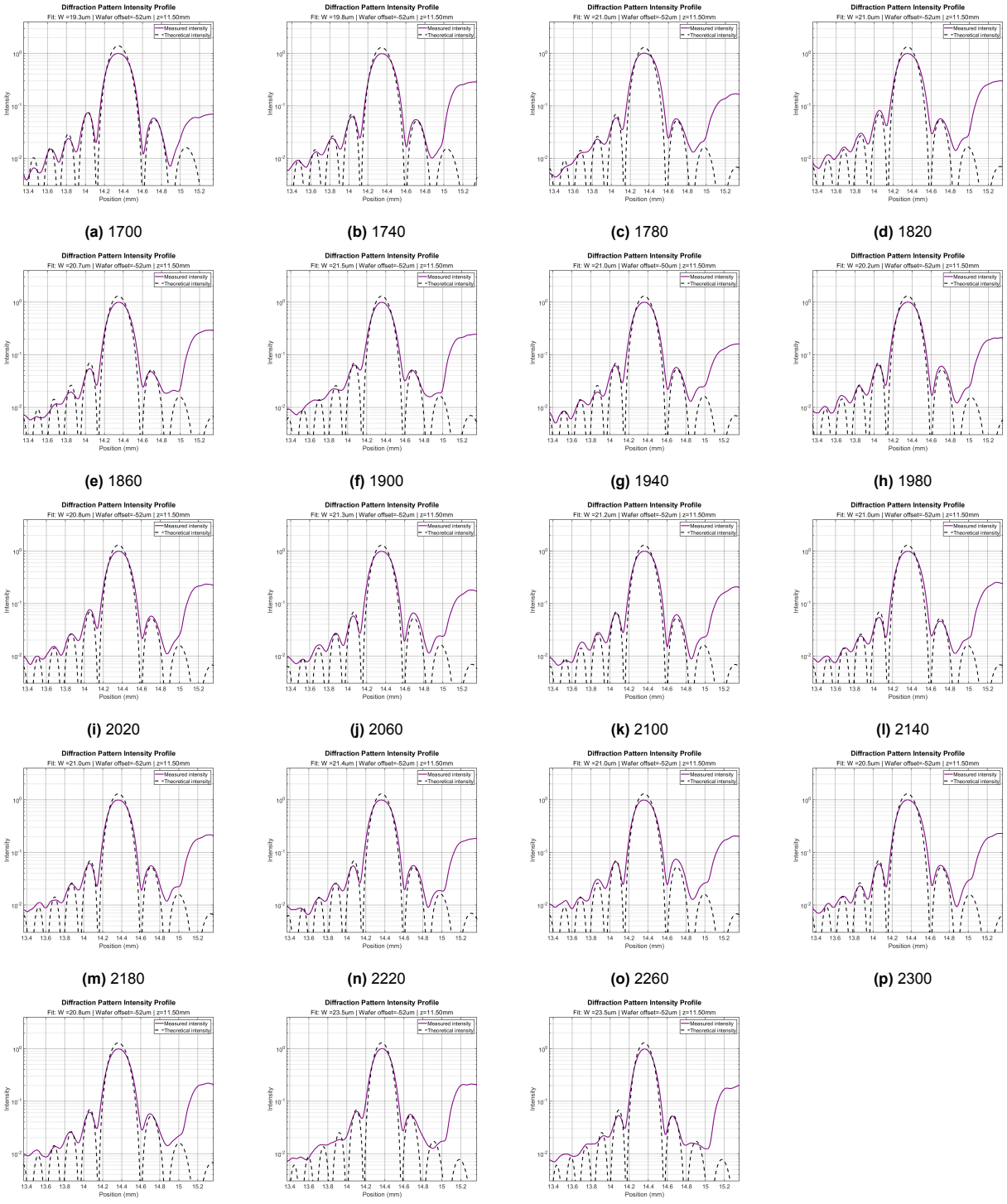

(a) 1700 **(b)** 1740 **(c)** 1780 **(d)** 1820

(e) 1860 **(f)** 1900 **(g)** 1940 **(h)** 1980

(i) 2020 **(j)** 2060 **(k)** 2100 **(l)** 2140

(m) 2180 **(n)** 2220 **(o)** 2260 **(p)** 2300

(q) 2340 **(r)** 2380 **(s)** 2420

Figure C.1: Intensity plots used to analyse the parallelism performance. The numbers equate to the vertical position along the slit, expressed by the pixel number. Figure a equates to 14.1 mm, Figure s equates to 10.0 mm.

C.2. Actuation characterization intensity profiles

C.2.1.

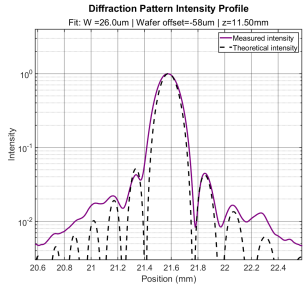

(a) 280

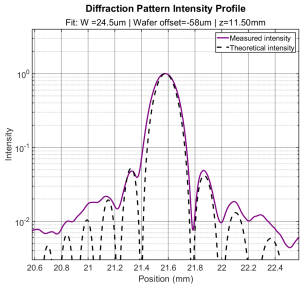

(b) 281

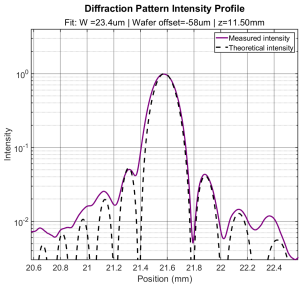

(c) 282

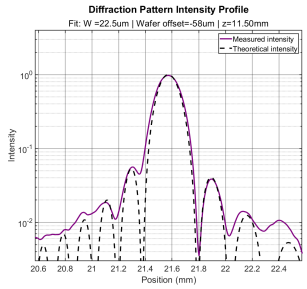

(d) 283

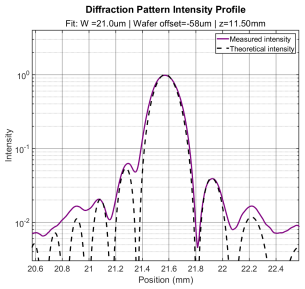

(e) 284

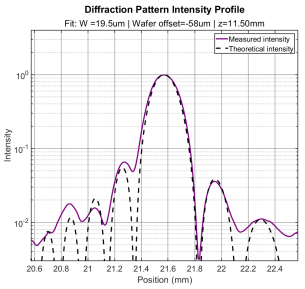

(f) 285

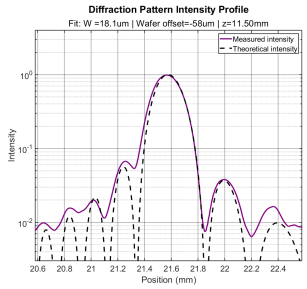

(g) 286

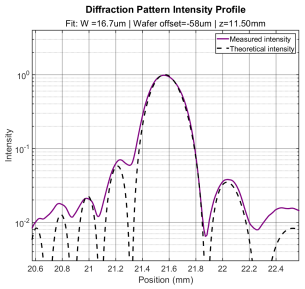

(h) 287

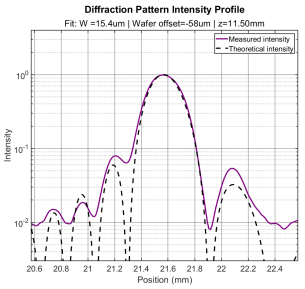

(i) 288

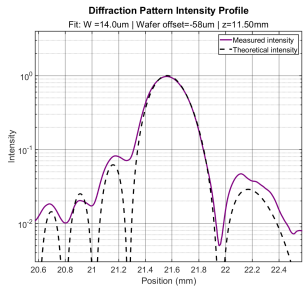

(j) 289

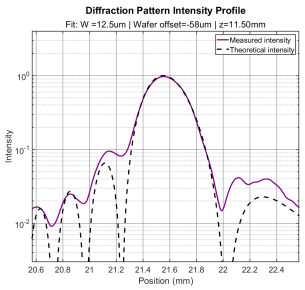

(k) 290

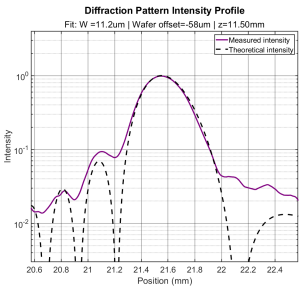

(l) 291

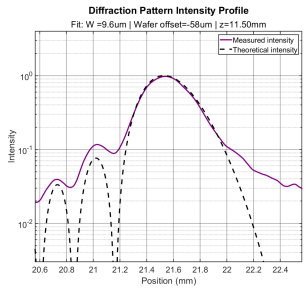

(m) 292

Figure C.2: Overview of intensity profiles used for the scatter plot of the 50 increment actuation characterization test. The numbers each profile indicate the frame number corresponding to each picture used.

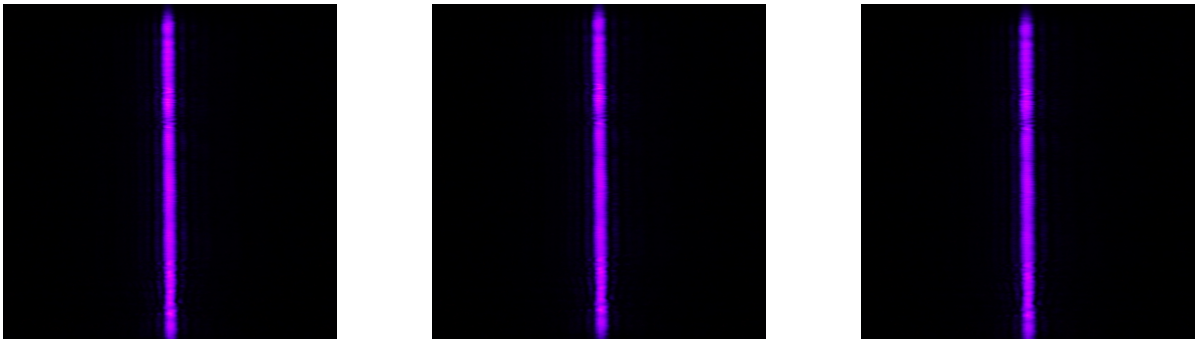

(a) 280

(b) 281

(c) 282

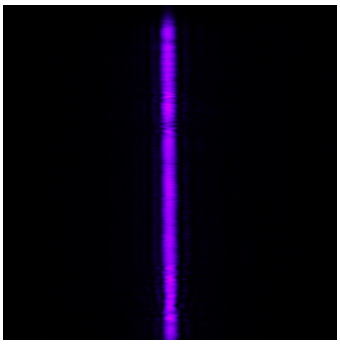

(d) 283

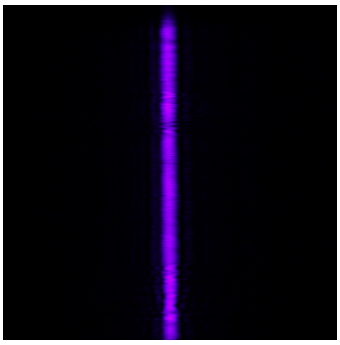

(e) 284

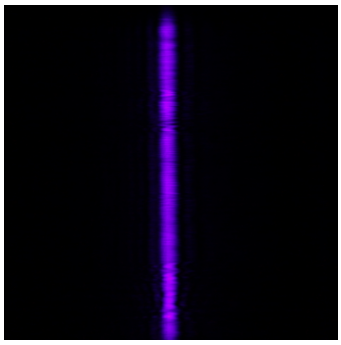

(f) 285

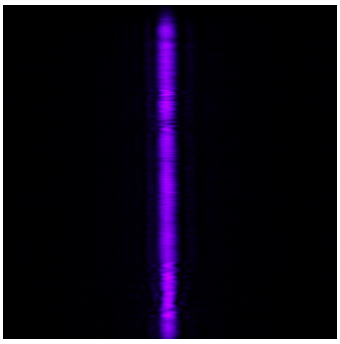

(g) 286

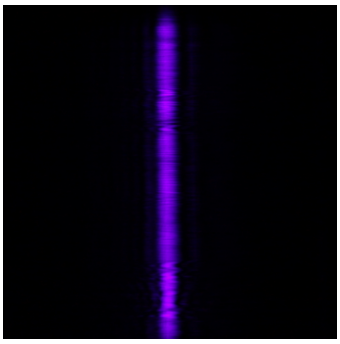

(h) 287

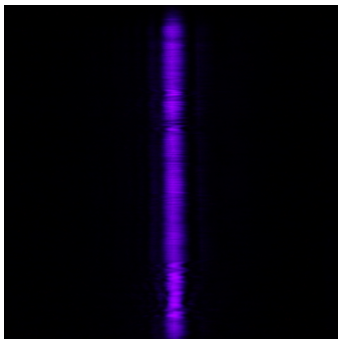

(i) 288

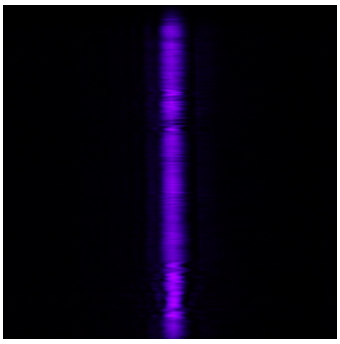

(j) 289

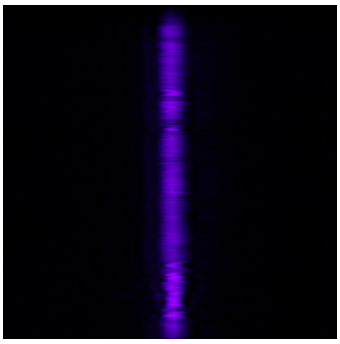

(k) 290

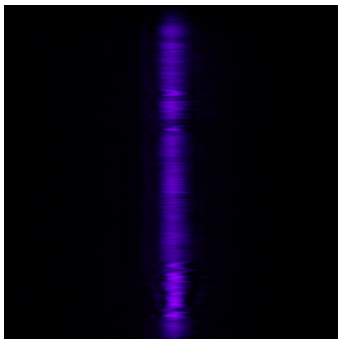

(l) 291

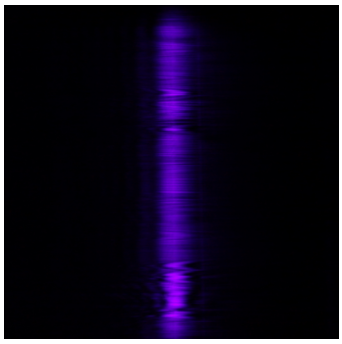

(m) 292

Figure C.3: Overview of the Diffraction patterns used to build the intensity profiles shown for the 50 step increments. The caption indicates the frame number of each image.

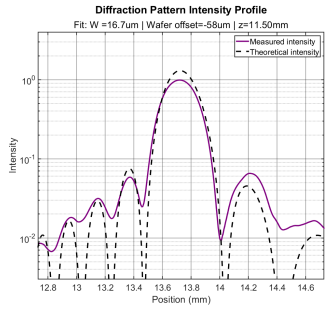

(a) 240

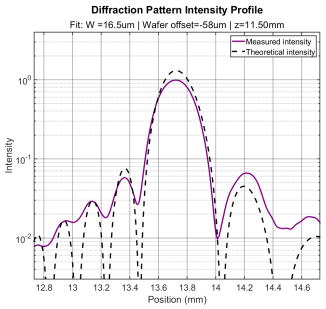

(b) 241

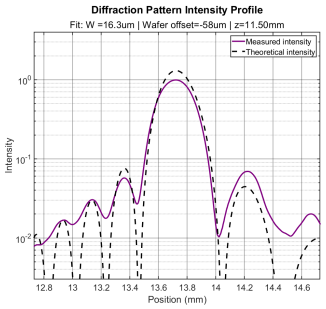

(c) 242

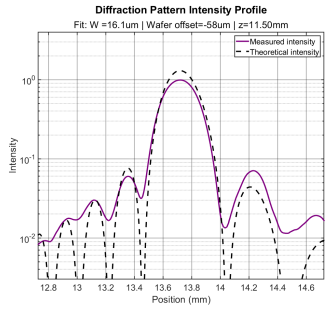

(d) 243

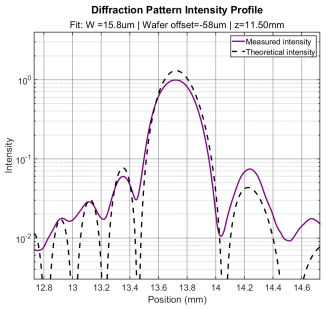

(e) 244

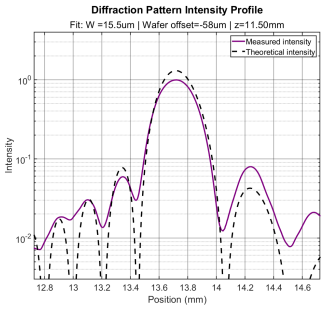

(f) 245

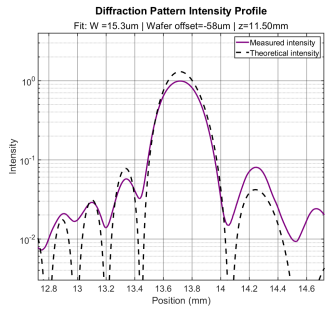

(g) 246

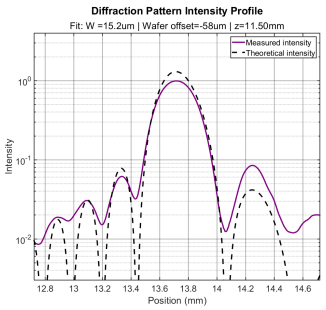

(h) 247

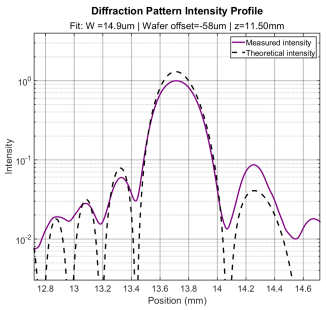

(i) 248

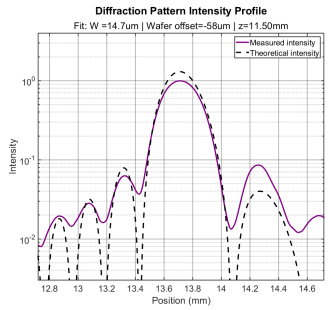

(j) 249

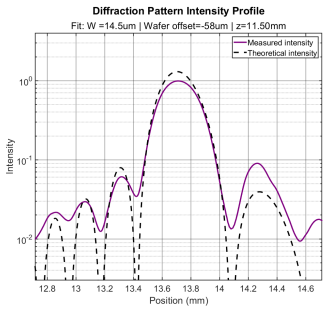

(k) 250

Figure C.4: Overview of intensity profiles used for the linear regression fitting for the 10 step increment actuation characterization test.

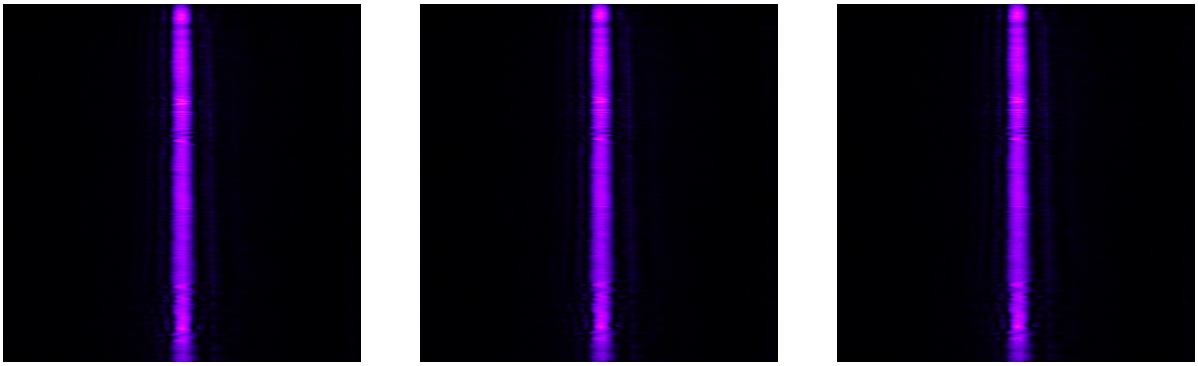

(a) 240 **(b)** 241 **(c)** 242

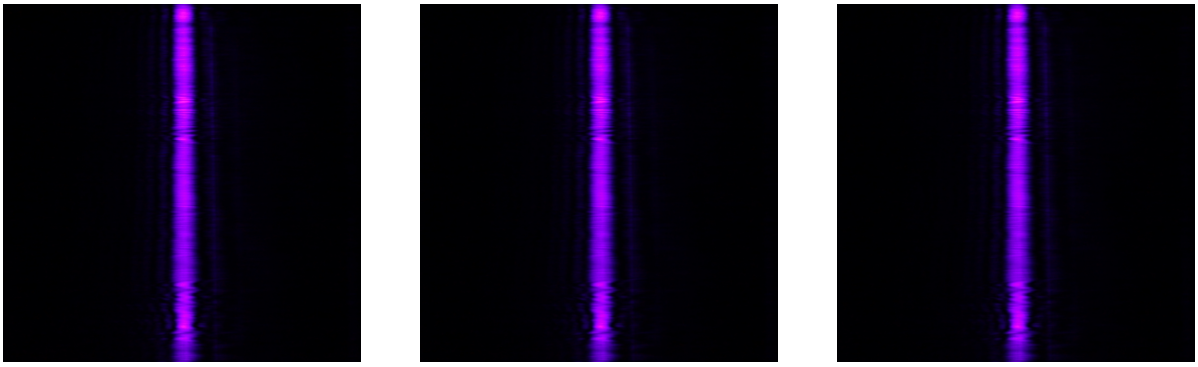

(d) 243 **(e)** 244 **(f)** 245

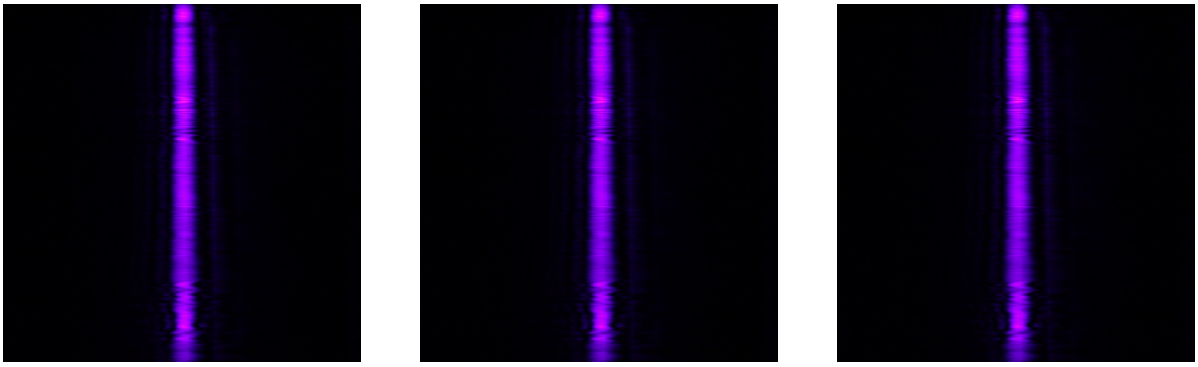

(g) 246 **(h)** 247 **(i)** 248

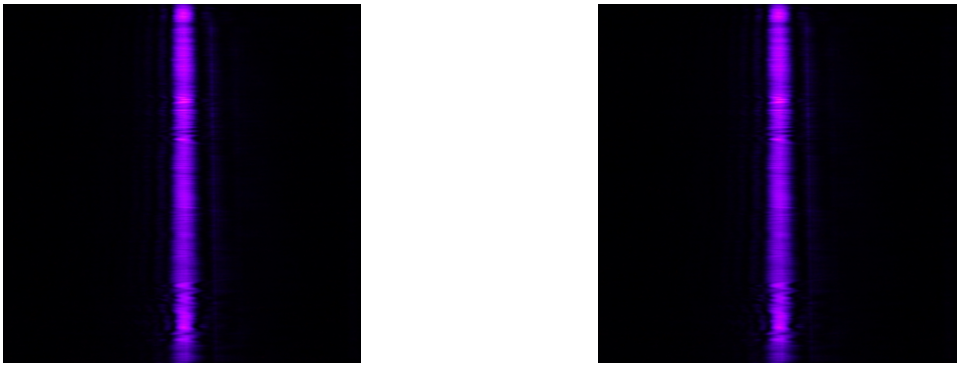

(j) 249 **(k)** 250

Figure C.5: Overview of the Diffraction patterns used to build the intensity profiles shown for the 10 step increments. The caption indicates the frame number of each image.

D

Material selection

As discussed in Section 4.4.1, choosing the right material is crucial. It influences both the stiffness of the hinges and the maximum range of motion that can be achieved. The material properties that are of most importance are the Young's modulus, E and the ultimate Yield strength, σ_y. Looking at Equation 4.4 it becomes evident that the ratio between σ_y and E should be maximized. The Granta Edupack software package can be used to plot the two properties against each other. A graph showing all metals classified for these properties can be seen in Figure D.1. In this graph, the black line indicates the slope where the ratio between the two properties stays the same. Maximizing the ratio between the Young's modulus and Yield strength equates to moving the black line to the top left. Doing so gives some obvious candidates to consider. That is, aluminium alloys, titanium alloys, and low alloy or high carbon steels. For each of these materials the range of motion, stiffness and stress at maximum displacement were determined to rank the material options, using a given set of parameters to allow fair comparison. Table D.1 shows this overview. From these three candidates, titanium alloys give the best performance. Titanium does not necessarily have the highest yield strength, which is achieved with high carbon steels. However, it does offer the best ratio between yield stress and Young's modulus. This means that for any combination of geometric parameters it will have the highest range of motion. A massive downside of titanium is its poor workability. Making a mechanism with small flexures using titanium will cost multiples of the costs when using aluminium for example. The second best performing would be the low alloy or high carbon steels. These types of steel are often used for springs and more recently, compliant mechanisms. They offer a good ratio between Young's modulus and yield strength at much lower costs than titanium. Their relatively high Young's modulus limits their usability for the compliant mechanism designed in this work. The actuators chosen have a low maximum actuation force as will be discussed in Section 4.1.4. So, unrealistically thin flexures would need to be used to ensure that the mechanism does not become too stiff. The right aluminium alloy can give adequate performance with realistic flexure thickness, as will be discussed in Section 4.5. Aluminium is also considerably cheaper and easier to manufacture than titanium and was chosen as the material to use. Specifically Al-7075, because of its high yield strength and low costs.

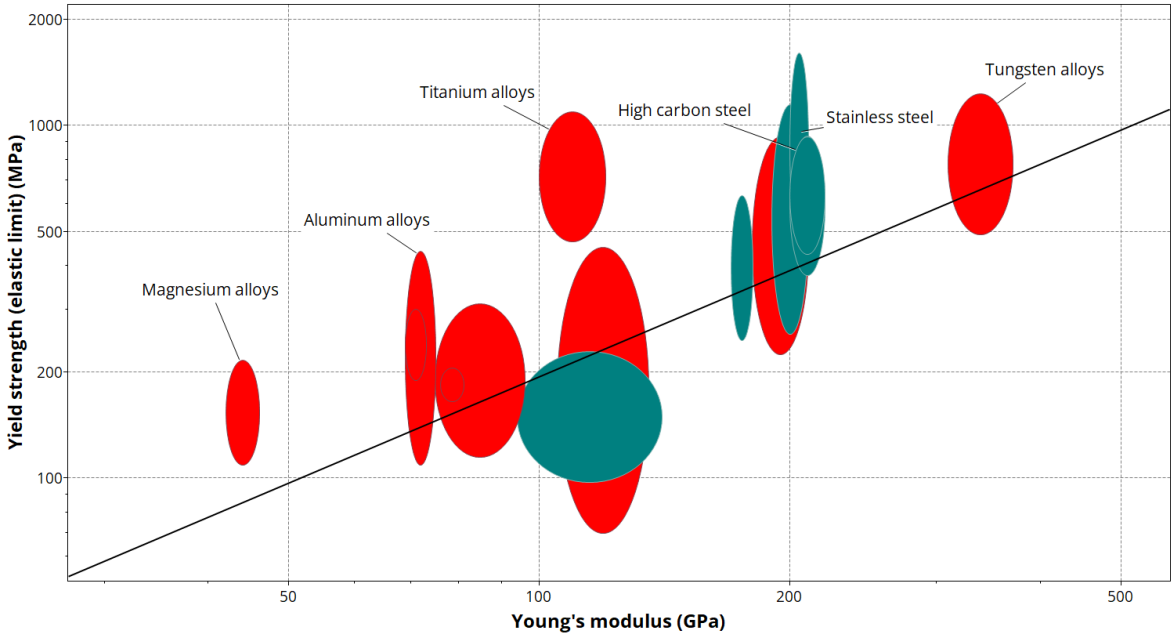

Figure D.1: Yield strength σ_Y versus Young's Modulus E for metals with yield strength over $100\ [MPa]$.

Material	**Al-7075**	**Steel**	**Titanium**	**Invar (cold worked)**
Young's modulus [GPa]	69–76	200–210	100–120	140
Yield strength [MPa]	460–530	470–1600	450–1100	585–725
Flexure thickness [mm]	0.5	0.5	0.5	0.5
Flexure radius [mm]	4	4	4	4
Link length [mm]	80	80	80	80
Plate thickness [mm]	10	10	10	10
Best case scenario results				
Angular ROM [degree °]	2.81	2.97	3.40	1.93
Range of motion [mm]	3.59	3.73	4.28	2.42
Hinge stiffness [Nm/rad]	4.31	12.50	7.50	8.75
Translation actuation stiffness [N/mm]	3.33	9.65	4.82	6.75
Actuation force for required ROM [N]	1.66	4.82	2.89	3.38

Table D.1: Mechanism performance for candidate materials.

E

Hinge optimization

All additional equations used for the parameter optimization:

$$K_{\theta_y} = \frac{Eb^3}{12\beta_3} \tag{E.1}$$

$$K_{\theta_x} = G\left(\frac{2bt^{5/2}}{9\pi R^{1/2}} + \frac{b^3}{12\beta^3}\right) \tag{E.2}$$

$$\text{with } \beta_3 = \left(\frac{2(1+\beta_1)}{\sqrt{2\beta_1+\beta_1^2}}\tan^{-1}\sqrt{\frac{2+\beta_1}{\beta_1}} - \frac{\pi}{2}\right) \tag{E.3}$$

The sensitivities of the objective function to the design variables:

The contour plots for the other combinations of parameters:

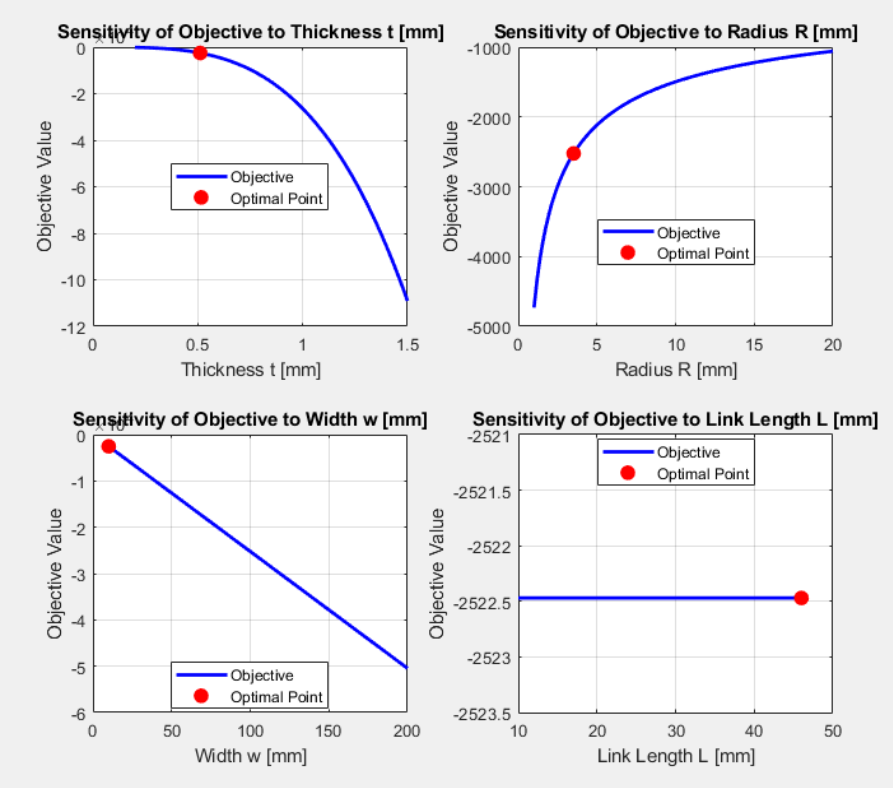

Figure E.1: Sensitivity of the objective function to each design variable.

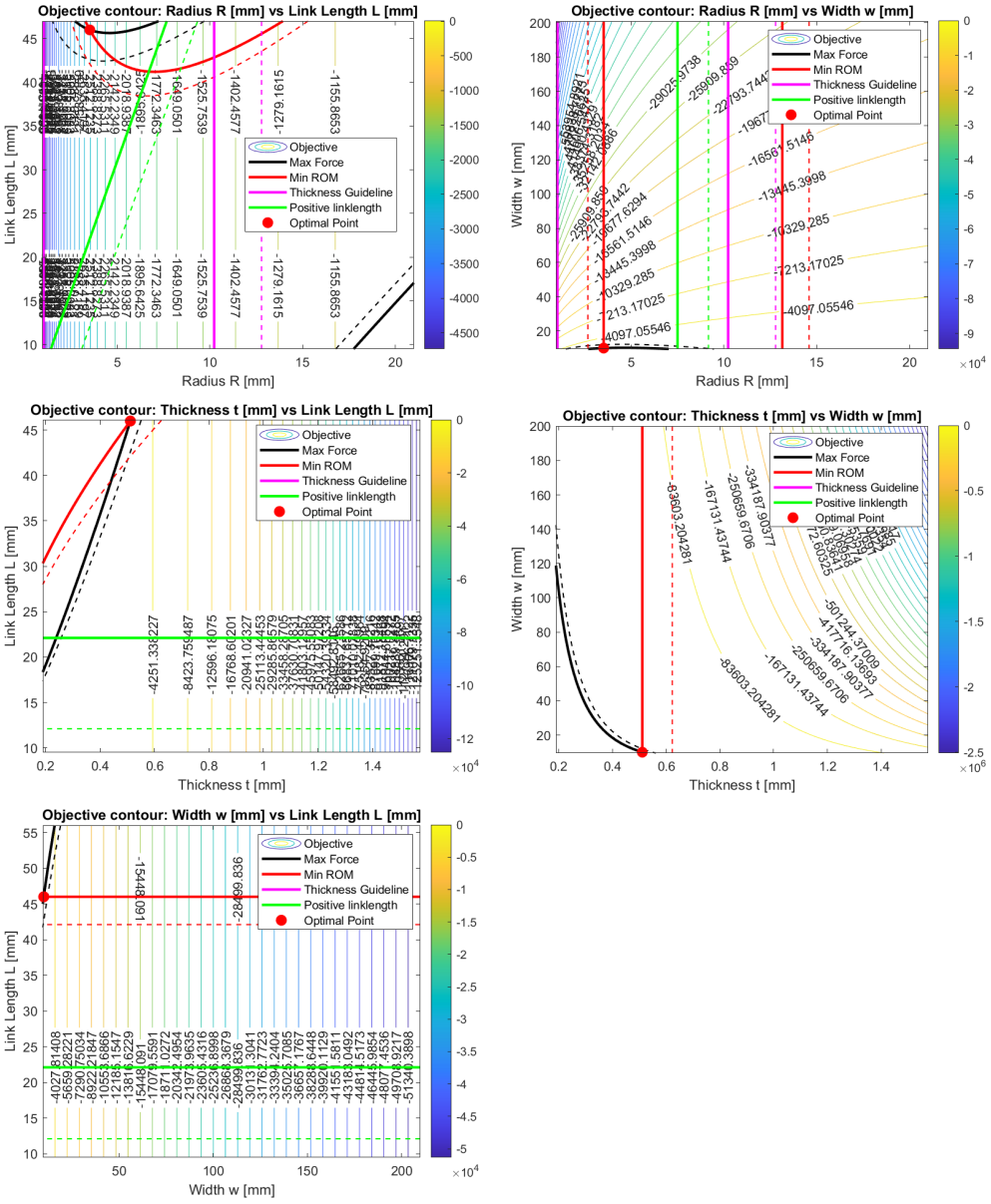

Figure E.2: Parameter optimization contour plots

F

Matlab code

F.1. Parameter optimization

The code used for the parameter optimization performed in Matlab.

```
%% Optimization Setup

t0 = 0.6;   % Initial Thickness
R0 = 4;    % Initial Radius
w0 = 14;    % Initial Width
L0 = 30;  % Initial Link Length

% design variable initialization
x0 = [t0, R0, w0, L0];
lb = [0.2 1, 10, 10]; % Lower Bounds
ub = [1.5, 20, 200, 46];     % Upper Bounds

% optimization options
options = optimoptions('fmincon', 'Display','iter',...
    'TolFun',1e-6,'TolX',1e-6,'TolCon',1e-6,'MaxIter',5000,'MaxFunEvals',5000);


[xopt,fval,exitflag,output,lambda,grad] = fmincon(@ObjMechanism,x0,[],[],[],[],lb,ub,
    @ConstraintCircNotch,options);

[ROM, FB_Kx, Tz, Tzd, Ktz, RatXZ, RatYZ, Ktx] = MechanismAnalytical(xopt(1),xopt(2),xopt(3),
    xopt(4));

%Command line outputs for readability
disp('Optimal design variables:');
disp(['t = ', num2str(xopt(1)), ' mm']);
disp(['R = ', num2str(xopt(2)), ' mm']);
disp(['b_h = ', num2str(xopt(3)), ' mm']);
disp(['L = ', num2str(xopt(4)), ' mm']);
disp(['Objective value): ', num2str(fval)]);
disp(['Range of Motion: ', num2str(ROM), ' mm']);
disp(['Angular Range of Motion: ', num2str(Tzd), ' deg']);
disp(['Hinge Stiffness ', num2str(Ktz), ' N mm/rad']);
disp(['Mechanism Stiffness ', num2str(FB_Kx), ' N/mm']);
disp(['Out of plane stiffness ', num2str(Ktx), ' N mm/rad']);
disp(['Ratio Stiffness XZ: ', num2str(RatXZ)]);
disp(['Ratio Stiffness YZ: ', num2str(RatYZ)]);
disp(['Actuation force at 0.6 mm = ', num2str(FB_Kx*0.6), ' N']);
disp([' Deflection at maximum force = ', num2str(22/FB_Kx), ' mm']);
disp(['Exitflag = ', num2str(exitflag)]);
% Exitflag explanation for readability
switch exitflag
    case 1
        disp('Optimization terminated: First-order optimality conditions satisfied.');
    case 0
```

```
        disp('Optimization terminated: Number of iterations or function evaluations exceeded.
            ');
    case -1
        disp('Optimization terminated: No feasible point found.');
    case 2
        disp('Optimization terminated: Change in x less than tolerance.');
    case 3
        disp('Optimization terminated: Change in objective function less than tolerance.');
    case -2
        disp('Optimization terminated: Problem infeasible.');
    otherwise
        disp(['Optimization terminated: Unknown exitflag (' num2str(exitflag) ').']);
end
%% Objective Function
% Setup of the objective function
function f = ObjMechanism(x)
    t = x(1);
    R = x(2);
    w = x(3);
    L = x(4);

    [~, ~, ~, ~, Ktz, ~, ~, ~] = MechanismAnalytical(t,R,w,L);

    f = -(Ktz*t); % Maximize Hinge Stiffnes with a thickness bias
end

%% Constraints
% setup of the constraints
function [g,geq] = ConstraintCircNotch(x)
    t = x(1);
    R = x(2);
    w = x(3);
    L = x(4);

    [ROM, FB_Kx, ~, ~, ~, ~, ~, ~] = MechanismAnalytical(t,R,w,L);
    geq = [];
    NeededRom = 1; % mm
    g(1) = FB_Kx*NeededRom/13-1;          % Max Actuation Force
    g(2) = -ROM/NeededRom+1;         % Min Range of Motion
    g(3) = -20*t/R+1;       % Ratio Thickness vs Radius lower limit
    g(4) = 1.25*t/R-1;      % Ratio thickness vs radius upper limit
    g(5) = -(L-6*R)+1;          % Link length is longer than three hinge radii
end
%% CNJ analytical equations

%Function used to calculate all equations from supplementary material from
%Farhadi Machekposhti et al., 2015
function [ROM, FB_Kx, Tz, Tzd, Ktz, RatXZ, RatYZ, Ktx] = MechanismAnalytical(t,R,w,L)

    % Material properties
    E = 70e3; %GPa, Young's Modulus
    v = 0.33; % Poisson ratio
    G = E/(2*(1+v)); %GPa, Shear Modulus
    Sy = 300; % MPa, Maximum allowed stress. Although named Sy, it is not actually the Yield
        stress of Alu 7075-T6

    B1 = t/(2*R); % Geometrical parameter
    B2 = 3*pi/(2*B1)^2.5; % Geometrical parameter
    B3 = 2*(1+B1)/sqrt(2*B1+B1^2)*atan(sqrt((2+B1)/B1))-pi/2; % Geometrical Parameter

    % Rotational stiffnesses
    Ktz = (2*E*w*t^2.5)/(9*pi*R^0.5);% Nmm/rad, Rotational stiffness around the Z-axis
    Kty = E*w^3/(12*B3);% Nmm/rad, Rotational stiffness around the Y-axis
    Ktx = G * ( (2*w*t^2.5)/(9*pi*sqrt(R)) + w^3/(12*B3) );% Nmm/rad, Rotational stiffness
        around the X-axis

    % Translational stiffnesses
    Kx = E*w/B3; % [N/mm], Translational stiffness in X
    Ky = 2*E*w/(9*pi)*(t/R)^2.5; % [N/mm], Translational stiffness in Y
    inv_Kz = (R^2/Kty) + (6*R^2/(E*w^3)) * ((2 + 2*B1 + (pi/2)*(1 + 4*B1 + 2*B1^2)) ...
```

```
            - 4*(1 + B1)*sqrt(2*B1 + B1^2)*atan( sqrt((2 + B1)/B1) )); Inverse of the
                translational stiffness in Z
    Kz = 1/inv_Kz; % [N/mm], Translation stiffness in Z

    % Four bar notch translation stiffness
    FB_Kx = 4*Ktz/((L-2*R)^2); % [N/mm], Apparent stiffness of the top rigid connecting link
        of the four bar notch mechanism

    %Range of motions
    Tz = B1^2*B2*Sy/(E*(1+B1)^(9/20));% Hinge angular range of motion [rad]
    Tzd = Tz*180/pi;% Hinge angular range of motion [degree]
    ROM = (L-2*R)*sin(Tz); % Hinge translational range of motion of the rigid link for the
        four bar notch mechanism [mm]

    %Stiffness ratios between hinge rotational DoFs
    RatXZ = Ktx/Ktz; % Rotational stiffness ratio between X and Z
    RatYZ = Kty/Ktz; % Rotational stiffness ratio between Y and Z
end

%% visualization

% Visualization for all pairs of optimization variables
var_names = {'Thickness t [mm]', 'Radius R [mm]', 'Width w [mm]', 'Link Length L [mm]'};
var_indices = 1:4;
fixed_vals = xopt; % Use optimal values for fixed variables

close all
plot_num = 1;
for i = 1:4
    for j = i+1:4
        % Create grid for variable pair (i, j)
        vals_i = linspace(lb(i)-lb(i)*0.05, ub(i)+ub(i)*0.05, 100);
        vals_j = linspace(lb(j)-lb(j)*0.05, ub(j)+ub(i)*0.05, 100);
        [VI, VJ] = meshgrid(vals_i, vals_j);

        % Initialization of relevant vectors for visualization
        F_obj = zeros(size(VI));
        G1 = zeros(size(VI));
        G2 = zeros(size(VI));
        G3 = zeros(size(VI));
        G4 = zeros(size(VI));
        G5 = zeros(size(VI));
        for m = 1:numel(VI)
            x_vis = fixed_vals;
            x_vis(i) = VI(m);
            x_vis(j) = VJ(m);
            f = ObjMechanism(x_vis);
            F_obj(m) = f;
            g = ConstraintCircNotch(x_vis);
            G1(m) = g(1);
            G2(m) = g(2);
            G3(m) = g(3);
            G4(m) = g(4);
            G5(m) = g(5);

        end

        % contour plots for all combinations of design variables
        figure(plot_num);
        contour(VI, VJ, F_obj, 30, 'ShowText','on');
        colorbar;
        hold on;
        contour(VI, VJ, G1, [0 0], 'LineColor', 'k', 'LineWidth', 2);
        contour(VI, VJ, G1, [0.2 0.2], 'LineColor', 'k', 'LineWidth', 1, 'LineStyle', '--');
        contour(VI, VJ, G2, [0 0], 'LineColor', 'r', 'LineWidth', 2);
        contour(VI, VJ, G2, [0.1 0.1], 'LineColor', 'r', 'LineWidth', 1, 'LineStyle', '--');
        contour(VI, VJ, G3, [0 0], 'LineColor', 'm', 'LineWidth', 2);
        contour(VI, VJ, G3, [0.2 0.2], 'LineColor', 'm', 'LineWidth', 1, 'LineStyle', '--');
        contour(VI, VJ, G4, [0 0], 'LineColor', 'm', 'LineWidth', 2);
        contour(VI, VJ, G4, [0.2 0.2], 'LineColor', 'm', 'LineWidth', 1, 'LineStyle', '--');
        contour(VI, VJ, G5, [0 0], 'LineColor', 'g', 'LineWidth', 2);
```

```
        contour(VI, VJ, G5, [10 10], 'LineColor', 'g', 'LineWidth', 1, 'LineStyle', '--');
        plot(xopt(i), xopt(j), 'ro', 'MarkerSize', 8, 'MarkerFaceColor', 'r');
        xlabel(var_names{i});
        ylabel(var_names{j});
        title(['Objective contour: ', var_names{i}, ' vs ', var_names{j}]);
        legend('Objective','Max Force','','Min ROM','','Thickness Guideline','','','', '
            Positive linklength','','Optimal Point','Location','best');
        hold off;
        plot_num = plot_num + 1;
    end
end

% Plot StiffnessHinge for R vs T
t_vals = linspace(lb(1), ub(1), 50);
R_vals = linspace(lb(2), ub(2), 50);
[TT, RR] = meshgrid(t_vals, R_vals);

StiffnessHinge = zeros(size(TT));
w_vis = xopt(3);
L_vis = xopt(4);

for m = 1:numel(TT)
    x_vis = [TT(m), RR(m), w_vis, L_vis];
    [ROM, FB_Kx, Tz, Tzd, Ktz, RatXZ, RatYZ, Ktx] = MechanismAnalytical(x_vis(1), x_vis(2),
        x_vis(3), x_vis(4));
    StiffnessHinge(m) = Ktz;
end

figure;
contour(TT, RR, ((StiffnessHinge)), 30, 'ShowText','on');
colorbar;
hold on;
plot(xopt(1), xopt(2), 'ro', 'MarkerSize', 8, 'MarkerFaceColor', 'r');
xlabel('Thickness t [mm]');
ylabel('Radius R [mm]');
title('Hinge Stiffness (Ktz) for R vs t');
legend('Hinge Stiffness','Optimal Point','Location','best');
hold off;

% Sensitivity plots for each design variable

var_names = {'Thickness t [mm]', 'Radius R [mm]', 'Width w [mm]', 'Link Length L [mm]'};
fixed_vals = xopt; % Use optimal values for fixed variables

figure;
for i = 1:4
    vals = linspace(lb(i), ub(i), 100);
    obj_vals = zeros(size(vals));
    for k = 1:length(vals)
        x_vis = fixed_vals;
        x_vis(i) = vals(k);
        obj_vals(k) = ObjMechanism(x_vis);
    end
    subplot(2,2,i)
    plot(vals, obj_vals, 'b-', 'LineWidth', 2);
    hold on;
    plot(xopt(i), ObjMechanism(xopt), 'ro', 'MarkerSize', 8, 'MarkerFaceColor', 'r');
    xlabel(var_names{i});
    ylabel('Objective Value');
    title(['Sensitivity of Objective to ', var_names{i}]);
    grid on;
    legend('Objective','Optimal Point','Location','best');
    hold off;
end
```

F.2. Fraunhofer curve fitting

The code used to manually fit the measured intensity profiles to a theoretical profile.

```
function interactive_diffraction_fit
```

```
%% 1. Loading of pictures and creation of intensity profile
total_width_mm = 35.9;
lambda = 405e-9;

img_path = "[specify file path].JPG";
img = imread(img_path);

 % File name and folder prep
[~, fname, ~] = fileparts(img_path);
folder_name = 'Intensity Plots';

if ~exist(folder_name, 'dir')
    mkdir(folder_name);
end

export_path = fullfile(pwd, folder_name, strcat(fname, '_intensity_plot.png'));

% Horizontal slice & intensity profile
target_row = 2460; thickness = 40;
row_start = max(1, round(target_row - (thickness/2)));
row_end   = min(size(img, 1), round(target_row + (thickness/2)));
gray_img = img(row_start:row_end, :, 1);

intensity_profile = mean(gray_img, 1);
n_intensity_profile = normalize(intensity_profile, 'range');
[smoothedData,~] = smoothdata(n_intensity_profile, "sgolay", 40);
x_mm = linspace(0, total_width_mm, length(smoothedData));

%% 2. Figure setup
fig = figure('Name', 'Interactive Fraunhofer Fit', 'Position', [100, 100, 1000, 800]);
ax = axes('Parent', fig, 'Position', [0.15, 0.40, 0.75, 0.50], 'FontSize', 16);

hData = semilogy(ax, x_mm, smoothedData, 'LineWidth', 2, 'Color', [0.5 0 0.5], '
    DisplayName', 'Measured');
hold(ax, 'on');
hTheory = semilogy(ax, x_mm, x_mm*0, '--k', 'LineWidth', 2, 'DisplayName', 'Theoretical')
    ;

grid(ax, 'on');
ylim(ax, [3e-3, 4]);
xlabel(ax, 'Position (mm)', 'FontSize', 16);
ylabel(ax, 'Intensity', 'FontSize', 16);
legend(ax, 'Location', 'northeast', 'FontSize', 16);

%% 3. UI Elements
col1 = 50; col2 = 160; col3 = 470; col4 = 550; col5 = 660; col6 = 850;

% Sliders (a, hx, L, t0, xc, Zoom, Scale)
uicontrol('Style','text','String','a (um):','Position',[col1 210 100 20],'
    HorizontalAlignment','left');
s_a = uicontrol('Style','slider','Min',0.5,'Max',100,'Value',20.3,'Position',[col2 210
    250 20]);
e_a = uicontrol('Style','edit','String','20.3','Position',[col3 210 60 20]);

uicontrol('Style','text','String','hx (um):','Position',[col1 170 100 20],'
    HorizontalAlignment','left');
s_hx = uicontrol('Style','slider','Min',-1000,'Max',1000,'Value',-52,'Position',[col2 170
     250 20]);
e_hx = uicontrol('Style','edit','String','-52','Position',[col3 170 60 20]);

uicontrol('Style','text','String','L (mm):','Position',[col4 210 100 20],'
    HorizontalAlignment','left');
s_L = uicontrol('Style','slider','Min',1,'Max',50,'Value',11.5,'Position',[col5 210 180
    20]);
e_L = uicontrol('Style','edit','String','11.5','Position',[col6 210 60 20]);

uicontrol('Style','text','String','theta0 (rad):','Position',[col4 170 100 20],'
    HorizontalAlignment','left');
s_t0 = uicontrol('Style','slider','Min',-0.1,'Max',0.1,'Value',0,'Position',[col5 170 180
     20]);
e_t0 = uicontrol('Style','edit','String','0','Position',[col6 170 60 20]);
```

```
63
64      uicontrol('Style','text','String','Center␣(mm):','Position',[col1 130 100 20],'
            HorizontalAlignment','left');
65      s_xc = uicontrol('Style','slider','Min',10,'Max',25,'Value',14.37,'Position',[col2 130
            500 20]);
66      e_xc = uicontrol('Style','edit','String','14.37','Position',[col6 130 60 20]);
67
68      uicontrol('Style','text','String','Zoom␣(mm):','Position',[col1 90 100 20],'
            HorizontalAlignment','left');
69      s_vw = uicontrol('Style','slider','Min',0.1,'Max',10,'Value',2,'Position',[col2 90 500
            20]);
70      e_vw = uicontrol('Style','edit','String','2','Position',[col6 90 60 20]);
71
72      uicontrol('Style','text','String','Scale:','Position',[col1 50 100 20],'
            HorizontalAlignment','left');
73      s_scale = uicontrol('Style','slider','Min',0.1,'Max',20,'Value',1.3,'Position',[col2 50
            500 20]);
74      e_scale = uicontrol('Style','edit','String','1.3','Position',[col6 50 60 20]);
75
76      uicontrol('Style','pushbutton','String','Save␣PNG','Position',[col4 10 150 40],...
77          'FontSize', 12, 'BackgroundColor', [0.8 0.9 1], 'Callback', @save_plot_png);
78
79      %% 4. Functions
80      function update_from_slider(~, ~)
81          e_a.String = num2str(s_a.Value, '%.2f');
82          e_hx.String = num2str(s_hx.Value, '%.1f');
83          e_L.String = num2str(s_L.Value, '%.2f');
84          e_t0.String = num2str(s_t0.Value, '%.4f');
85          e_xc.String = num2str(s_xc.Value, '%.2f');
86          e_vw.String = num2str(s_vw.Value, '%.2f');
87          e_scale.String = num2str(s_scale.Value, '%.2f');
88          render_plot();
89      end
90
91      function update_from_edit(~, ~)
92          s_a.Value = max(s_a.Min, min(s_a.Max, str2double(e_a.String)));
93          s_hx.Value = max(s_hx.Min, min(s_hx.Max, str2double(e_hx.String)));
94          s_L.Value = max(s_L.Min, min(s_L.Max, str2double(e_L.String)));
95          s_t0.Value = max(s_t0.Min, min(s_t0.Max, str2double(e_t0.String)));
96          s_xc.Value = max(s_xc.Min, min(s_xc.Max, str2double(e_xc.String)));
97          s_vw.Value = max(s_vw.Min, min(s_vw.Max, str2double(e_vw.String)));
98          s_scale.Value = max(s_scale.Min, min(s_scale.Max, str2double(e_scale.String)));
99          render_plot();
100     end
101
102     function render_plot()
103         a_m = s_a.Value * 1e-6;
104         hx_m = s_hx.Value * 1e-6;
105         L_m = s_L.Value * 1e-3;
106         t0 = s_t0.Value;
107         xc = s_xc.Value;
108
109         x_rel_m = (x_mm - xc) * 1e-3;
110         sx = a_m + x_rel_m .* hx_m ./ L_m;
111         sin_theta = x_rel_m ./ L_m;
112         ang = (pi .* sx ./ lambda) .* (sin_theta - sin(t0));
113
114         y_th = (sx.^2) .* (sin(ang)./ang).^2;
115         y_th(ang == 0) = max(sx.^2);
116         y_th = (y_th ./ max(y_th)) * s_scale.Value;
117
118         hTheory.YData = y_th;
119         half_width = s_vw.Value / 2;
120         xlim(ax, [xc - half_width, xc + half_width]);
121
122         title(ax,'Diffraction␣Pattern␣Intensity␣Profile','FontSize', 18)
123         subtitle(ax, sprintf('Fit:␣W␣=%.1fum␣|␣Wafer␣offset=%.0fum␣|␣z=%.2fmm', ...
124             a_m*1e6, hx_m*1e6, L_m*1e3),'FontSize', 16);
125     end
126
127
```

```
    function save_plot_png(~, ~)

        export_fig = figure('Visible', 'off', 'Units', 'pixels', 'Position', [0 0 1100 1100])
            ;
        new_ax = copyobj(ax, export_fig);


        export_lines = findobj(new_ax, 'Type', 'line');
        set(export_lines, 'LineWidth', 3); % Dikte naar 3 voor betere zichtbaarheid
        set(new_ax, 'LineWidth', 1.75, 'GridAlpha', 0.4);
        set(new_ax, 'Units', 'normalized', 'Position', [0.12 0.12 0.80 0.75], 'FontSize', 20)
            ;

        lines = findobj(new_ax, 'Type', 'line');

        legend(new_ax, [lines(2), lines(1)], {'Measured␣intensity', 'Theoretical␣intensity'},
             ...
            'Location', 'northeast', 'FontSize', 18);

        title(new_ax, 'Diffraction␣Pattern␣Intensity␣Profile', 'FontSize', 24);

        print(export_fig, export_path, '-dpng', '-r0');
        close(export_fig);

        msgbox(['Plot␣saved␣to␣', folder_name], 'Success');
    end
    %% 5. Callbacks
    addlistener(s_a, 'Value', 'PostSet', @update_from_slider);
    addlistener(s_hx, 'Value', 'PostSet', @update_from_slider);
    addlistener(s_L, 'Value', 'PostSet', @update_from_slider);
    addlistener(s_t0, 'Value', 'PostSet', @update_from_slider);
    addlistener(s_xc, 'Value', 'PostSet', @update_from_slider);
    addlistener(s_vw, 'Value', 'PostSet', @update_from_slider);
    addlistener(s_scale, 'Value', 'PostSet', @update_from_slider);

    set(e_a, 'Callback', @update_from_edit);
    set(e_hx, 'Callback', @update_from_edit);
    set(e_L, 'Callback', @update_from_edit);
    set(e_t0, 'Callback', @update_from_edit);
    set(e_xc, 'Callback', @update_from_edit);
    set(e_vw, 'Callback', @update_from_edit);
    set(e_scale, 'Callback', @update_from_edit);

    render_plot();
end
```

F.3. Linear regression fit

The code used to perform the linear regression fit for the parallelism test and the actuation characterization.

```
clf; clf; close all;

%% Plot data
x = [14.19231, 13.96154, 13.73077, 13.5, 13.26923, 13.03846, ...
     12.80769, 12.57692, 12.34615, 12.11538, 11.88462, 11.65385, ...
     11.42308, 11.19231, 10.96154, 10.73077, 10.5, 10.26923, 10.03846];

y = [19.3, 19.8, 21, 21, 20.7, 21.5, 21, 20.2, 20.8, 21.3, ...
     21.2, 21, 21, 21.4, 21, 20.5, 20.8, 23.5, 23.5];

x2 = [13.73077, 13.5, 13.26923, 13.03846, ...
     12.80769, 12.57692, 12.34615, 12.11538, 11.88462, 11.65385, ...
     11.42308, 11.19231, 10.96154, 10.73077, 10.5];

y2 = [21, 21, 20.7, 21.5, 21, 20.2, 20.8, 21.3, ...
     21.2, 21, 21, 21.4, 21, 20.5, 20.8];

x3 = [1:11];
y3 = [16.7 16.5 16.3 16.1 15.8 15.5 15.3 15.2 14.9 14.8 14.5];
```

```
20
21
22 x4 = [1:13];
23 y4 = [26        24.5    23.4    22.5    21      19.5    18.1    16.7    15.4    14      12.5
       11.2       9.6];
24
25 %% Linear regression calculation
26 p = polyfit(x, y, 1);
27 y_fit = polyval(p, x);
28
29 p2 = polyfit(x2, y2, 1);
30 y_fit2 = polyval(p2, x2);
31
32 p3 = polyfit(x3,y3,1);
33 y_fit3 = polyval(p3, x3)
34
35 p4 = polyfit(x4,y4,1);
36 y_fit4 = polyval(p4, x4)
37
38 y_resid = y - y_fit;
39 SS_resid = sum(y_resid.^2);
40 SS_total = sum((y - mean(y)).^2);
41 r2 = 1 - (SS_resid / SS_total);
42
43 y_resid2 = y2 - y_fit2;
44 SS_resid2 = sum(y_resid2.^2);
45 SS_total2 = sum((y2 - mean(y2)).^2);
46 r22 = 1 - (SS_resid2 / SS_total2);
47
48 y_resid3 = y3 - y_fit3;
49 SS_resid3 = sum(y_resid3.^2);
50 SS_total3 = sum((y3 - mean(y3)).^2);
51 r23 = 1 - (SS_resid3 / SS_total3);
52
53 y_resid4 = y4 - y_fit4;
54 SS_resid4 = sum(y_resid4.^2);
55 SS_total4 = sum((y4 - mean(y4)).^2);
56 r24 = 1 - (SS_resid4 / SS_total4);
57
58
59 slope_str = sprintf('Fit␣1:␣y␣=␣%.3fx␣+␣%.3f', p(1), p(2));
60 r2_str = sprintf('R^2_1␣=␣%.4f', r2);
61 slope_str2 = sprintf('Fit␣2:␣y␣=␣%.3fx␣+␣%.3f', p2(1), p2(2));
62 r22_str = sprintf('R^2_2␣=␣%.4f', r22);
63 slope_str3 = sprintf('Fit:␣y␣=␣%.3fx␣+␣%.3f', p3(1), p3(2));
64 r23_str = sprintf('R^2␣=␣%.4f', r23);
65 slope_str4 = sprintf('Fit:␣y␣=␣%.3fx␣+␣%.3f', p4(1), p4(2));
66 r24_str = sprintf('R^2␣=␣%.4f', r24);
67
68 fprintf('Regression␣Equation:␣y␣=␣%.4fx␣+␣%.4f\n', p(1), p(2));
69 fprintf('Regression␣Equation:␣y2␣=␣%.4fx␣+␣%.4f\n', p2(1), p2(2));
70 fprintf('Regression␣Equation:␣y3␣=␣%.4fx␣+␣%.4f\n', p3(1), p3(2));
71 fprintf('Regression␣Equation:␣y4␣=␣%.4fx␣+␣%.4f\n', p4(1), p4(2));
72 fprintf('R2␣=␣%.3f',r2);
73 fprintf('R2␣=␣%.3f',r22);
74 fprintf('R2␣=␣%.3f',r23);
75 fprintf('R2␣=␣%.3f',r24);
76
77 %% 3. Plots
78 figure(1);
79 hold on; grid on;
80 scatter(x([3:17]), y([3:17]), 'filled', 'DisplayName', 'Data␣Points','MarkerFaceColor','r');
       % Scatter plot
81 scatter(x([1 2 18 19]), y([1 2 18 19]), 'filled', 'DisplayName', 'Data␣outliers','
       MarkerFaceColor','m'); % Scatter plot
82
83 plot(x, y_fit, 'b--', 'LineWidth', 2, 'DisplayName', 'Linear␣Fit'); % Regression line
84 plot(x2, y_fit2, 'g--', 'LineWidth', 2, 'DisplayName', 'Linear␣Fit␣exluding␣extremities'); %
       Regression line
85
86 grid on;
```

```
xlabel('Vertical position in image [mm]');
ylabel('Slit width [\mu m]');
title('Angular alignment linear regression');
legend('Location', 'northeast');
text(0.05, 0.15, [slope_str newline r2_str newline slope_str2 newline r22_str], 'Units', '
    normalized', 'FontSize', 10, 'BackgroundColor', 'white');
% text(0.05, 0.1, [], 'Units', 'normalized', 'FontSize', 10, 'BackgroundColor', 'white');
hold off;


figure(2);
scatter(x4,y4, 'filled', 'DisplayName', 'Data Points','MarkerFaceColor','r');
hold on;
plot(x4, y_fit4, 'b--', 'LineWidth', 2, 'DisplayName', 'Linear Fit');
grid on;
xlabel('Step number');
ylabel('Slit width [\mu m]');
title('50 step increment actuatation characterization');
legend('Data Points', 'Linear fit', 'Location', 'northeast');
text(0.05, 0.1, [slope_str4 char(10) r24_str], 'Units', 'normalized', 'FontSize', 10, '
    BackgroundColor', 'white');

figure(3);
scatter(x3,y3, 'filled', 'DisplayName', 'Data Points','MarkerFaceColor','r');
hold on;
plot(x3, y_fit3, 'b--', 'LineWidth', 2, 'DisplayName', 'Linear Fit');
grid on;
xlabel('Step number');
ylabel('Slit width [\mu m]');
title('10 step increment actuatation characterization');
legend('Data Points', 'Linear fit', 'Location', 'northeast');
text(0.05, 0.1, [slope_str3 char(10) r23_str], 'Units', 'normalized', 'FontSize', 10, '
    BackgroundColor', 'white');
```

COMSOL Multiphysics®supporting material

In this Appendix, supporting material for the simulations and TO performed using COMSOL multiphysics can be found.

G.1. Validation simulations

Mesh fidelity used for the validation simulations can be seen in Figures G.1 to G.3. Meshes used for the validation of the topology optimized domain can be found in Figures G.4 to G.6.

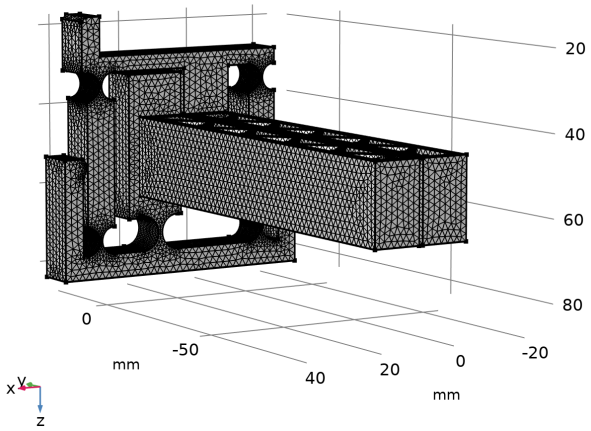

Figure G.1: Overview of the mesh used for the validation studies for the traditional mechanism.

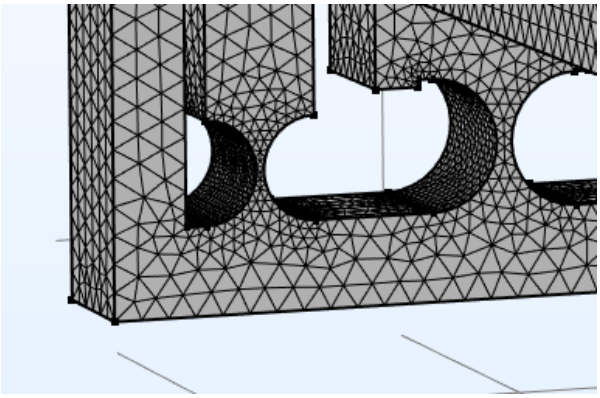

Figure G.2: Close up of the mesh used for the 3D validation studies for the traditionally designed mechanism.

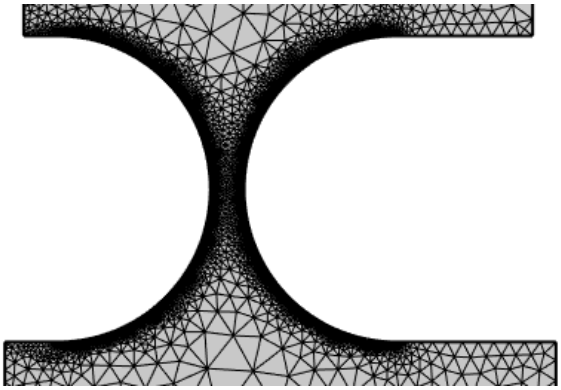

Figure G.3: Close up for the mesh fidelity used for the 2D validation studies.

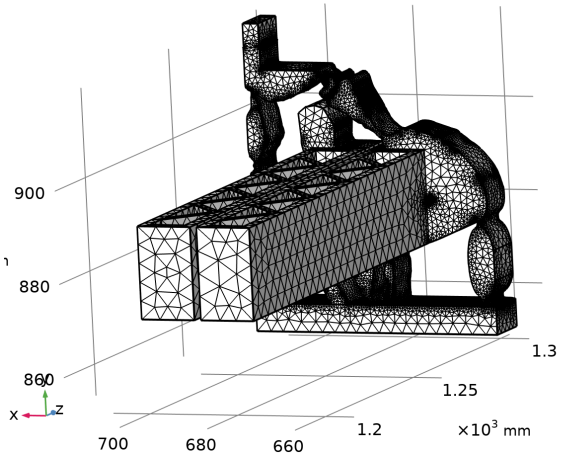

Figure G.4: Overview of the mesh used for the validation studies for the topology optimized mechanism

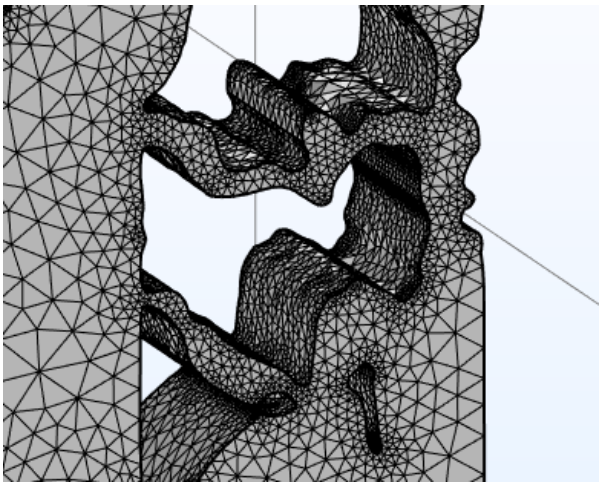

Figure G.5: Close up of the mesh used for the 3D validation studies for the TO mechanism.

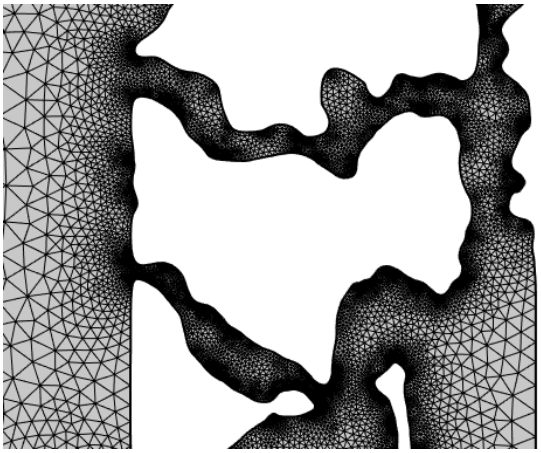

Figure G.6: Close up for the mesh fidelity used for the 2D validation studies of the TO mechanism.

G.2. Topology optimization

Image of the mesh fidelity for the optimized domain can be seen in Figure G.7.

An overview of the optimization history taken for each 75 iterations can be seen in Figure G.8.

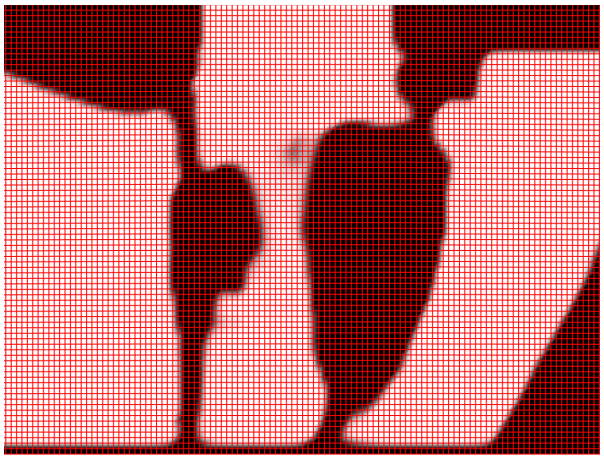

Figure G.7: Image showcasing the mesh fidelity used in the topology optimization.

Figure G.8: Optimization results taken each 75 iterations.

H

Alternative designs

H.1. Alternative slit mechanism design

An alternative slit mechanism was shortly considered. The main reason for the consideration is that for the chosen design, the center of the slit moves when the translating side is actuated. For the chosen design this is solved using a translation stage on which the mechanism is mounted. This alternative design, which is shown in Figure **??**, proposed by Zubir et al., 2009, solves this issue intrinsically by moving both halves of the slit simultaneously and symmetrically. The drawback for this design is that there is no rotating DoF present. Furthermore, the mechanism as presented by Zubir et al., 2009 is too large to fit in the design space available.

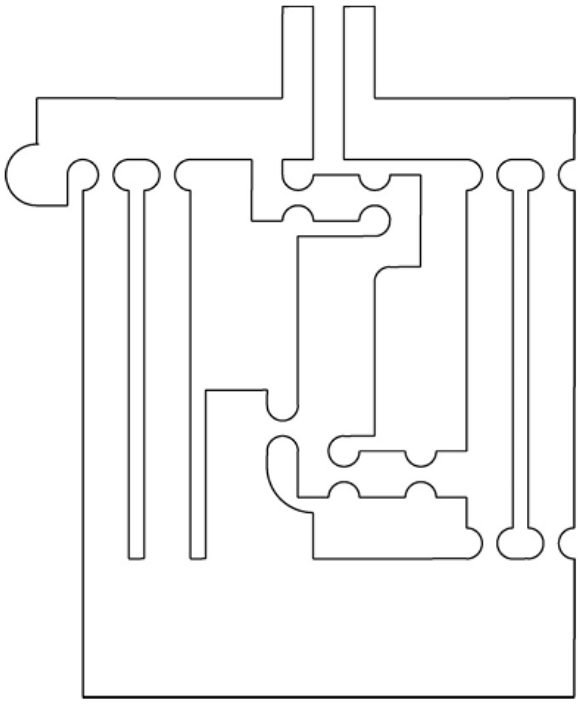

Figure H.1: Basic geometrical model of the micro gripper by Zubir et al., 2009.

An attempt to adapt this mechanism can be seen in Figure **??**. There were some issues with this adaption. Firstly, the exact dimensions and required ratios between the compliant linkages was not available in the paper. The full analytical derivation was also not given. So replicating the symmetrical motion was quite difficult to achieve. Secondly, an extra linkage had to be added to adapt the

mechanism to the design space. Adding this linkage also changes the kinematics of the mechanism, further increasing the difficulty of adapting the mechanism. Simulations also showed that the crucial out of plane stiffnesses were also not better for this mechanism than for the chosen design. So, it was chosen to discard this option.

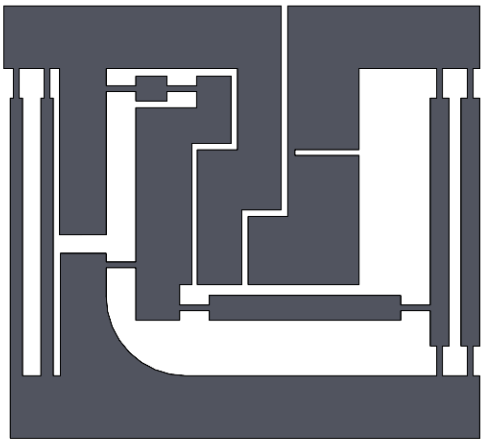

Figure H.2: The mechanism presented by Zubir et al., 2009.

H.2. Actuation transmission

A system layout including a transmission to actuate the translating DoF was briefly considered, mainly due to perceived spatial constraints. This layout can be found in Figure H.3. However, as the actuators already provide sufficient resolution, there is no need for the transmission.

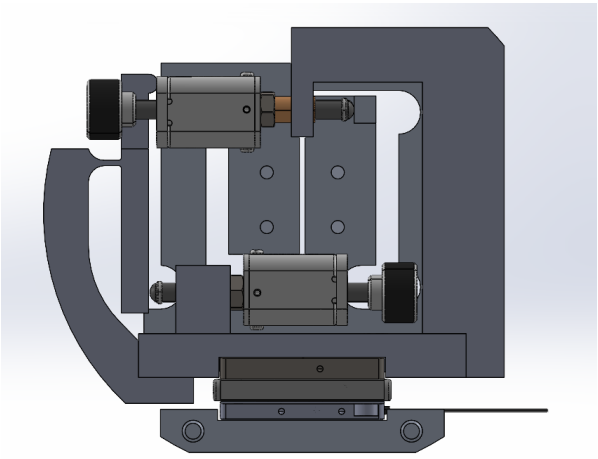

Figure H.3: Alternate layout using a transmission to actuate the translating DoF.

Topology Optimization alternative methods

In this Appendix adaption of Koppen's method (Koppen et al., 2022) for flexure synthesis using topology optimization to the optimization formulation presented in Chapter 5 will be presented. This method is intended to be used for flexures, not necessarily for mechanisms. Because of this, implementation of an actuation point is missing from the design problem. This is the main problem that needs to be addressed in order to properly adapt the method to the mechanism design case in this report.

Firstly, the method applied by Koppen et al., 2022 will be discussed briefly. Secondly, an adaption to this design problem without actuation will be presented, along with some realizations. Then, the stiffness matching will be discussed. Finally, the proposed method for the implementation of an actuation point is presented.

I.1. Koppen's method

As briefly discussed in Section 5.2.1, a novel way to optimize short-stroke flexures was presented by Koppen et al., 2022. To design flexures using topology optimization, Strain Energy SE is used. The six possible *Motion Patterns* (MP), the three axes of translation and rotation, are divided into two sets. Set $\mathbb{F}$ containing the free MPs or degrees of freedom, and $\mathbb{C}$, containing the constrained MPs or degrees of constraint. The goal is to maximize the stiffness of the constrained MPs whilst constraining the stiffness in the free MPs. The strain energy is used to measure the stiffness of each MP. By minimizing the strain energy under a prescribed displacement, the corresponding stiffness is minimized. The problem formulation can be stated using the following three equations:

$$\mathcal{P} = \begin{cases} \text{minimize} & -f\left[\mathcal{E}_i[\mathbf{x}]\right], \quad i \in \mathcal{C} \\ \text{subject to} & \mathcal{E}_j[\mathbf{x}] \leq \bar{\mathcal{E}}_j, \quad j \in \mathcal{F}, \\ & \mathbf{x} \in \mathcal{X}^N \end{cases} \tag{I.1}$$

The objective function contains the maximization of stiffness of the constraint MPs. Minimizing the negative value of the strain energy $\mathcal{E}_i$ maximizes the absolute value, corresponding to high stiffness. The strain energies $\mathcal{E}_j$ are limited to remain below the chosen maximum value $\mathcal{E}_j$. This strain energy can be selected according to the design requirements, based on strain energy directly, or by equating it to a desired stiffness (Koppen et al., 2022), using Equation 5.2.1.

I.1.1. Adaption to the design case

This method, without the implementation of actuators, can be used for the design case of the slit quite easily. In contrast to the design domain laid out in Section 5.1, no input forces are used. Rather, prescribed displacements are placed at output 1 and 2. For each output, three separate FEA are implemented. One for each dummy prescribed displacement. For each of the two outputs, the strain energy is maximized for the constrained motion paths. This means that the objective function is the sum of 4 SEs. The SE for the free motion paths is constrained according to Equations **??** and **??**.

In contrast to the optimization scheme described in Chapter 5, as the motions are prescribed there can

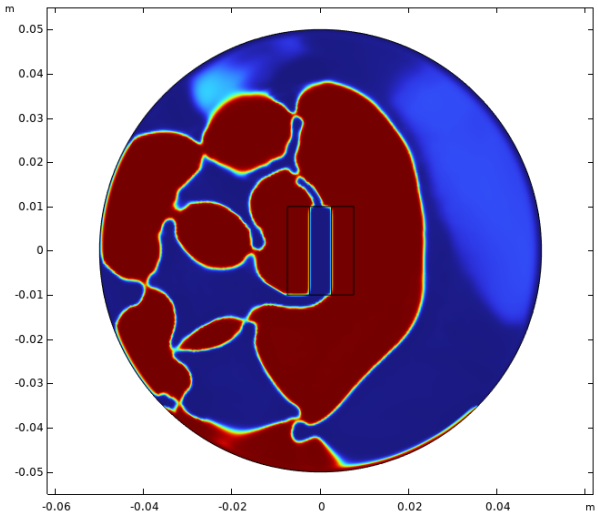

Figure I.1: Topology optimized design for a circular domain, without input implementation.

be no parasitic displacements. So, they are not considered for the constraints. For these exploratory topologies, the coupling between outputs was also not necessarily considered. Additionally, design domains with the dimensions of the vacuum six way cross were also tried. The optimization problem is the following:

$$
\begin{aligned}
&min : f(\boldsymbol{\rho}) \\
&with : f = SE_1(\boldsymbol{\rho}) + SE_2(\boldsymbol{\rho}) + SE_3\boldsymbol{\rho}) + SE_4(\boldsymbol{\rho}) \\
&\quad s.t. : \frac{2SE_5}{u^2_{O1,u}} \leq k_{O1,u} \\
&\qquad\quad : \frac{2SE_6}{u^2_{O2,\theta}} \leq k_{O2,\theta}
\end{aligned}
$$

An example showing the capabilities of this optimization formulation can be seen in Figure I.1. It is notable that this is not yet a practical design for the design case. However, the optimization does show a clean black and white design, which shows promise for further exploration. The lack of clear actuation points is noticeable too.